5-2006

Nondestructive Evaluation of Loading and Fatigue Effects in Haynes® 230® Alloy

Tarik Adel Saleh
University of Tennessee - Knoxville

To the Graduate Council:

I am submitting herewith a dissertation written by Tarik Adel Saleh entitled "Nondestructive Evaluation of Loading and Fatigue Effects in Haynes® 230® Alloy." I have examined the final electronic copy of this dissertation for form and content and recommend that it be accepted in partial fulfillment of the requirements for the degree of Doctor of Philosophy, with a major in Materials Science and Engineering.

Peter Liaw, Major Professor

We have read this dissertation and recommend its acceptance:

Hahn Choo, George Pharr, John Landes

Accepted for the Council:
Dixie L. Thompson

Vice Provost and Dean of the Graduate School

(Original signatures are on file with official student records.)

To the Graduate Council:

I am submitting herewith a dissertation written by Tarik Adel Saleh entitled "Nondestructive Evaluation of Loading and Fatigue Effects in Haynes® 230® Alloy." I have examined the final electronic copy of this dissertation for form and content and recommend that it be accepted in partial fulfillment of the requirements for the degree of Doctor of Philosophy, with a major in Materials Science and Engineering.

Peter Liaw

_____

Major Professor

We have read this dissertation and recommend its acceptance:

Hahn Choo

George Pharr

John Landes

Acceptance for the Council:

Anne Mahew

Vice Chancellor and Dean of Graduate Studies

(Original Signatures are on file with official student records.)

NONDESTRUCTIVE EVALUATION OF LOADING AND FATIGUE EFFECTS IN HAYNES® 230® ALLOY

A Dissertation
Presented for the
Doctor of Philosophy Degree
The University of Tennessee, Knoxville

Tarik Adel Saleh
May 2006

Dedication

This thesis is dedicated to the memory of my grandfather Richard Denton. His intellectual curiosity and example as a person and as an engineer has encouraged and inspired me greatly in my endeavors. Thank you, Granddad.

Acknowledgements

Firstly, I wish to thank my parents and brother for their constant encouragement throughout the years of schooling I have undertaken. Without their unwavering support I never would have reached this level.

Projects as large as this are never completed independently. I relied on many colleagues for advice, technical and scientific help, relevant and irrelevant conversations, and, of course, much needed distractions. Most important among the many that helped in these regards were Dr. Hahn Choo, Dr. Raymond Buchanan, Mr. Doug Feilden, Dr. Bjorn Clausen, Mr. Thomas Sisneros, Dr. Shannon McDaniel, Dr. Bing Yang, Mr. Michael Benson, Mr. Robert McDaniels and Ms. Rejanah Steward. Certainly, I would like to thank my advisor Dr. Peter Liaw for his rich and famous encouragement and his tireless editing. The work herein was supported by the NSF IGERT and IMI grants, as well as by materials and support by Haynes International and Dr. Dwaine Klarstrom.

Finally, I would like to thank the hours between midnight and 5 am, without which virtually none of the writing would have occurred.

Abstract

Nondestructive evaluation is a useful method for studying the effects of deformation and fatigue. In this dissertation I employed neutron and X-ray diffraction, nonlinear resonant ultrasound spectroscopy (NRUS), and infrared thermography to study the effects of deformation and fatigue on two different nickel based superalloys. The alloys studied were HAYNES 230, a solid solution strengthened alloy with 4% M_6C carbides, and secondarily HASTELLOY C-2000 a similar single phase alloy.

Using neutron and X-ray diffraction, the deformation behavior of HAYNES 230 was revealed to be composite-like during compression, but unusual in tension. The carbides present in this alloy do not provide strengthening in tension as would be expected or finite element modeling predicted. The carbides provide strengthening until just after the macroscopic yield strength and then they begin to debond and crack, creating a tension-compression asymmetry that is revealed clearly by *in situ* diffraction. HASTELLOY C-2000, a similar alloy without carbides, shows typical anisotropic load sharing between differently oriented grains.

In fatigue of HAYNES 230, the *hkl* behavior as revealed by neutron diffraction showed that the elastic strain changes very little in tension-tension fatigue. However, *in situ* tension-compression studies showed large changes over the initial stages of fatigue. There was slight evidence for changes in elastic modulus as fatigue progressed.

The HAYNES 230 samples studies had two distinct starting textures, measured by neutron diffraction. Some samples were texture free initially and deformed in tension and compression to fiber textures. Other samples started with a bimodal texture due to cross-rolling and incomplete annealing. The final texture of these bimodal samples is shown through modeling to be a superposition of the initial texture and typical FCC deformation mechanisms. The effect of these different textures on the macroscopic and internal-elastic stress-strain curves are shown. The texture-free samples deformed significantly more macroscopically and in internal elastic strains than the samples with the cross-rolled texture.

In contrast to the relative insensitivity of neutron diffraction to the effects of tension-tension fatigue, NRUS revealed large differences between as-received and progressively fatigued samples. This showed that microcracking and void formation are the primary mechanisms responsible for fatigue damage in tension-tension fatigue. NRUS is shown to be a useful complimentary technique to neutron diffraction to evaluate fatigue damage.

Finally, infrared thermography is used to show temperature changes over the course of fatigue in HASTELLOY C-2000. Four stages of temperature are shown over the course of a single fatigue test: an initial temperature rise, followed by an equilibrium region, a sharp increase of temperature at failure and, finally, a cooling back to room temperature after fracture. Both empirical and theoretical relationships between steady state temperature and fatigue life are developed and presented.

Table of Contents

List of Tables

List of Figures

Chapter 1

Introduction

The utility of nondestructive methods for evaluating something is undeniable. The simple example of a broken arm is proffered. There are two ways of determining if there is a broken bone in an injured arm:

1. Cut the arm open and see if the bone is broken
2. Use an X-ray to view if the bone is broken or intact

While the first method is very straightforward, it hearkens to opening the goose to see how the golden egg is made, no one wins, especially not the goose. The second method, while requiring a degree of expertise and interpretation, is much preferable, both from the standpoint of the owner of the injured limb and for the prospects of fixing the problem.

Nondestructive evaluation (NDE) is extremely useful for applications ranging from medicine, to manufacturing, to quality control, to facilities operations, to research and development. The underlying principle is to obtain an accurate evaluation of the condition and state of an object without destroying it, or altering it in a process. As shown above, the medical case is obvious, finding out if you are healthy should avoid injuring or killing you, if possible. Similarly, clever use of NDE techniques can allow the monitoring of the quality of parts on an assembly line without damaging their salability. For large facilities, such as nuclear reactors, being able to evaluate the soundness of a critical pressure vessel *in situ* during operations allows you to both accurately asses damage during

operational conditions and avoid costly downtime during destructive testing or component failure. Finally, during research and development, as evidenced by the following document, NDE can add a new dimension to traditional mechanical testing.

This dissertation uses three methods of NDE: neutron diffraction, nonlinear acoustics, and infrared thermography. The focus will be on *in situ* diffraction. The data presented here shows the elastic strain and texture development during loading operations. A simple diffraction pattern, analyzed and interpreted, can reveal grain-orientation dependent strains in a material, as well as the interplay between multiple phases. Additionally, the material's texture can be examined and its subsequent effect on loading operations can be studied.

While much less daunting from an equipment perspective, the infrared (IR) thermography method provides a similar utility as an NDE technique. Directly measuring heat on the surface of an object undergoing loading can reveal the elastic and plastic behavior in a material. Moreover, estimates of fatigue lifetime can be made from the steady-state temperature achieved during a fatigue test.

Finally nonlinear-acoustic methods are used to analyze damage during fatigue, *ex situ*. While the diffraction techniques shown are very sensitive to the elastic behavior due to changes in the atomic spacing in the material, they are not directly sensitive to plastic strains and stresses. These acoustic methods, however, are sensitive to dislocation density, cracking, and void formation. Data from these

tests will compliment the elastic measurements of fatigue damage and allow a much fuller picture of the internal state of a material.

While the NDE methods described herein are not specific to any group or class of materials, they will be applied exclusively to two different nickel-based superalloys. The alloys studied, primarily HAYNES 230 and secondarily Hastelloy C-2000, are solid-solution strengthened superalloys, derivatives of a long line of Ni-Cr and Ni-Cr-Mo type alloys. They are used in a variety of fatigue-intensive and high-temperature environments, often in harsh atmospheres.

The current study was initially motivated by some anomalies in the high-temperature behavior of the HAYNES 230 alloy. As is often the case in research, the direction of the project has morphed considerably since its beginnings four years ago. The highlight of the following research is the investigation of the load sharing between the matrix and carbides in HAYNES 230 alloy during tension and compression using neutron and X-ray diffraction, as well as finite element modeling (FEM) techniques. Additional studies presented are the development of internal strains during loading and fatigue as well as texture development using neutron diffraction, development of fatigue lifetime prediction using infrared thermography, and the use of acoustic techniques to assess damage as fatigue progresses.

The techniques and results presented in this dissertation offer a comprehensive use of NDE techniques to study the effects of loading and fatigue on the internal state of HAYNES 230.

Chapter 2

Materials

2.1 HAYNES 230

The HAYNES 230 alloy studied in this project is a nickel-based superalloy frequently used in fatigue-intensive applications, such as power-generation turbines. It is a nickel-chromium-tungsten-molybdenum alloy that is optimized for use in high-temperature, oxidizing, and nitriding environments. It was designed to improve the oxidation resistance, creep-rupture strength and thermal stability of existing Haynes superalloys, such as HASTELLOY X and HAYNES 188 [1], while minimizing the use of cobalt, due to a large price increase of this element in the 1970's [2]. It exhibits temperature-induced carbide formation at high temperatures, resulting in a plateau in the yield strength between 600 and 800 ºC [1, 3, 4]. Additionally, there is an anomaly in the low-cycle fatigue behavior of the alloy at high temperatures. At strain ranges between 1.5 and 2%, the fatigue life is actually longer at 927 ºC than at 816 ºC [5]. Exploring the cause of these behaviors has motivated the current study in the fatigue behavior of HAYNES 230 alloy.

HAYNES 230 alloy is a nickel-based solid-solution strengthened super-alloy with a composition of as shown in Table 2.1.

Table 2.1. Nominal Composition of HAYNES 230 Alloy (Wt. %)

Ni	Cr	W	Mo	Fe	Co	Mn	Si	Al	C	La	B
Bal.	22	14	2	3*	5*	0.5	0.4	0.3	0.1	0.02	0.015*

*maximum

The alloy contains approximately 60% nickel as a balance. The Cr addition increases oxidation resistance by allowing a coherent chromium oxide layer to form on the surface of the alloy. The minor additions of Si, Mn and La also help with the oxidation resistance. The W and Mo additions provide solid-solution strengthening from substitutional strain on the lattice. Additionally, with the C addition, the Cr, W and Mo form strong carbides. The ratio of the primary alloying elements (Cr, W and Mo) is controlled to ensure that $M_{23}C_6$ carbides precipitate out at high temperatures. The B is added to change the lattice parameter of the carbide, so it is more coherent with the matrix [1]. As shown later, the lattice parameter of the M_6C carbide is approximately three times that of the alloy. The structure of the metal is face-centered cubic (FCC) with carbide strengthening. As seen in Figure 2.1a the as-received state contains a primary tungsten-rich M_6C carbide that is semicoherent with the parent metal. There are a small amount of chromium-rich $M_{23}C_6$ carbides on the grain boundaries in the as-received condition, Figure 2.1b [6].

The alloy is rolled from an electro-slag remelted slab ingot on a 4-hi

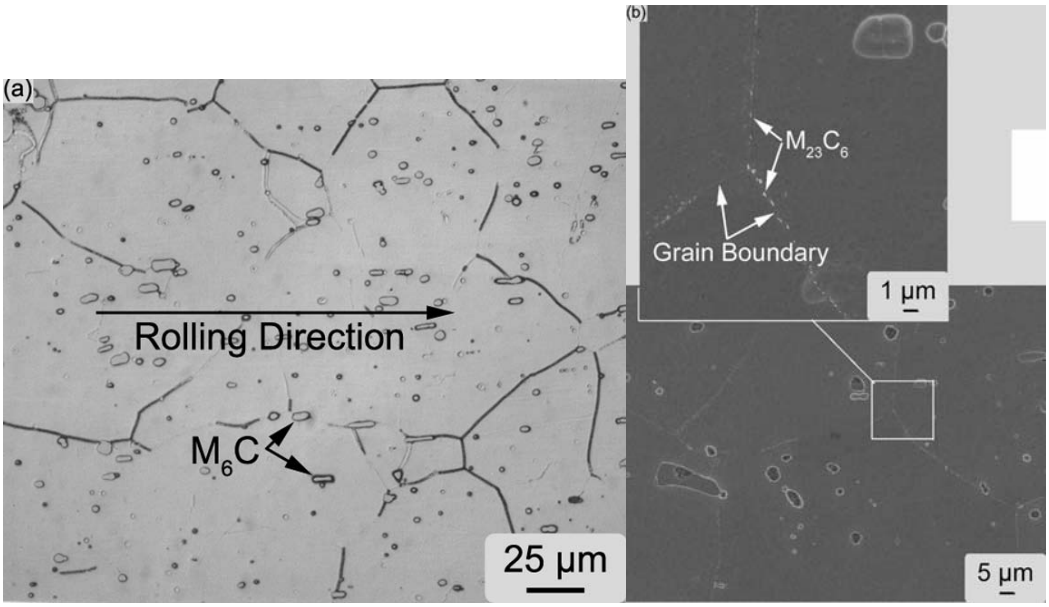

Figure 2.1: Micrograph showing the as-received microstructure of HAYNES 230 alloy, highlighting the M_6C carbides (Figure 2.1a) and the $M_{23}C_6$ carbides (Figure 2.1b) [6].

reversing mill at approximately 1200 °C. After rolling to the final gauge, the plate is solution annealed at 1200 °C and water quenched. The end result of the solution annealing is nominally a texture-free condition, however, as seen in Chapter 7, there are weak rolling and cross rolling textures in the as-received condition depending on the size of the initial plate. The grain size of the material averages 70 μm. The M_6C carbide makes up 1-5% by volume of the as-received microstructure.

The tensile properties of the alloy are: 0.2% yield strength of 375 MPa, ultimate tensile strength of 844 MPa, and elongation at failure of 48% [4]. Based on actual stress-strain experiments performed on the as-received material, tested per American Society for Testing and Materials (ASTM) standards [7, 8] at a strain rate of 5×10^{-3}/min, the 0.2% offset yield strength of the materials are 385 MPa in compression and 425 MPa in tension, Figure 2.2. However, as will be shown, the texture of the as-received specimens has an effect on the yield strength of the material. Significantly, with regard to the internal elastic strains, the deviation from linearity of the stress versus strain curve occurs below 300 MPa in both tension and compression (Chapter 5). The tested elastic modulus of 212 GPa is very close to the literature values.

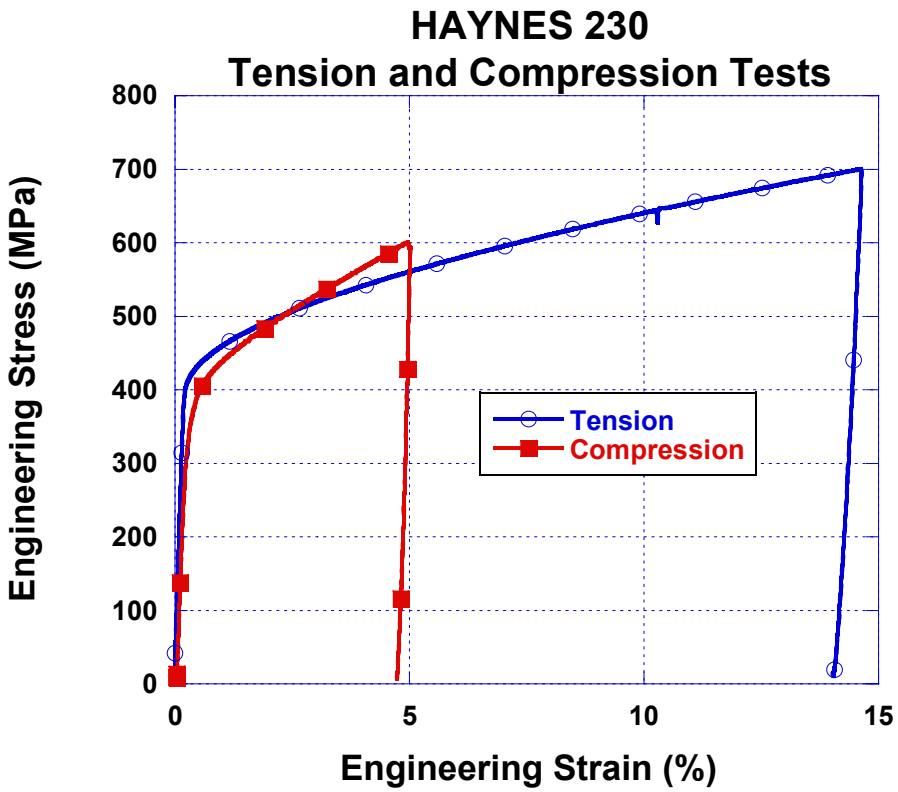

Figure 2.2: Engineering stress-strain curves for tension and compression experiments on HAYNES 230 alloy.

2.2 HASTELLOY C-2000

The second alloy studied is HASTELLOY C-2000. The alloy is a nickel-based superalloy with a composition shown in Table 2.2. The alloy contains approximately 59% nickel as a balance. It is a solid-solution strengthened FCC Ni-Cr-Mo type alloy that is formulated to resist both oxidizing and reducing atmospheres. The Cr and Mo act as substitutional-strengthening mechanisms, the Cr is a strong oxide former, while the Cu enhances the corrosion resistance in both oxidizing and reducing atmospheres [9, 10].

The test specimens were machined from bars, which had been hot rolled in the temperature range of 1176-1204 ºC, annealed at 1149 ºC, and then water quenched. The tensile properties of the alloy: 0.2% yield strength of 370 MPa, ultimate tensile strength of 750 MPa, and elongation at failure of 63% [10]. However, in actual testing conditions, per ASTM standards [7] at a strain rate of 5 x 10^{-3}/min, the alloy exhibited a much higher elongation, approximately 85%, at the UTS, Figure 2.3. The as-received microstructure, shown in Figure 2.4, is a single phase FCC structure with annealing twins and an average grain size of 180 - 200 μm [11].

Table 2.2 Nominal Composition of HASTELLOY C-2000 Alloy (Wt. %)

Ni	Cr	Mo	Cu	Si	C
Bal.	23	16	1.6	0.08*	0.01*

*maximum

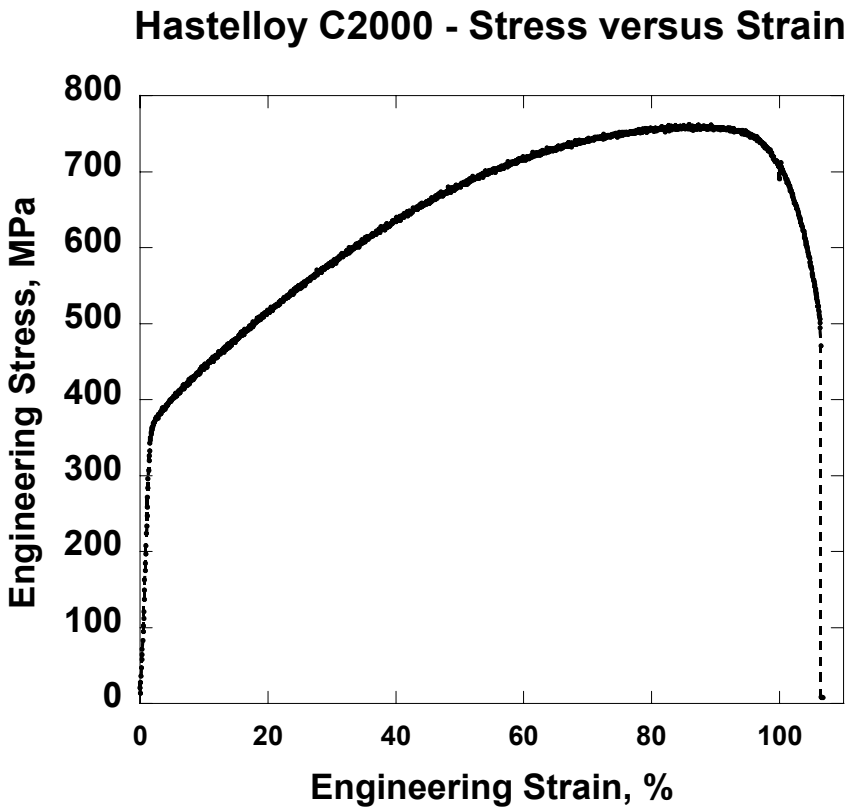

Figure 2.3: Engineering stress-strain curves for a tension experiment on HASTELLOY C-2000 alloy.

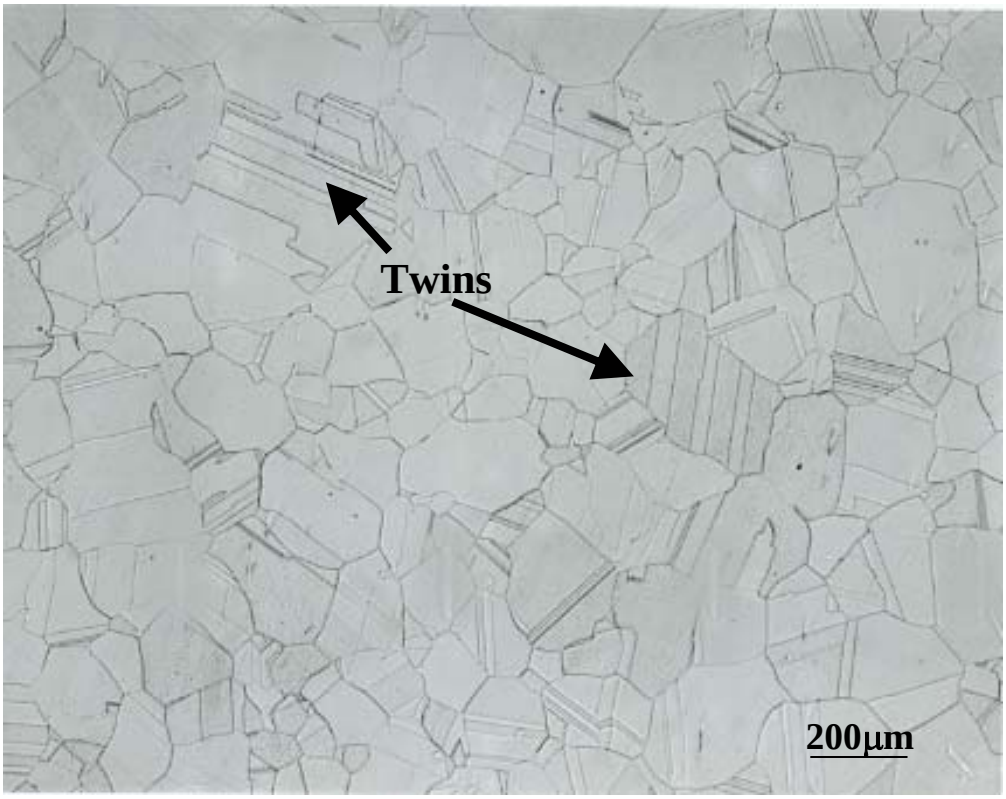

Figure 2.4: As-received HASTELLOY C-2000 microstructure showing a large 180 - 200 μm grain size and extensive annealing twins [11].

Chapter 3

Diffraction

3.1 Background

As with X-ray and electron diffraction, the behavior of neutron diffraction is dictated by Bragg's law:

$$n\lambda = 2d\sin\theta \tag{3.1}$$

A neutron beam incident upon an appropriate specimen will yield a peak pattern much like an X-ray pattern. However, X-rays tend to have very small penetration depths into materials, making it difficult to determine anything beyond surface information. Similarly, electrons, due to their charge, scatter strongly off the electron clouds surrounding atoms. In order to use electron diffraction to study a material, the sample must be very thin. Neutrons have a few key properties that make them attractive for studying material properties [12-15].

Neutrons are neutral particles. They have no interaction, electrostatic or otherwise, with the electron cloud surrounding an atom. Thus, the neutrons scatter directly off the nucleus of materials. The nucleus of an atom is orders of magnitude smaller than the atomic radius. Neutrons are faced with a much smaller cross section to scatter off than electrons or photons. Additionally, the nuclear radii do not change with the atomic number (Z) nearly as much as the atomic radii. Because of this, the atomic-scattering factor from neutrons does not scale with Z

number as with X-rays. In fact, negative and positive scattering can occur. This feature allows differentiation between atoms of similar Z numbers and even isotopes of the same atom. Neutrons can detect hydrogen in a structure and can differentiate between hydrogen and deuterium.

Neutrons are similar in wavelength to typical X-ray radiation, but have much lower energies. The interaction between a low-energy neutron and a nucleus of an atom is fairly weak. This weak interaction, coupled with the small cross section of the nuclei, allows neutrons to penetrate much more deeply than X-rays. Similarly, the neutrons do not damage the samples that they are irradiating. This trend allows neutron diffraction to be used as a NDE tool on actual parts and living things. Experiments can be designed such that the neutrons pass through experimental chambers while diffracting off a sample. This characteristic allows *in situ* experiments at temperature, under stress, or in a vacuum or corrosive environment.

The wavelengths of the neutrons involved in typical scattering experiments are similar to atomic-scale distances. Also, the neutron's energy is similar to that of the excitation and vibrations of atomic structures. The neutron has a magnetic moment allowing the neutron to be scattered by magnetic domains, revealing the magnetic structure of materials. The magnetic moment of neutrons is three orders of magnitudes lower than that of electrons. However, unlike electrons, neutrons do not scatter electrostatically so that the magnetic scattering is not overwhelmed.

As a crystalline material is put in a state of strain, the lattice spacing, d, is changed. If a sample in a diffraction experiment contains residual stresses or it is being strained *in situ*, the change in d also creates a change in the wavelength or scattering angle of diffracted neutrons. This detection of strain works well with both X-ray and neutron diffraction. X-rays, however, only show surface strains, while neutrons can penetrate deeply into a sample, allowing determination of average bulk strains.

For a spallation source (with a constant angle and many wavelengths), taking the derivative of Bragg's law (1) with respect to θ yields the following:

$$\Delta\lambda = 2\Delta d \sin\theta \tag{3.2}$$

Substituting (1) for sinθ

$$\Delta\lambda = \frac{\Delta d}{d}\lambda$$
$$\frac{\Delta d}{d} = \varepsilon = \frac{\Delta\lambda}{\lambda} \tag{3.3}$$

This shows that the strain is a function of the change in the wavelength of the diffracted beam for a spallation source with a fixed θ. A strained sample would have a small shift in the wavelength of the diffracted peaks versus that of an unstrained sample. The interaction between d-spacing and wavelength is also obvious from inspecting the derivation of Bragg's law [13]. This change in the wavelength is proportional to an energy change, which affects the speed of the diffracted neutron. In a spallation-neutron source, this difference is recorded as a difference in the time of arrival of the diffracted neutron at the detector. Given the

geometry of the instrument and the properties of the incident beam, the time difference can easily be converted into a d-spacing change.

A typical diffraction pattern for HAYNES 230 is shown in Figure 3.1. Using Rietveld refinement [16, 17], the entire pattern is fit, generating a lattice parameter (or parameters for non-cubic crystal structures). As elastic strain increases or decreases, the pattern changes and a new lattice parameter can be calculated. Comparing the initial and final lattice parameters, the elastic strain in the crystal can be calculated. Each peak in the diffraction pattern represents a specific *hkl* direction. Using least-squares methods, the peak position of each peak can be calculated very precisely. Comparing the changes in peak position as conditions vary within each sample can generate the *hkl* specific strains. Figure 3.2 shows the position shift in the 200 peak of Haynes 230 as load is applied. In this case, the position changes correspond to strains of 2300 με at 375 MPa and 5660 με at 700 MPa relative to the initial position of the 200 reflection with no load.

Since plastic strains are usually generated from a combination of dislocation motion and grain boundary sliding, this method is not directly sensitive to plasticity. Only elastic strains, generated from the stretching or compressing the interplanar spacing in the grains, are measured. Furthermore, the strains generated from this measurement are an average of the strains in all the grains that satisfy the Bragg condition for the particular scattering volume.

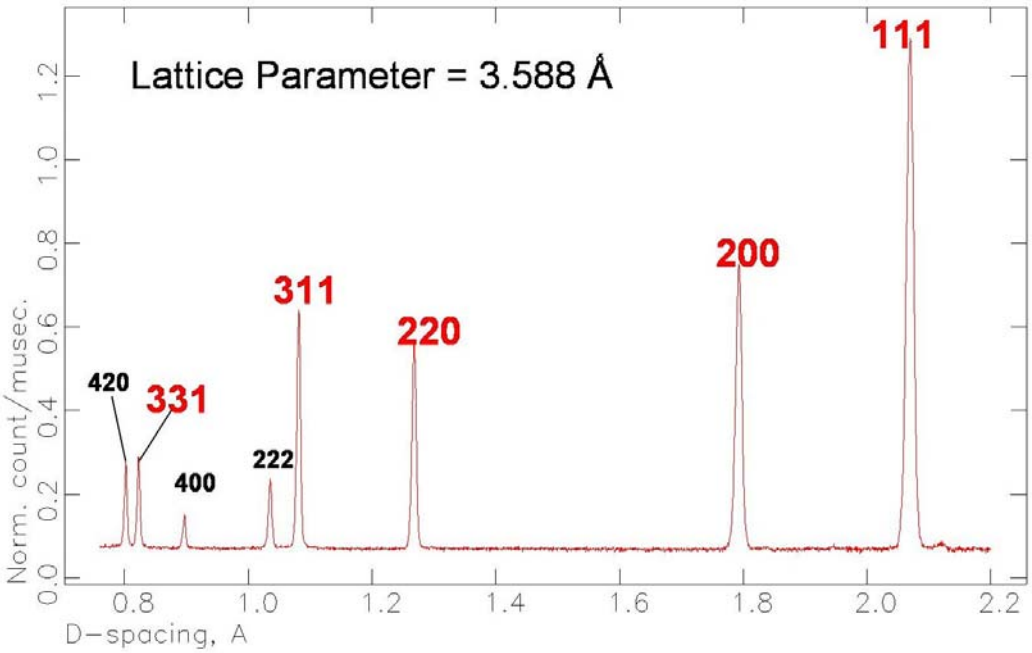

Figure 3.1: Neutron diffraction pattern of HAYNES 230 with the peaks indexed, taken on the SMARTS instrument. Lattice parameter derived from Rietveld refinement.

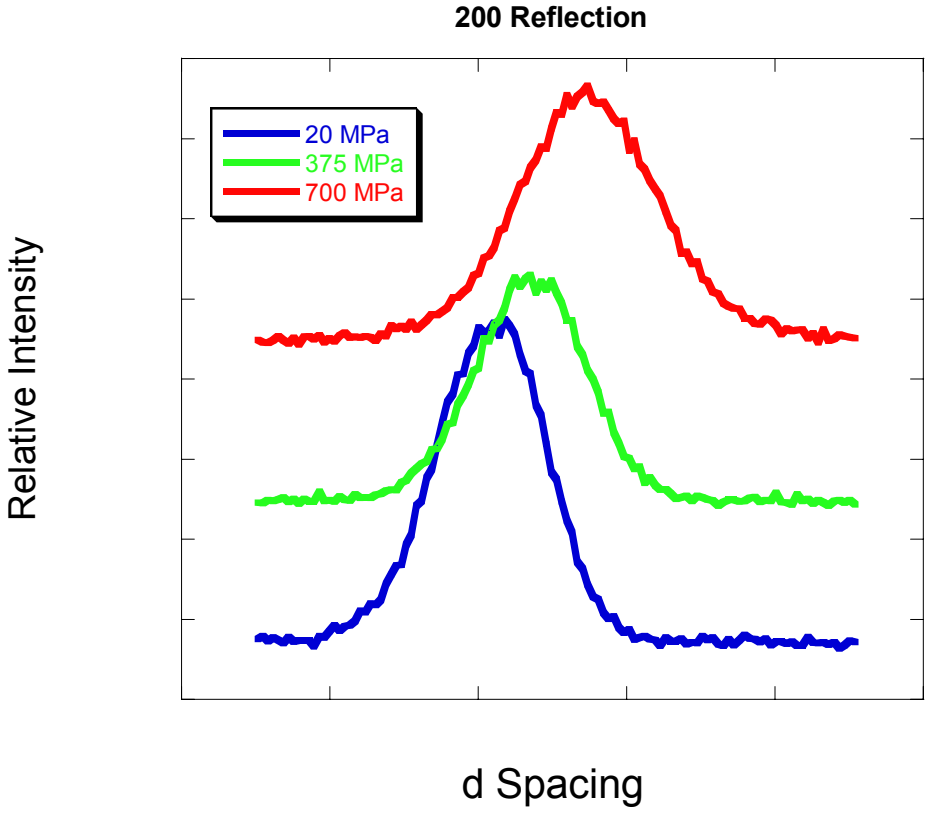

Figure 3.2: Change in the peak position of the 200 reflection in HAYNES 230 as load is applied.

The volume being measured is the intersection of the incident beam with the projection of the detector, (Figure 3.3). Using collimators, the size of the gauge volume can be changed. The resolution can be as small as 0.1 mm in projection, but it typically ranges from 1 to 6 mm in projection.

By translating this gauge volume through a sample, the complete three dimensional (3D) state of stress and strain can be determined for the sample. This strain mapping is a powerful tool for characterizing materials. Residual strains can be measured in actual parts. *In situ* mechanical, thermal and corrosion experiments can be carried out while monitoring the strain and microstructure of the sample. A 3D state of stress can be experimentally determined and compared to a finite-element model. The strain, stress and microstructure can be monitored *in situ* on a part that is being tested in a time-dependent operation, like fatigue, thermal cycling, or annealing.

3.2 *In Situ* Strain

Recently, at both reactor and spallation sources, a number of instruments dedicated to materials engineering and, specifically, *in situ* strain measurement have appeared or are in planning stages [18-21]. These instruments operate on simple principles. A uniaxial loading machine is placed in the beam line such that two sets of detectors can collect data coming from grains oriented parallel and perpendicular to the applied load. Using the same technique shown in Figure 3.3 to define the scattering volume, the sample is oriented at 45º to the incident beam (Figure 3.4) with two detectors placed at plus and minus 90º to the beam. A

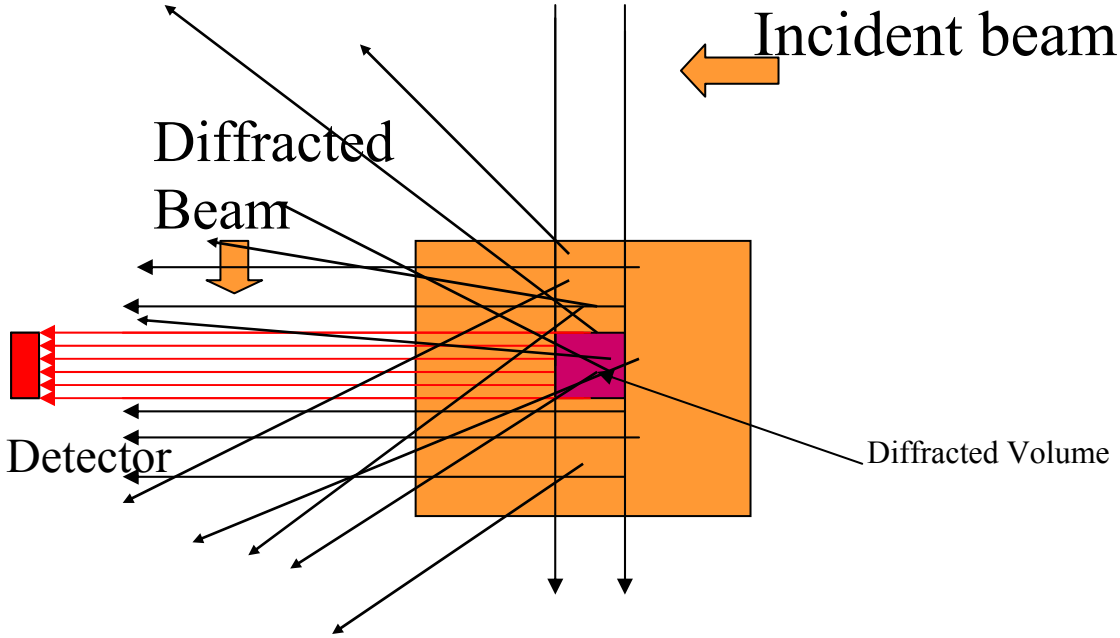

Figure 3.3: Geometry of strain measurements.

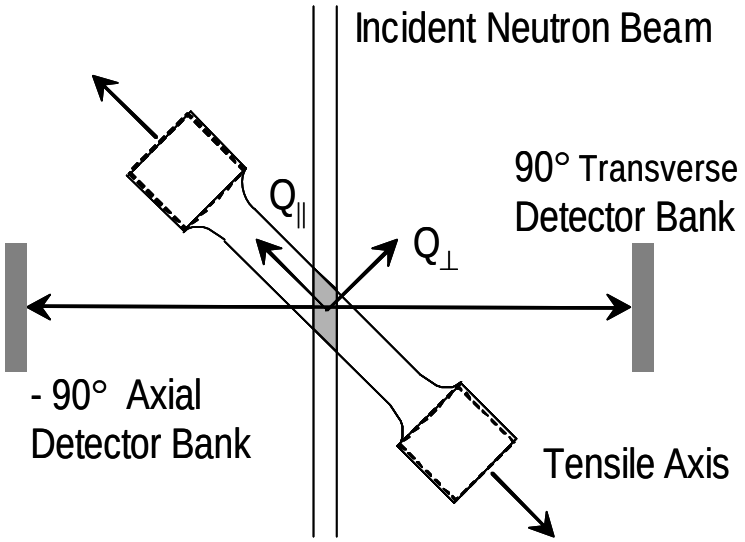

Figure 3.4: Geometry of *in situ* loading measurements at a spallation source [30].

schematic of the Spectrometer for Materials Research at Temperature and Stress (SMARTS) diffractometer [18] is shown in Figures 3.5 and 3.6. The transverse detector bank, +90º, measures the strain in grains with their plane normals oriented perpendicular to the applied load. This is the Poisson's direction during loading. The axial detector bank, -90º, measures the strain in grains oriented parallel to the applied load. This experimental setup, depending on the exact nature of the equipment used, can measure strains during a tension, compression, or fatigue test. The ENGIN-X diffractometer at the ISIS accelerator, at the Rutheford Appleton Laboratory (RAL) in England is a similar instrument (Figure 3.7) [19, 20]. Future instruments [21] will make use of tension/torsion rigs to explore the generation of internal strains during torsion.

In situ strain measurements can also be made at high energy X-ray sources, such as the Advanced Photon Source (APS) at the Argonne National Laboratory (ANL) [12, 22-24]. Instead of gaining diffraction information from a beam diffracted at 90 degrees to the sample orientation, as with the neutron diffractometers above, it is possible to obtain diffraction rings in transmission with macroscopic samples. In this case single wavelength X-rays of 0.1535 Å, 75 keV energy and a 150 μm x 150 μm beam spot size will yield a clean diffraction pattern through 1.5 mm thickness of a HAYNES 230 sample, ranging from roughly 0.5 to 4 Å in *d* spacing, depending on the sample to detector distance (Figure 3.8). Although the path length of X-rays is much shorter than neutrons, it is possible to pass through a few millimeters of a nickel superalloy with the high energy X-rays from the APS.

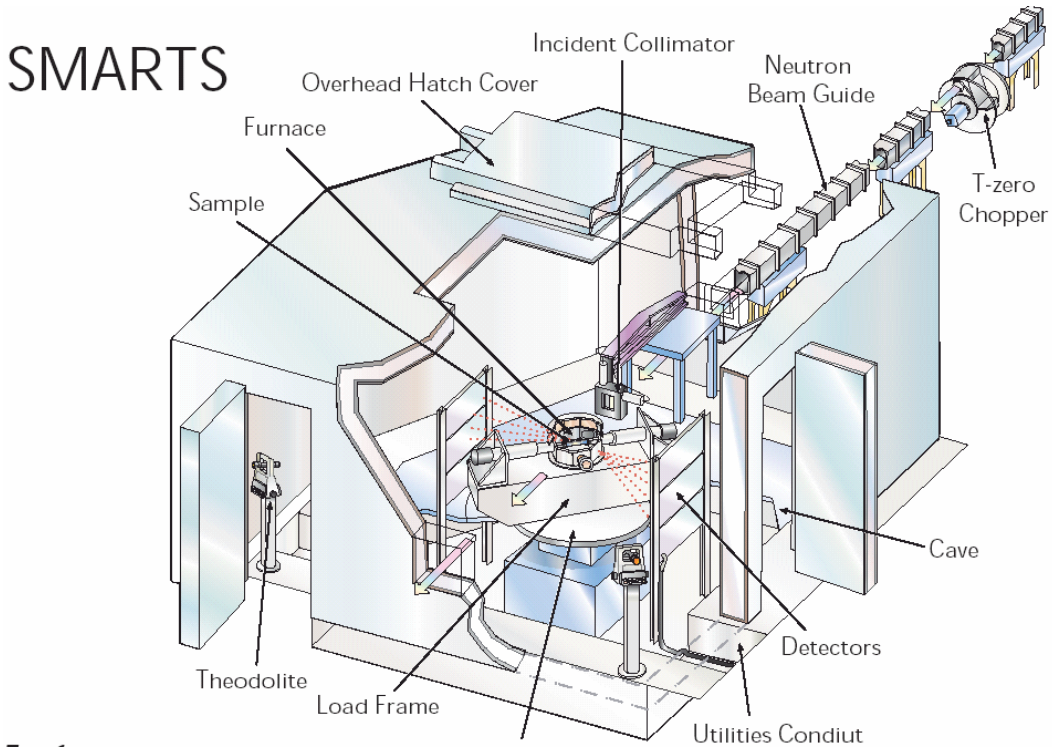

Figure 3.5: Schematic view of the SMARTS diffractometer, showing the load cell and furnace in the beam line [18].

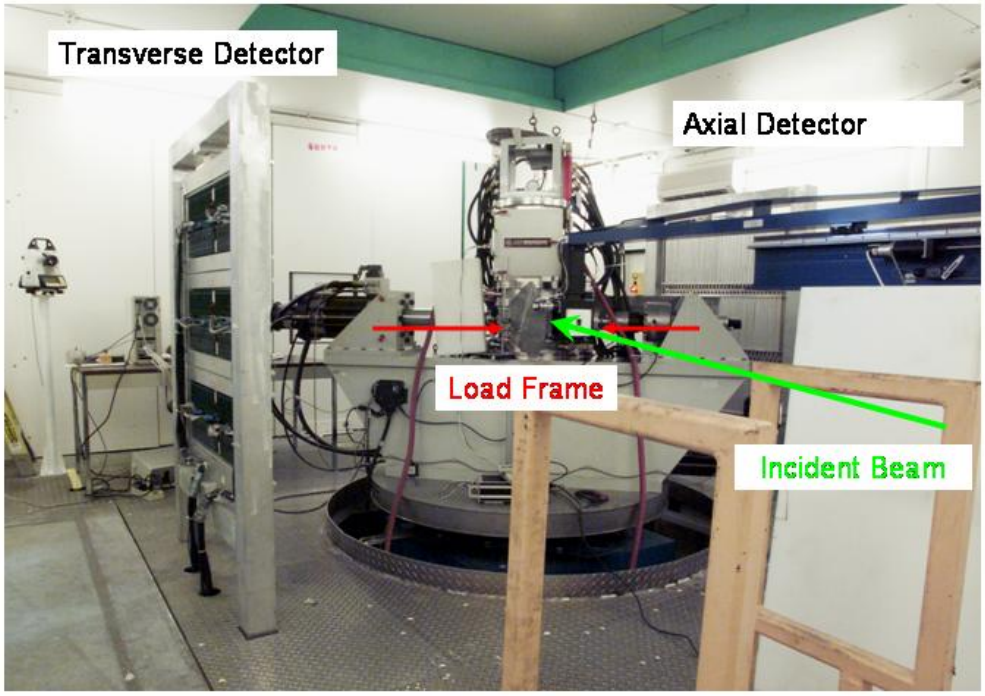

Figure 3.6: Photograph of the SMARTS diffractometer at the LANSCE facility at the Los Alamos National Laboratory, showing the axial and transverse detectorbanks, the load frame and the direction of the incident neutron beam.

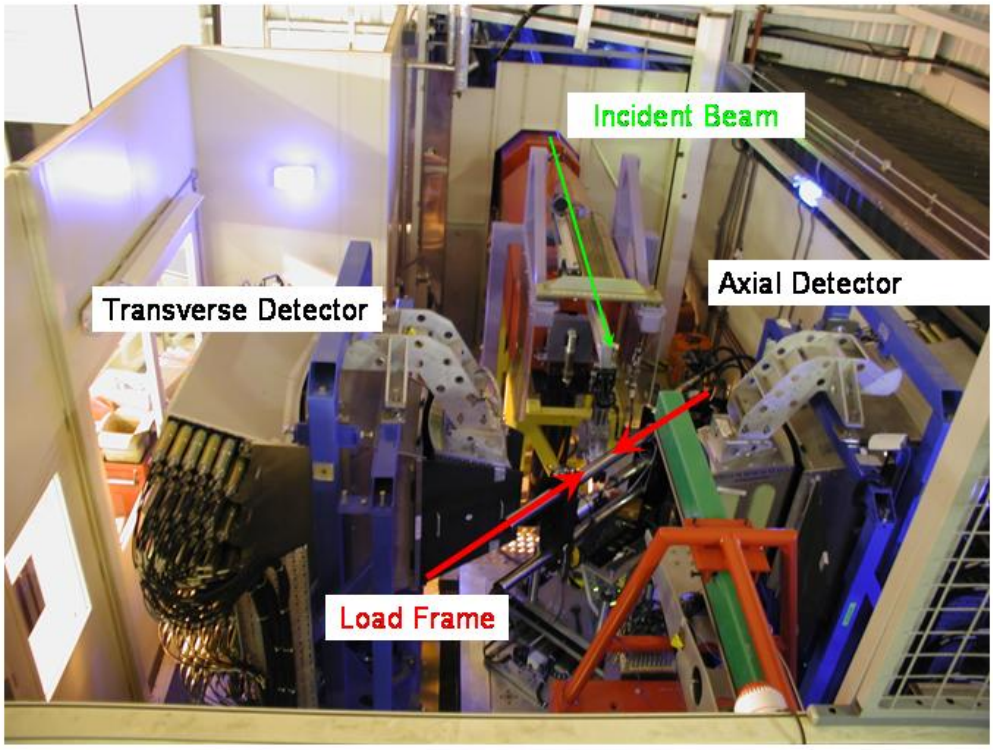

Figure 3.7: Photograph of the ENGIN-X Diffractometer at the ISIS facility at the RAL in England, showing the axial and transverse detector banks, the load frame and the direction of the incident neutron beam.

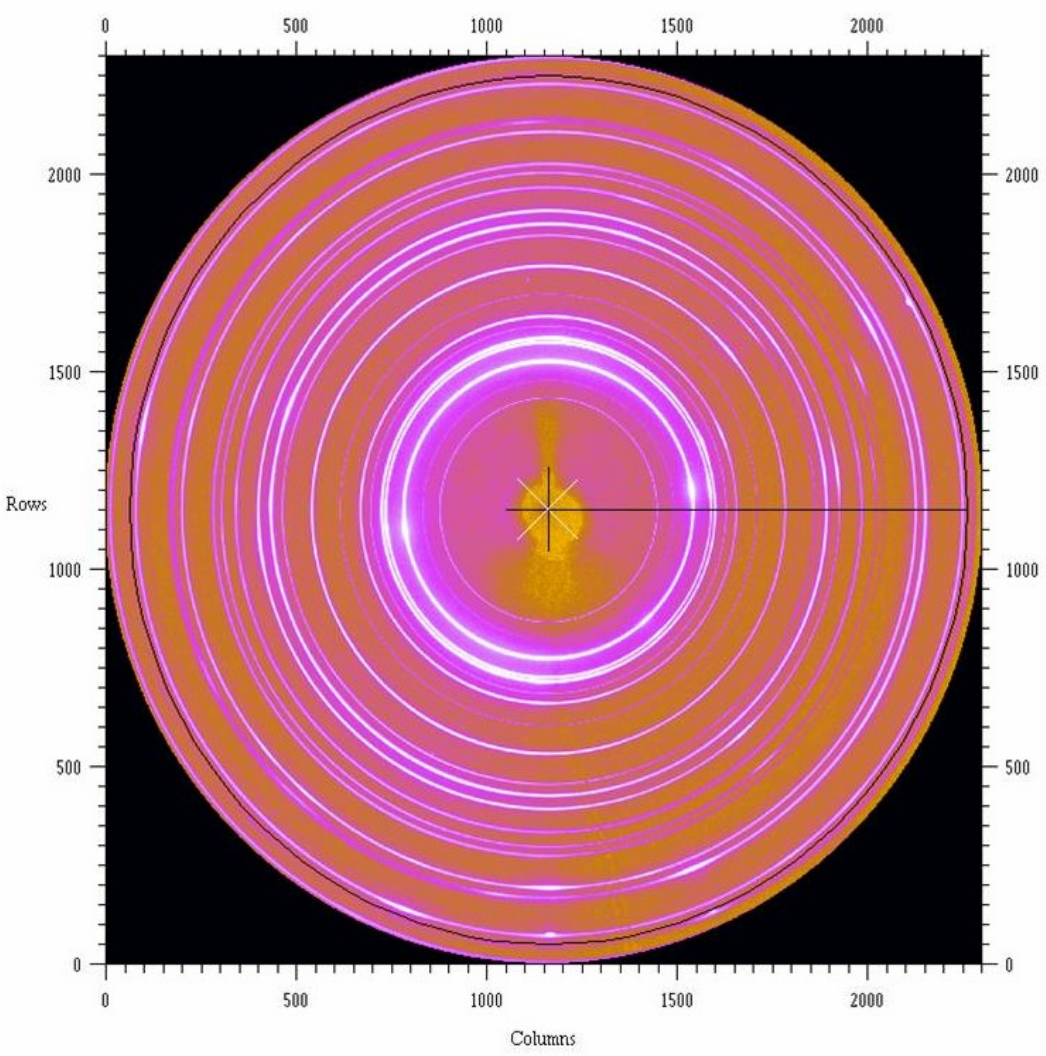

Figure 3.8: X-ray diffraction rings from HAYNES 230 taken on the 1-ID beam line at the APS.

The diffraction pattern for HAYNES 230 shown in Figure 3.8 was taken on the 1-ID beamline at the APS with the beamline configured with a simple screw-driven load rig in the beam, Figures 3.9 and 3.10. Integrating the diffraction rings across the 20 degrees centered on the sample's axis and at 90 degrees to the sample axis will yield a diffraction pattern that is similar to that recorded at the neutron instruments. However, in this case, the sensitivity to a smaller second phase, such as the carbide in HAYNES 230 is much higher. Figure 3.11 shows the higher *d* spacings of the diffraction pattern of HAYNES 230 showing multiple diffraction peaks from the M_6C carbide, as well as the ceria (CeO_2) peaks that were used to calibrate the diffraction patterns. This experimental setup was successful, but suffered from some large positioning errors due to the sample changing position with respect to the image plate as loading was applied. This led to large error bars on the strain measurements due to the inability to compensate for the position changes, despite having the ceria as a calibrant.

3.3 Texture

Closely related to the measurement of internal strains using diffraction, is the measurement of crystallographic texture [25-27]. In a powder, or randomly oriented solid, intensities of diffracted peaks in a diffraction pattern are dictated by the crystallography of the material and the structure factors for the given peaks. However, as a sample becomes more textured, the intensity is skewed by the number of grains meeting the diffraction condition. This change in texture is usually due to grain rotation, which is a method of accommodating internal

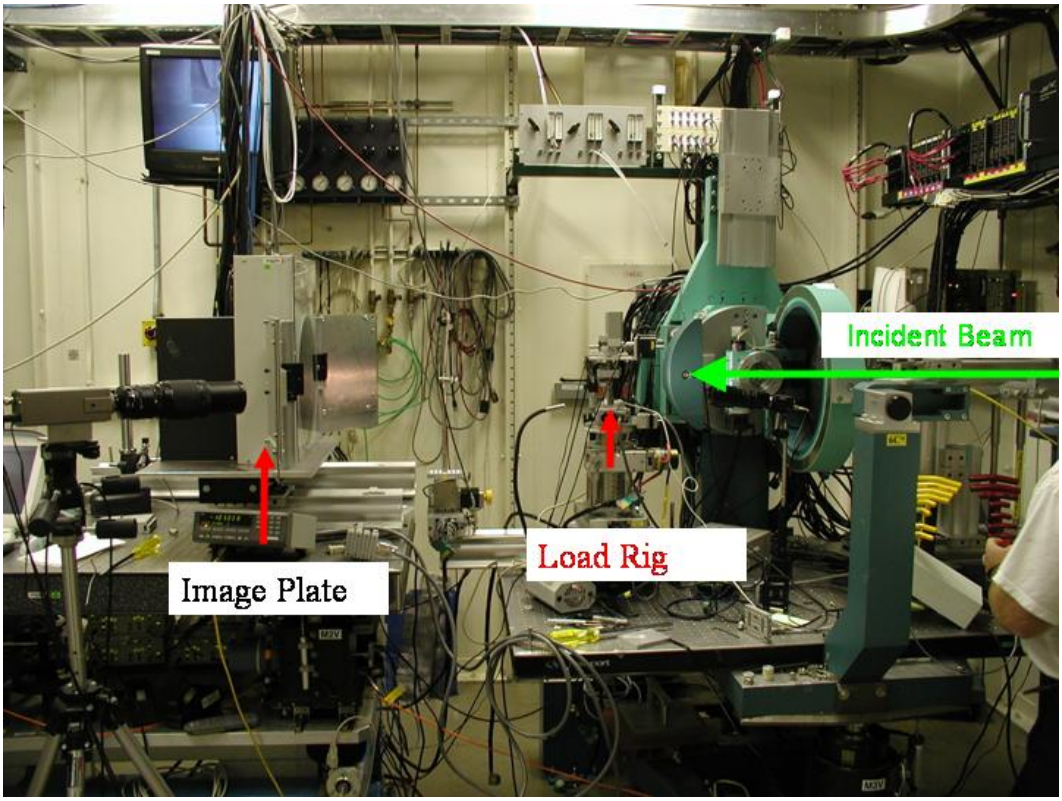

Figure 3.9: Photograph of the 1-ID beamline at the APS at the Argonne National Laboratory, showing the image plate, the load rig and the direction of the incident X-ray beam.

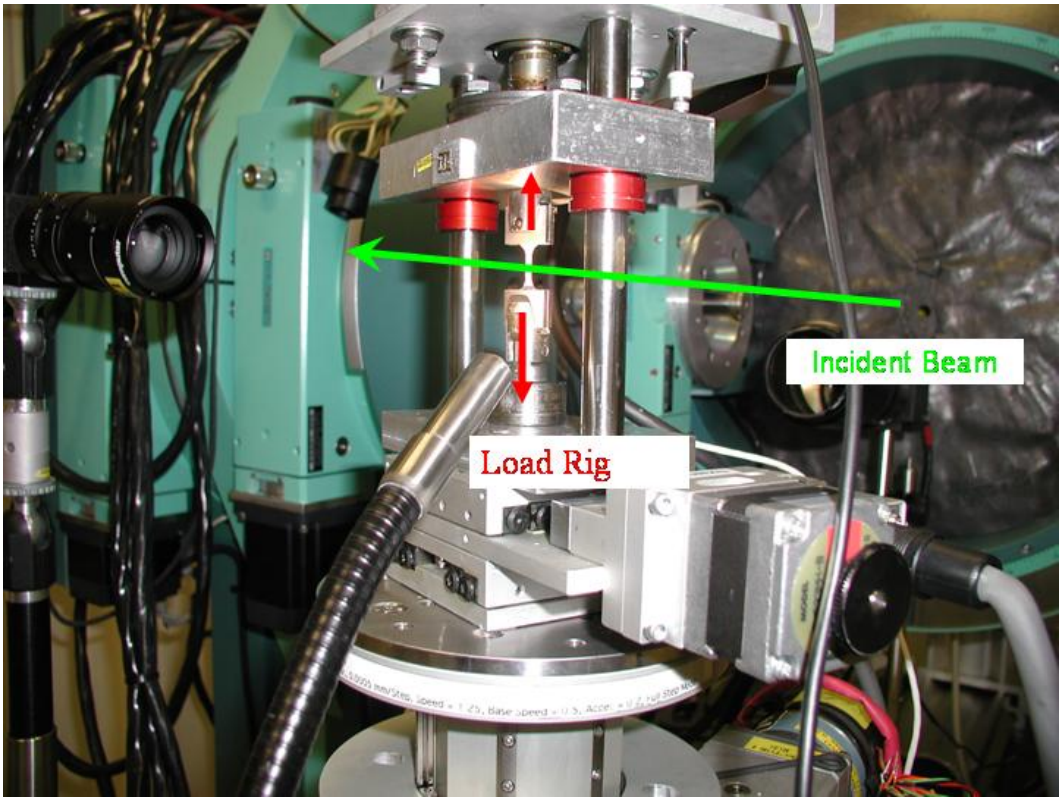

Figure 3.10: Close-up photograph of the load rig on the 1-ID beamline at the APS at the Argonne National Laboratory

.

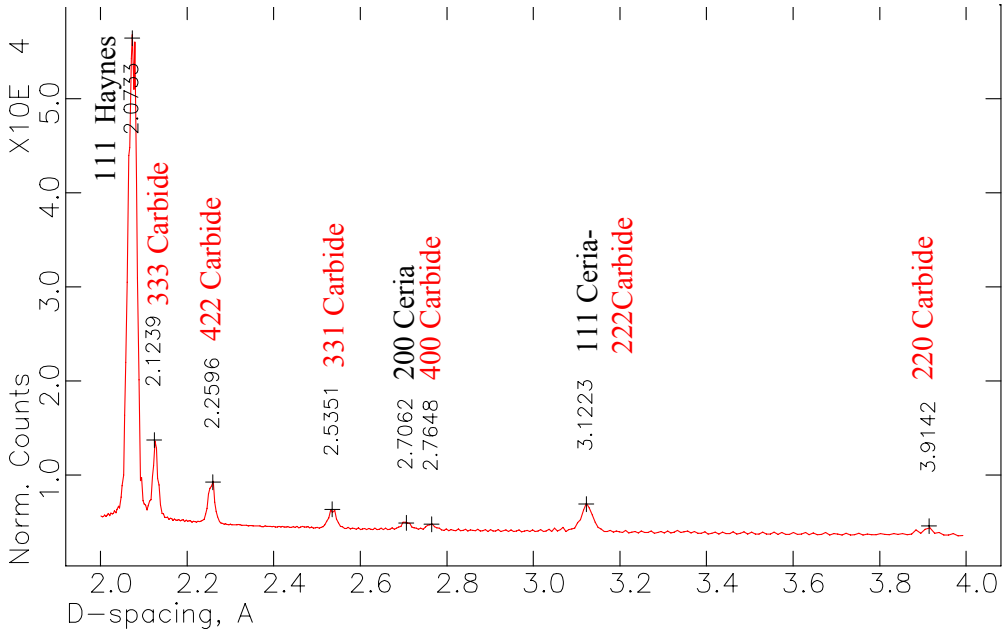

Figure 3.11: X-ray diffraction pattern of HAYNES 230 with the carbide peaks highlighted, taken on the 1-ID beam line at the APS.

strains. Twinning will also result in large quick changes in texture development. As a sample is loaded in tension the diffraction pattern will show both a shift in peak position from elastic strain, and change in peak intensity due to changes in texture, Figure 3.12.

The High Pressure Preferred Orientation Diffractometer (HIPPO) [28, 29] at LANSCE is optimized for quickly measuring texture in metallic, geologic or biological samples, Figure 3.13. The diffractometer has 50 banks of detectors so complete pole figures can be measured with 4 rotations. Each bank of detectors yields a separate diffraction pattern which corresponds to a different orientation on a pole figure. The patterns are fit using Reitveld refinements with spherical harmonics to accommodate changes in texture. A texture pole figure is, then, generated from the combined texture information from all the diffraction patterns [28, 29]. The texture pole figures seen in Figure 3.14, for example, are generated from 98 unique diffraction patterns accomplished by four sample rotations in the HIPPO diffractometer. These pole figures show a typical fiber texture achieved by tensile deformation on an originally untextured FCC alloy, in this case Haynes 230 after tension to 700 MPa.

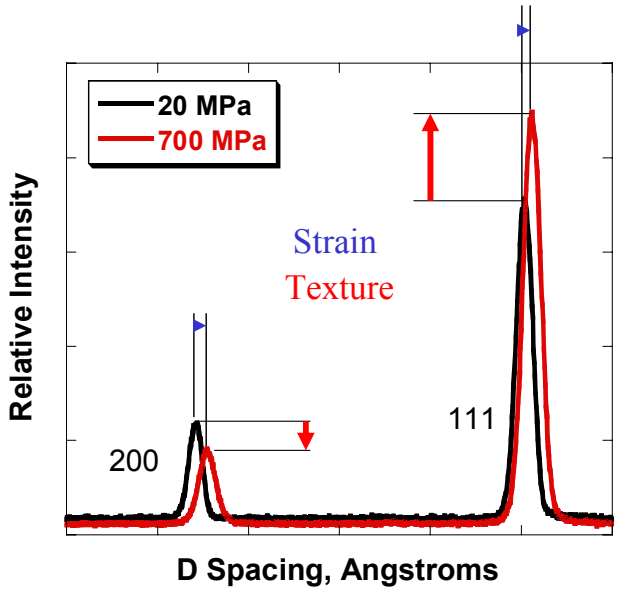

Figure 3.12: Intensity change due to texture and peak position change due to strain in the diffraction pattern of HAYNES 230 as it is loaded from 20 MPa to 700 MPa.

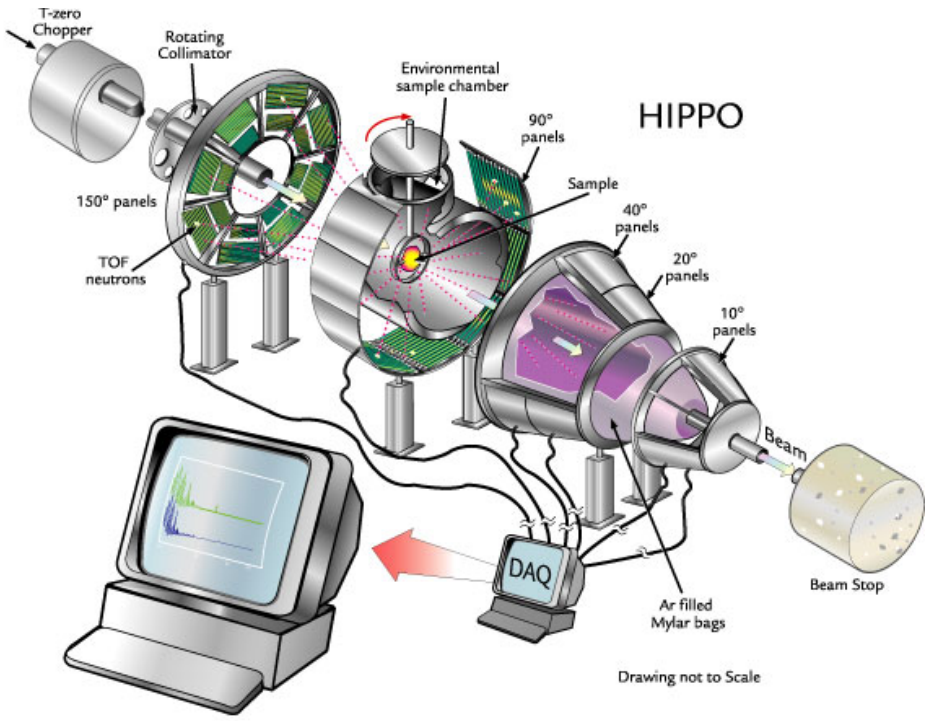

Figure 3.13: The High Pressure Preferred Orientation (HIPPO) Diffractometer at LANSCE [29].

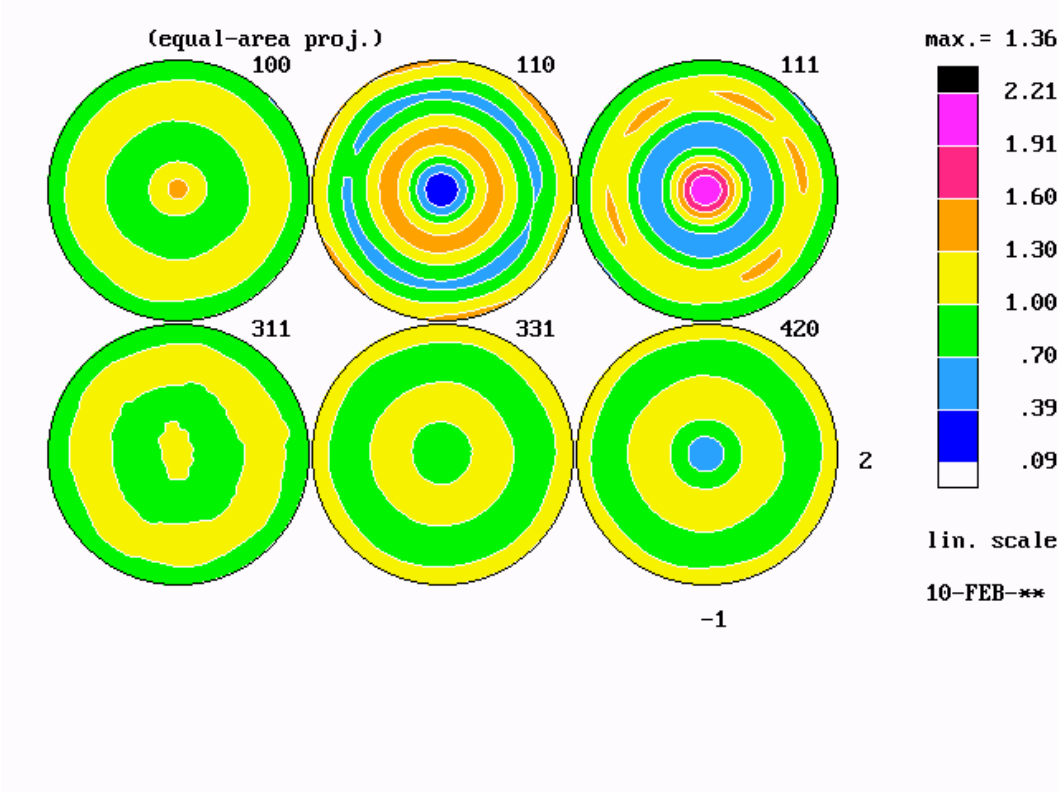

Figure 3.14: Texture pole figures measured on the HIPPO diffractometer for HAYNES 230 after a tensile experiment.

Chapter 4

Literature Review

4.1 *In Situ* Loading

While the measurement of strain using neutron diffraction techniques has been known for some time [14, 31-33], the concept of *in situ* measurement of strains during loading using neutrons has become a relatively recent phenomenon [32, 34]. The advent of materials science based neutron diffractometers with the instrument and scattering geometry optimized for strain scanning and *in situ* loading experiments is less than two decades old. Dedicated instruments for *in situ* strain measurement at neutron sources were pioneered at the Neutron Powder Diffractometer (NPD) [35, 36] at LANSCE and the ENGIN Diffractomer at the ISIS accelerator [19, 37]. The recent addition of the SMARTS diffractometer at LANSCE [18] and the ENGIN X diffractometer at ISIS [19, 20] have brought the field into maturity. Next generation instruments such as VULCAN at the SNS [21] and dedicated beamline and instruments at high energy synchrotron X-ray facilities [23] will push the field further.

In situ loading experiments have existed since 1925 when X-ray studies of loading of steel ribbon were undertaken by Lester [38]. The loading was horizontal, accomplished by hanging a weight off of a string and pulley system while diffraction patterns were being exposed. Wood and coauthors, starting in the late thirties conducted a series of *in situ* loading experiments, both tension and

compression, on full size specimens of copper, aluminum, iron, steel and brass [39-47], thus introducing the concept of lattice strain versus applied load plots. These studies were instrumental in helping clarify the role of crystalline anisotropy during loading as well as anisotropy's effect on residual strain [48-51]. Additional *in situ* and *ex situ* studies on creep and fatigue of metals were conducted through the late thirties through the 1960's [47, 52-55]. By the early 1960's X-ray studies were being used to single out the reactions of different phases of composites during loading [56, 57].

The addition of time of flight neutron diffraction at high intensity neutron sources has improved this technology greatly [34]. The ability to take full diffraction patterns without moving the sample or load rig has increased accuracy, experimental breadth and decreased experimental time. This work has come to maturity with the ability to accurately model lattice strains in metals with high symmetry structures. Most clearly, the using the elastic-plastic self consistent modeling EPSC technique to isolate and model strains in individual grains during loading [58-61]. Starting with the concept of an Eshleby inclusion in a homogenous matrix [62], which was originally conceived as a way of modeling composite structures, and then applying the model to a specifically oriented grain of material in a homogenous equivalent matrix (HEM) consisting of a single phase that has the properties of the entire material. In this fashion the reactions of the oriented particle to an applied load, within the constraints of the rest of the material, can be predicted. With computer simulations this can, through an iterative process, accurately predict the results of each grain orientation to an

applied load, the *hkl* specific elastic strains, and compare it to experimental results [59, 63-69]. Although it is more difficult due to higher crystal asymmetry, this method can be applied to hexagonal close packed materials, such as beryllium and magnesium [30, 70-74], as well as ongoing programs to expand this method to lower symmetry materials, such as uranium. Keen understanding of slip, twinning and other deformation mechanisms must be in hand before this model will accurately predict behavior in lower symmetry metals, thus, this is the subject of ongoing preliminary deformation studies [75, 76].

Although efforts are ongoing to apply these EPSC models to two phase materials, right now this has been applied only to materials with voids, with an Eshleby inclusion consisting of a combined grain and void inclusion [77]. For composite materials, simple finite element models of a representative microstructure can accurately predict macroscopic strains as well as, due to the bulk averaging nature of *in situ* neutron diffraction measurements, elastic lattice parameter strains [78].

As mentioned, the ability of neutron diffraction to record unique diffraction patterns from each phase of a composite material, allows one to generate separate strain measurements for each phase in the material and investigate load sharing mechanisms between phases in composites. Using diffraction to study multi-phase materials such as composites has been frequently used since the 1960's [35, 36, 56, 57, 79-83]. More uniquely, *in situ* diffraction has been used to study materials that are not normally considered classic composites, such as yielding in reinforced or semicrystalline BMG's [78, 84, 85],

load sharing in γ -γ' type superalloys [86, 87], as well as interphase load sharing in various steels [66, 68].

4.2 Fatigue Studies

The use of *ex situ* and *in situ* X-rays to study fatigue has been around since the late 1930's [52, 54, 88]. While results show clear effects of fatigue, the results are limited by studying surface effects. More systematic studies involving X-rays to study tension-tension and tension-compression fatigue in steels have been undertaken [89, 90]. Again these studies look at the effect of surface residual stresses and the effect of these stresses on the fatigue life, rather than bulk changes in the lattice response as fatigue progresses.

To date, there has been little published on the use of neutron diffraction to study fatigued materials. Previous studies using neutrons have explored only eight cycles [65] or have compared the internal strains between different samples that had been fatigued outside the neutron instrument (*ex situ*) [91]. The former experiment showed the development of approximately 150 με over the first 8 cycles of low-cycle fatigue. The latter showed residual strain development of roughly 500 με and the subsequent relaxation to no residual strain over the course of 90% of the fatigue life of a high-cycle (stress controlled) full reversal fatigue test. However, since the second study was based on experiments performed *ex situ*, the strain development was not tracked across a single sample.

Additional studies using stroboscopic methods have explored the development of internal stresses due to mechanical and thermal fatigue [92-95]. These methods are useful in measuring average strains across the same condition (stress or temperature) over many cycles, especially when the cycles and hold times are much shorter than the time it takes to collect a diffraction pattern. However, they are insensitive to large changes over a small number of cycles, especially over current "typical" diffraction time. This technique becomes much more viable as neutron flux increases with the next generation of spallation sources, such as the Spallation Neutron Source, and its next generation strain diffractometer, VULCAN [21]. Similarly the addition of a fatigue rated MTS load frame and a high speed image plate [96] on the 1ID beamline at the APS [23] will add very high speed fatigue and image recording capabilities, allowing for real frequency (1-10 Hz) fatigue experiments and potential for even higher frequency stroboscopic measurements.

There have been a number of studies using *in situ* diffraction to look at stress induced phase changes, especially martensitic type, during fatigue. In particular the behavior of shape memory alloys [97, 98] has been studied over the course of a small number of cycles, showing both texture and phase changes as cycling progresses. Studies on stress induced phase changes in austenitic stainless steel have been undertaken [99, 100], however, the fatigue has generally been accomplished prior to the *in situ* loading to look at the load sharing between austenitic and martensitic phases as the phase fraction changes with increasing fatigue life. Similarly, Ultimet, a cobalt based superalloy, has been the subject of

both X-Ray and neutron diffraction based studies on phase change during fatigue [101-103]. Significantly, both low cycle and high cycle fatigue has been studied, as well as large numbers of cycles. Although the primary focus of these studies has been the mechanism and result of phase changes during fatigue, the progression of internal strains have been noted as well.

4.3 Texture

Texture describes the orientation of a polycrystalline solid [25-27]. The concept has been applied to geologic materials since the early 1800's [104], when it was realized that the method of formation affected the orientation of grains in rocks. The term texture was applied by 1850 [105]. Initial studies of texture were simply based on observing and counting grains of certain orientation in micrographs. X-ray diffraction intensity was used to study texture in metals in the 1920's [106]. Quantitative studies of texture using X-rays occurred in the late 1940's with the technique of using Geiger counters and goniometers [107, 108], roughly coincident with better understanding of anisotropy's role in *in situ* loading [48-50].

Application of neutron diffraction to texture measurement began in the 1950's [109] and continues until today [28, 29], spurred on by the development of high intensity neutron sources, advanced instrumentation and the inherent advantages of neutrons described in previous chapters.

4.4 Nonlinear Resonant Ultrasound Spectroscopy

Nonlinear resonant ultrasound spectroscopy (NRUS) is a specialized subset of resonant ultrasound spectroscopy (RUS) techniques, often used for evaluating elastic constants in materials [110-114]. By measuring the elastic resonance frequencies of a sample using small perturbations created by ultrasonic frequencies, the elastic tensor of a solid can be extracted. This method works well with homogenous solid samples of precise dimensions, such as single and polycrystalline metals in an undamaged state [115-119]. However, recent advances coupling RUS techniques with finite element methods have allowed determination of elastic constants in more complex materials like composites[120, 121], bones [122], and rocks [123, 124]. Similarly, inelastic effects can be characterized using RUS such as microcracks in ceramics [125, 126] and internal friction in metal hydrides [127].

Studies on less coherent materials such as rock and bone using RUS determined that there were a host of non-linear effects that take place in materials that are inhomogenous or damaged [128-131]. As resonant frequencies were driven to higher powers, the resonant peaks shifted in damaged materials allowing for a qualitative measurement of damage. An obvious application of this technique is to progressively fatigued materials, however only simple studies on materials such as concrete [130] and bone [122] have been accomplished to this point.

4.5 Infrared Thermography

The relationship between temperature and deformation has been known for centuries [132]. Elastic and inelastic deformations of materials produce thermal effects that can be related to their stress and strain state. Starting with early recognition of the role of plastic deformation creating heat in worked objects [133], to the study of the thermoelastic effect in metals [134, 135], to the quantification of the temperature rise at a crack tip [136], research has built to the point of understanding all factors generating heat during deformation and fatigue processes. With recent advances in equipment, infrared thermography can be used as a quantitative NDE technique for monitoring fatigue tests *in situ* [137-140]. The IR camera records the intensity of infrared waves emanating from a sample. The intensity of the IR radiation scales with the temperature of the sample. Fatigue damage results from the elastic and inelastic behavior in the material. Elastic and inelastic materials have distinct temperature signals, which can be monitored in-situ by IR thermography. Excellent background on the technique and cutting edge methods of applying IR thermography to fatigue are available through the work of Jiang and Yang [102, 103, 137-147].

Chapter 5

In Situ Loading Experiments

5.1 Background Experiments

Two relevant, but unpublished, studies conducted by the author and collaborators are instructive background to the HAYNES 230 results presented: a recently completed study on the *in situ* loading behavior in HASTELLOY C-2000 alloy [148], and a study on *in situ* loading of particulate reinforced aluminum alloys [149]. HASTELLOY C-2000 is a very similar alloy to HAYNES 230. It is a FCC solid-solution strengthened nickel-based superalloy, however, without the benefit of carbide strengthening. Figure 5.1 shows the *in situ* loading behavior of HASTELLOY C-2000. The internal strains are typical for an FCC alloy [59, 69]. The elastic anisotropy follows convention with the 200 direction taking up most of the elastic strain after yield, while the 311 takes up somewhat less elastic strain. The 111, 220, and 331 directions take up very little of the elastic strain. Upon unloading, the residual strains balance out with the 200 direction being very positive, while the 311 direction being approximately zero and the remaining directions having negative residual strain. This is absolutely standard behavior for FCC metals, showing the elastic anisotropy expected and seen in single-phase alloys like stainless steel, aluminum, and nickel [59, 69].

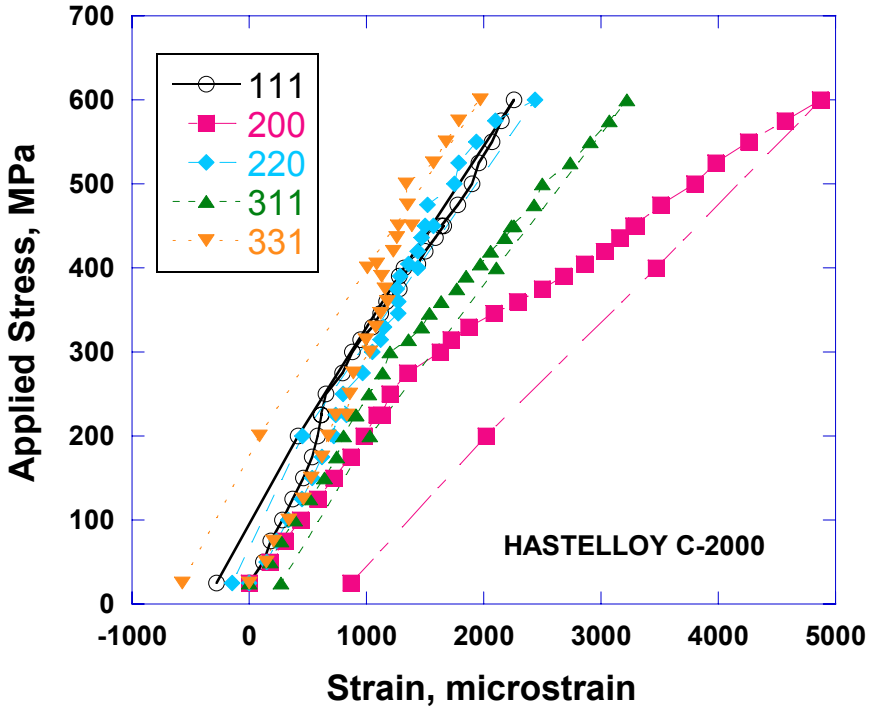

Figure 5.1: Internal strains generated during the *in situ* tension test, axial direction in HASTELLOY C-2000 alloy.

The second study is of a precipitate-strengthened 7075 aluminum alloy reinforced with approximately 20% $MgZn_2$ precipitates. Shown in Figure 5.2, there is a very homogenized lattice response in both the matrix and the carbide. Essentially, the strengthening mechanism is such that the MgZn2 takes up all the elastic strain, while the aluminum matrix behaves almost completely plastically. This homogenization has its roots in the generally isotropic behavior of aluminum, especially when compared to that of nickel. The Zener Anisotropy Ratio is defined as:

$$A = 2C_{44} / (C_{11} - C_{12}) \tag{5.1}$$

With C_{11}, C_{12} and C_{44} being material stiffness'. A is 1.22 for Al, making it virtually isotropic, as compared to 2.33 for nickel alloys and 2.5 on average for FCC metals [150]. Despite the isotropic behavior, the load sharing is completely consistent with the behavior of metal-matrix composites under *in situ* loading [35, 36, 79, 81-83].

5.2 Results

This chapter involves *in situ* tension and compression studies. These experiments provided a baseline measurement for fatigue experiments (Chapter 6), detailing the behavior of the alloy in a single cycle of fatigue. The carbides present in the alloy not only affected the loading behavior, but they produced a tension compression asymmetry, which motivated the present study of the

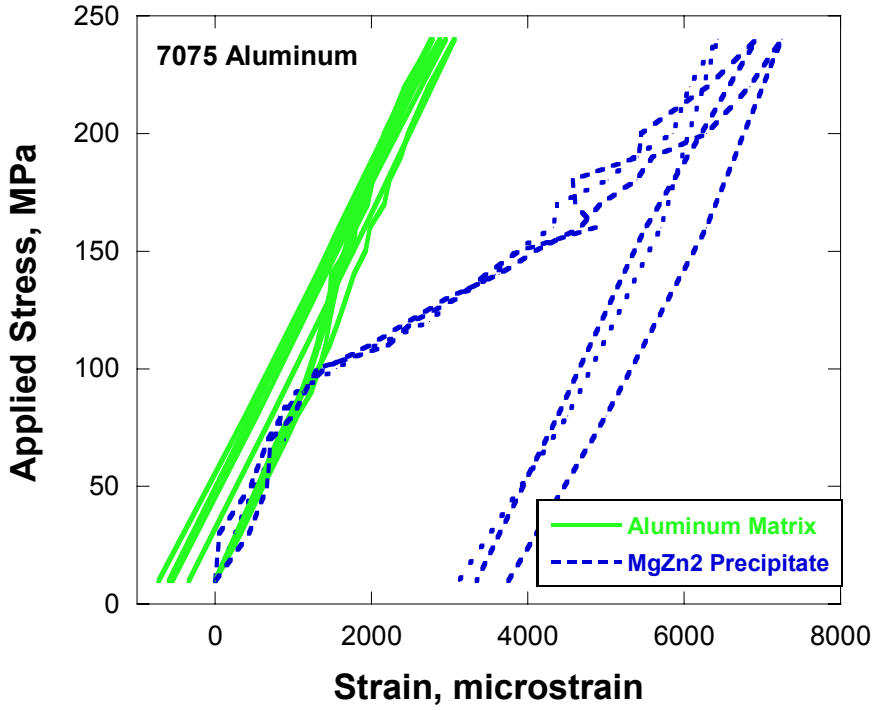

Figure 5.2: Internal strains generated during the *in situ* tension test, axial direction in 7075 aluminum alloy.

carbide-matrix interaction in this material. *In situ* tension and compression experiments using neutrons were performed at the SMARTS diffractometer at LANSCE while an additional *in situ* tension experiment, using high-energy X-rays, was performed at the 1-ID beamline at the APS.

For the neutron experiment, cylindrical tensile specimens were cut from a 13 mm thick plate, with a gauge length of 50 mm and a diameter of 6 mm. The specimens had a surface roughness of 0.2 μm along the gauge-length section. The ends of the specimens were threaded with a ½" UNC 13 thread [7]. Compression specimens were cylinders of 20 mm in length and 10 mm in diameter [8]. The *in situ* X-ray sample was a small dogbone tensile sample, 1.5 mm thick by 2 mm wide.

Both single-peak fitting and Rietveld refinement were performed on the diffraction patterns to yield the *hkl*-specific and lattice-parameter strains, respectively [16]. All strains reported below are relative to the starting condition of each sample under a nominal holding stress of 20 MPa in tension and -10 MPa in compression. Diffraction patterns are shown in the Chapter 3, Figures 3.1, 3.8, and 3.11. In the neutron data, the carbide peak was only resolvable in the transverse diffraction bank, due to being overwhelmed by background scattering in the axial direction. The experimental carbide data from the neutron experiments presented is specific to this reflection and is not based on Rietveld-generated lattice-parameter strain. As explained previously, despite the cleaner diffraction patterns for the carbide reflections recorded in the *in situ* X-ray diffraction experiment, positioning uncertainty during the experiment led to large errors in

the measurement of strain. Thus, the only carbide lattice parameter strain presented from the X-ray experiment is in the axial direction.

In the *in situ* neutron experiment in tension, the specimen was loaded incrementally from 20 MPa to 700 MPa and then unloaded to 20 MPa. The loading was paused for 10-15 minutes after each stress increment to collect diffraction patterns. Measurements were made at twenty-two stresses during loading and three during unloading (Figure 5.3). Similarly, in compression, a sample was loaded from 10 MPa to 605 MPa, pausing for diffraction patterns at thirty-nine stresses during loading and four during unloading (Figure 5.3). Finally, during the X-ray experiment, the sample was loaded from a nominal holding stress of 10 MPa in approximately 10-20 MPa increments to 630 MPa and then unloaded to 10 MPa in 6 steps. Loading was paused for approximately 5 minutes at each load level for diffraction patterns to be recorded.

Figure 5.3 shows the macroscopic stress versus strain curve during the *in situ* tension and compression experiments on SMARTS. Beyond the macroscopic yield stress of 390 MPa, creep occurred at a constant load during the hold time while the diffraction data was collected, resulting in the plateaus visible in Figure 5.3. The total macroscopic strain during the tension test was just over 15%, while it was approximately 7% in compression.

The lattice strains for 5 *hkl* reflections measured parallel and perpendicular to the load are plotted against applied stress in Figures 5.4 and 5.5, respectively. With respect to the tension-tension fatigue data presented in Chapter 6, this experiment corresponds to a single cycle of fatigue. The differences in the plane-

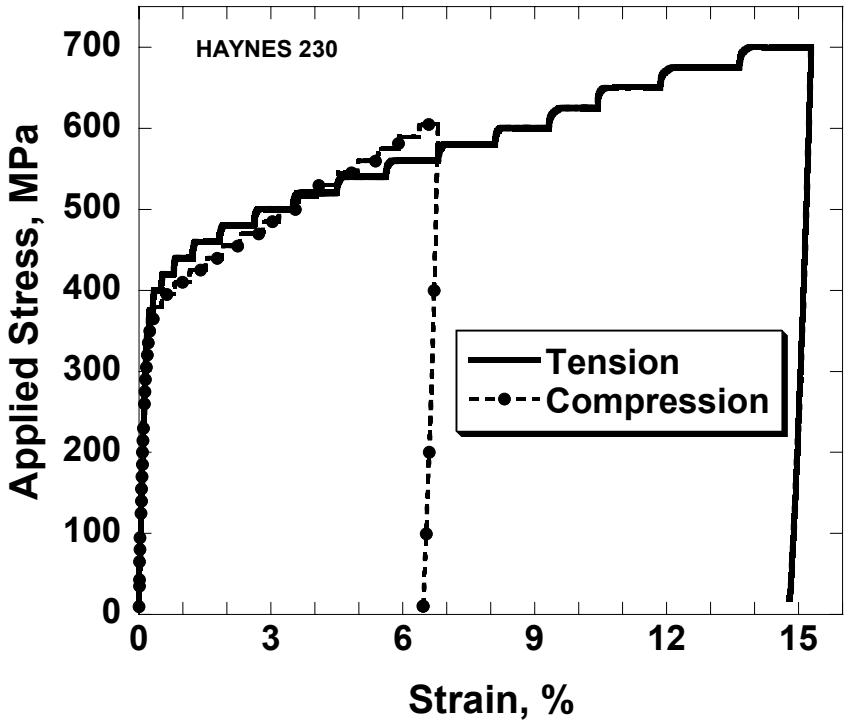

Figure 5.3: Macroscopic stress versus strain curve of HAYNES 230 during the *in situ* tension and compression tests.

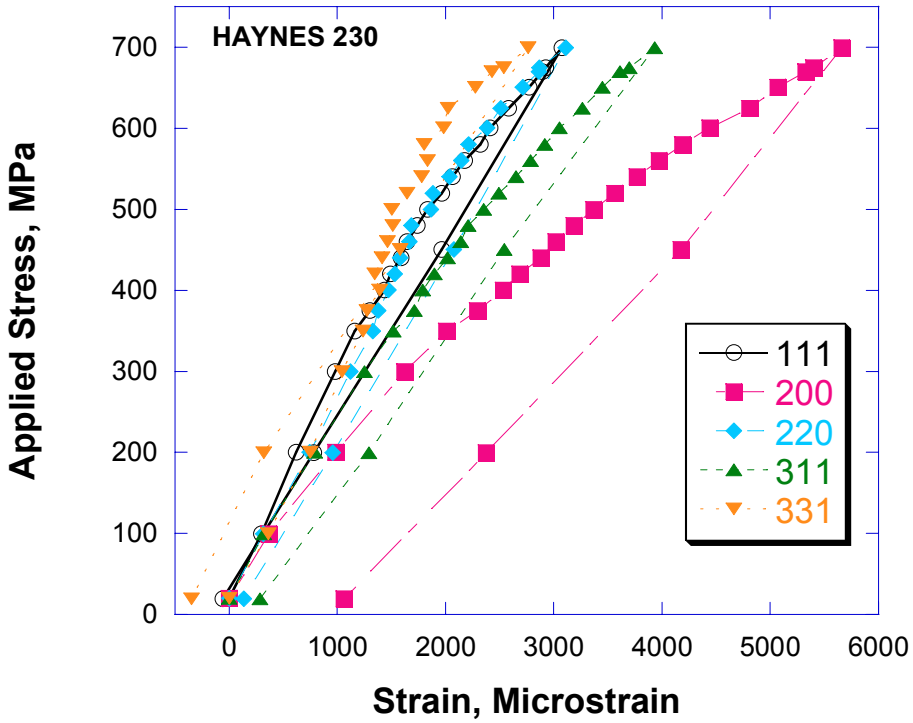

Figure 5.4: Internal strains generated during the *in situ* tension test, axial direction.

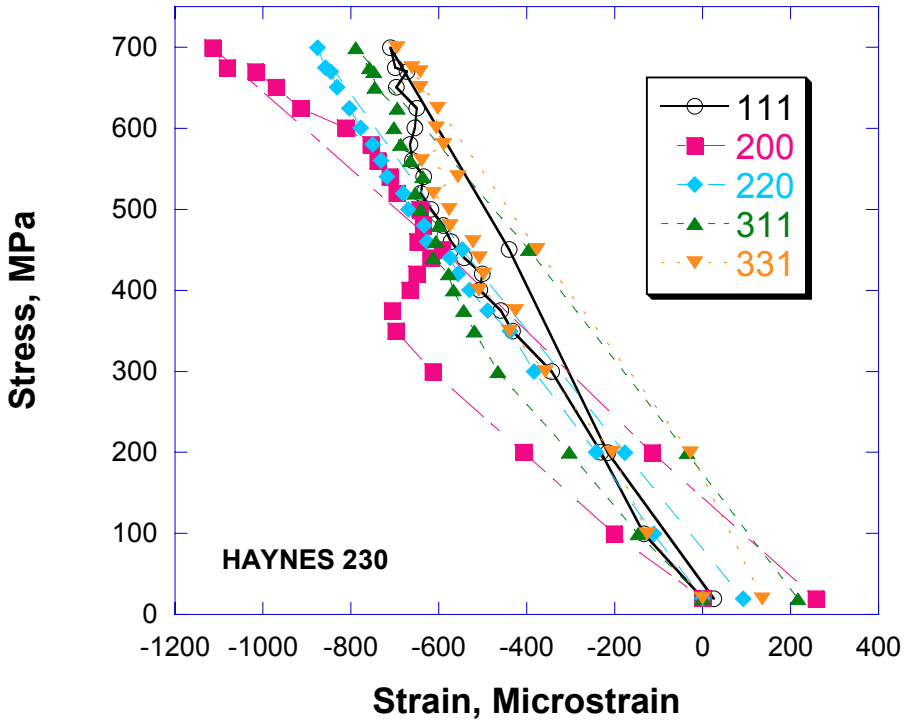

Figure 5.5: Internal strains generated during the *in situ* tension test, transverse direction.

specific moduli are apparent in Figure 5.4. In the axial direction, parallel to the applied stress, the 111, 220, and 311 reflections have moduli of 284, 248, and 221 GPa respectively, contrasting with the 162 GPa moduli of the 200 direction. The 200 reflection exhibits the most strain at the peak stress of 700 MPa. Notably, in both the axial and transverse directions, the residual strains are overwhelmingly positive. This is distinct from the typical balance of residual lattice strains upon unloading exemplified by the C-2000 data presented in Figure 5.1. It is also notable that the behavior is distinct from the typical composite load-sharing behavior seen in the 7075 Al alloy seen in Figure 5.2. The behavior of the 200 matrix *hkl* strains in the X-ray and neutron experiments are presented in Figure 5.6. Despite the larger error bars in the X-ray experiment (approx. 400 με for the matrix, 1000 με for the carbide) the data shows the same results, and the use of carbide data from the X-ray experiment is justified.

The lattice strains for the compression experiment in the axial and transverse directions are plotted in Figures 5.7 and 5.8, respectively. Since the peak stress was 600 MPa in compression, the magnitudes of the residual strains are not comparable to the *in situ* tension test, however, the sign of the residual stresses upon unloading are significant. In the axial direction, the residual strains are mostly positive, while in the transverse direction, they are mostly negative. This contrasts to the overwhelmingly positive residual strains in both directions in tension (Figures 5.4 and 5.5).

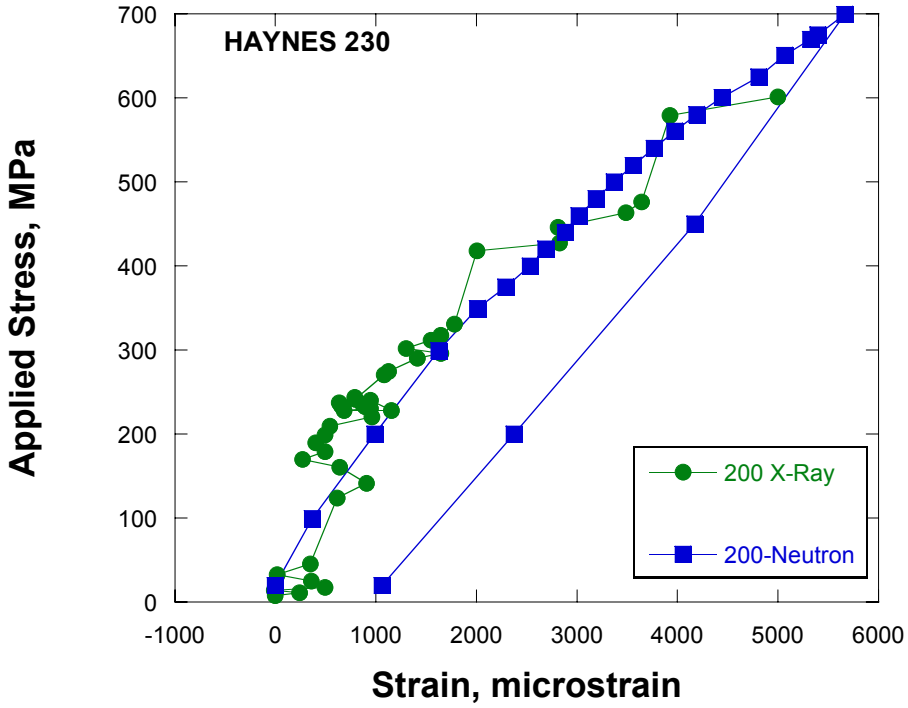

Figure 5.6: Comparison between the 200 strains from the neutron and X-ray *in situ* loading experiments.

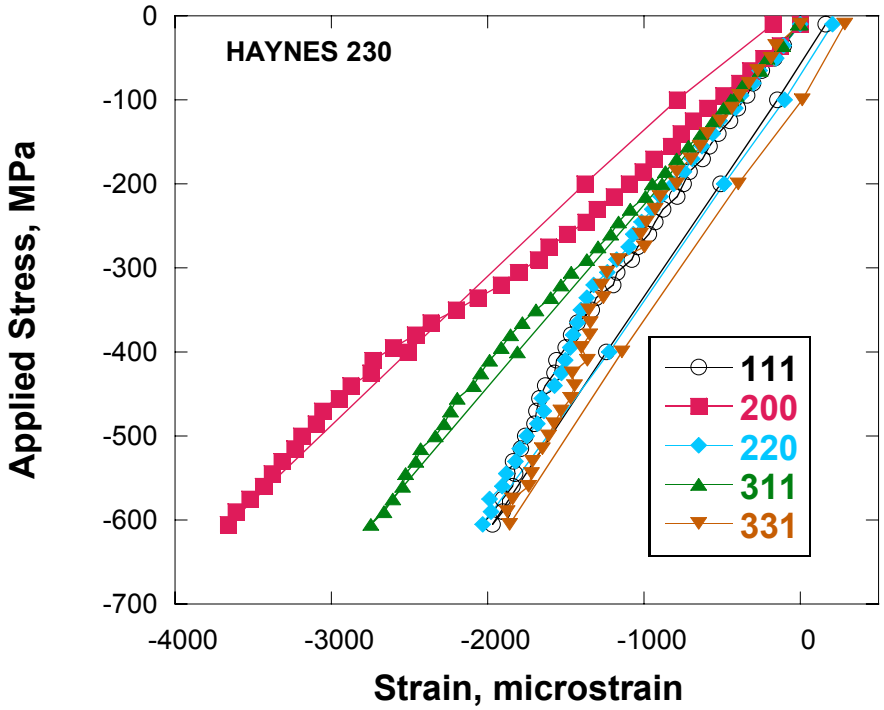

Figure 5.7: Internal strains generated during the *in situ* compression test, axial direction.

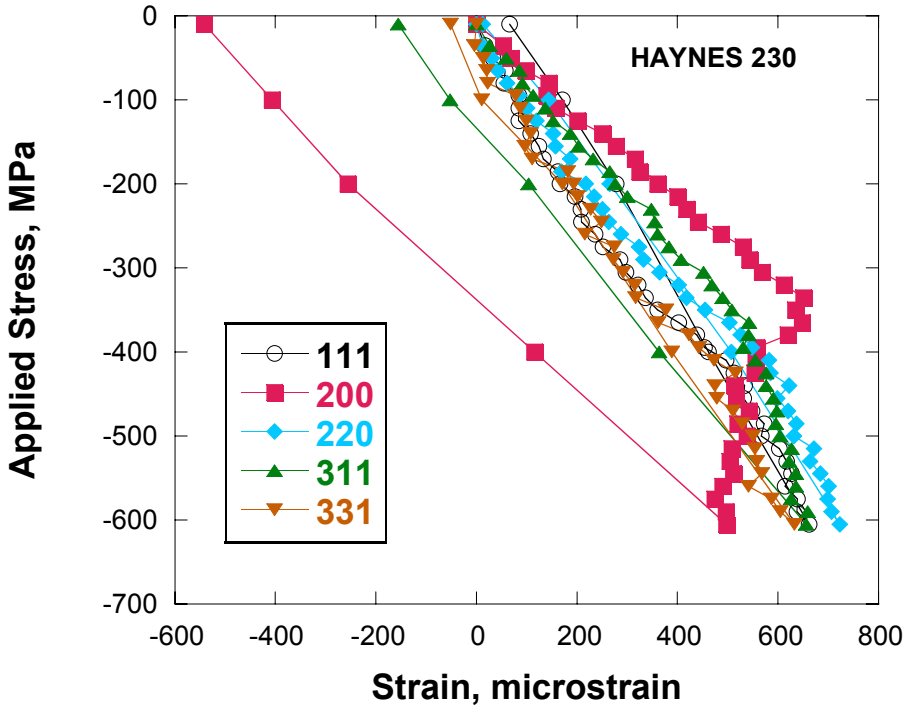

Figure 5.8: Internal strains generated during the *in situ* compression test transverse direction.

Further investigating the behavior in tension and compression, Figure 5.9 compares the lattice parameter strains for compression and tension on the same axis. The qualitative trend of the matrix in compression is completely different than in tension. The compressive behavior suggests that the matrix is shedding load and behaving plastically. In tension, the matrix is picking up load and behaving elastically. This trend suggests a radically different method of accommodating plastic strain in tension than in compression.

The M_6C carbide was found to have a lattice parameter of 11.09 Å. Despite its 1-5% volume fraction, there were multiple M_6C carbide peaks visible in both the transverse and axial diffraction patterns. However, during the *in situ* neutron experiment, only the 333 carbide peak in the transverse bank provided adequate statistics to extract strain data. This strain data is plotted along with the lattice-parameter strains in the 200 reflection in the matrix (Figure 5.10). At the maximum load of 700 MPa, the strain in the 333 carbide peak is approximately -1600 με in the transverse direction, as compared to -1100 με in the 200 peak of the matrix. This 200 reflection exhibits much more strain than any other matrix reflection.

In the axial direction in tension, the X-ray experiment provided carbide data is plotted with the lattice parameter matrix strain in Figure 5.11. Here, a similar behavior in the lattice and the carbide is observed, with the carbide initially taking elastic strain upon the macroscopic yield at 390 MPa, then, at around 420 MPa, the carbide data breaks upward, while the matrix starts carrying elastic strain. The macroscopic yield also coincides with an inflection in the

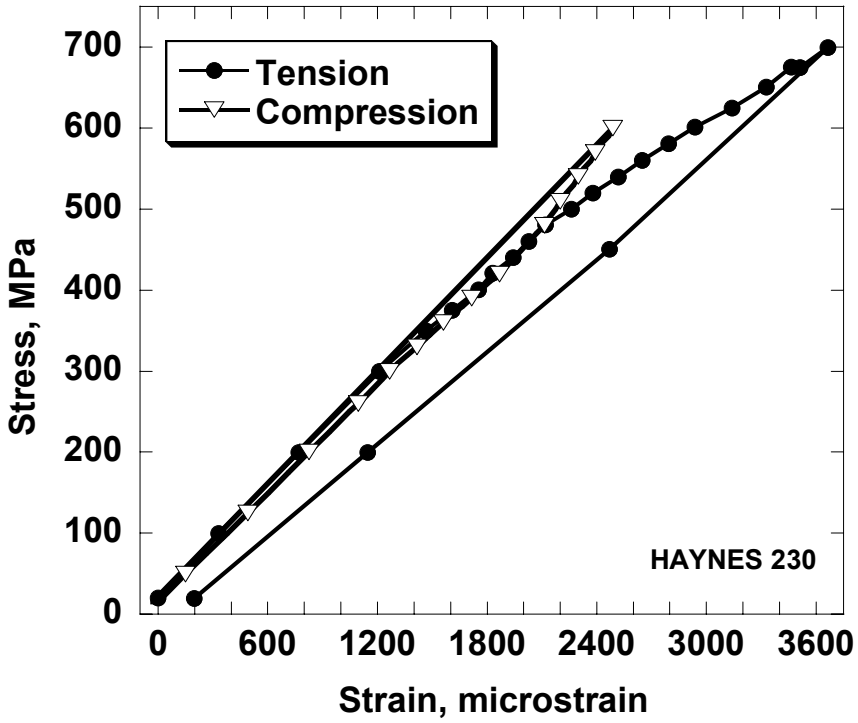

Figure 5.9: Tension-compression asymmetry in the elastic lattice parameter strains in the axial direction.

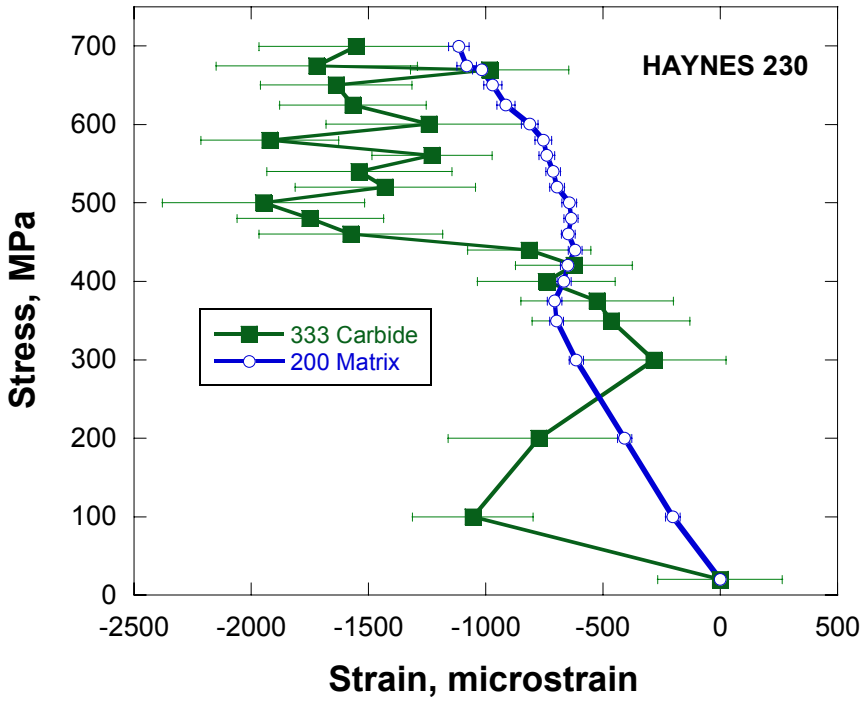

Figure 5.10: The 200 matrix strains and the 333 carbide strains in the transverse direction during the *in situ* tension experiment.

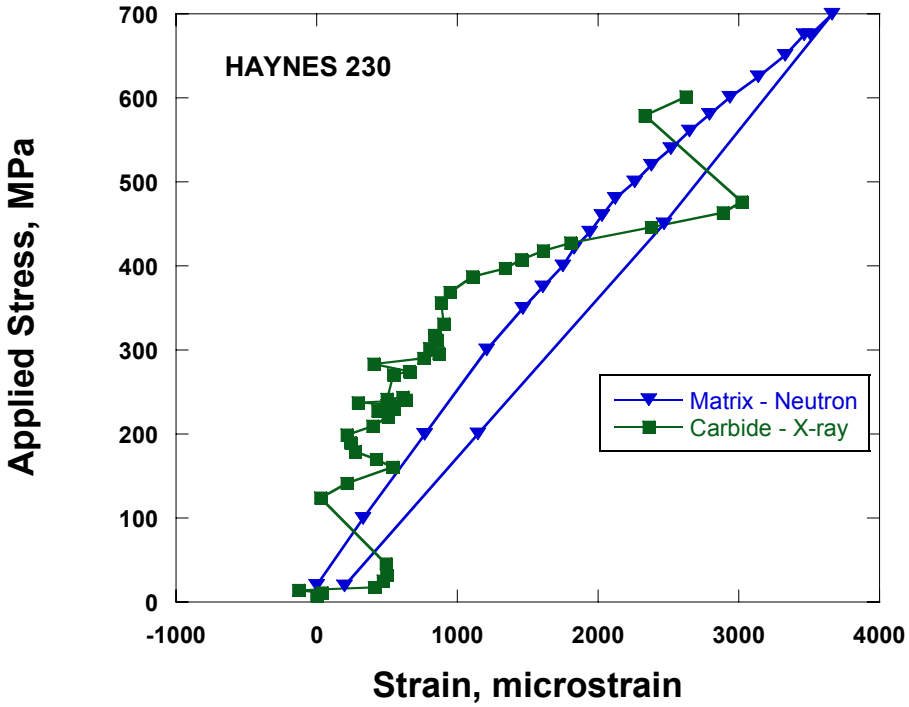

Figure 5.11: The lattice parameter matrix strains, from the neutron experiment, and the carbide strains, from the X-ray experiment, in the axial direction during the *in situ* tension experiment.

matrix strains. Typical composite behavior would show the matrix behaving plastically at yield with the reinforcement behaving elastically. While this behavior begins to occur at the macroscopic yield strength, the opposite behavior occurs at 420 MPa.

The carbide behavior in compression, however, is quite distinct to that in tension. Figure 5.12 displays the matrix behavior in the transverse direction in compression along with that of the 333 carbide. Here we see that at the macroscopic yield point of 390 MPa, the matrix phase no longer accumulates elastic strain, indicating that it is behaving plastically. At this same stress the carbide begins to accumulate elastic strain, thus, taking the bulk of the load. Unfortunately, there is no corresponding data from the axial direction as the carbide peaks are too faint to use in calculating strain.

5.3 Modeling

Finite element modeling (FEM) was performed using ABAQUS™ software [151]. The carbide particles were modeled as cubes embedded in a matrix (Figure 5.13), with the carbides making up 4% by volume of the structure. The mesh was generated using second order 20 node brick elements with reduced integration points. Carbide volume percentage is based on both microscopy and the diffraction pattern, using the phase fraction analysis in GSAS. This model has previously been successful in capturing the behavior of the elastic lattice-parameter strains in particle-strengthened composites [78]. The matrix properties were estimated from the bulk properties of the alloy, while the carbide's

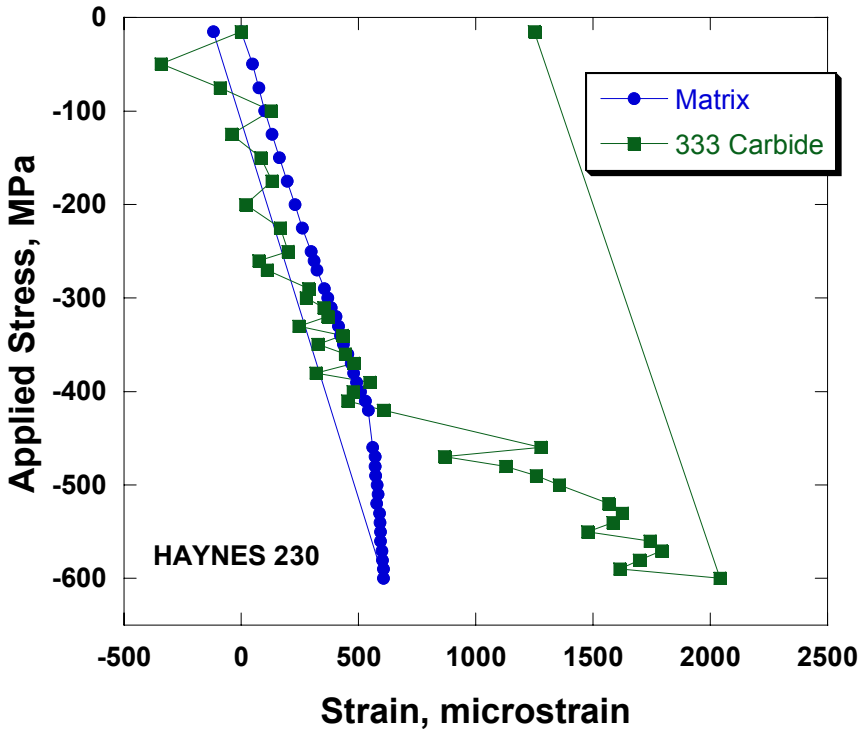

Figure 5.12: The lattice-parameter matrix strains and the 333 carbide strains in the transverse direction during the *in situ* compression experiment.

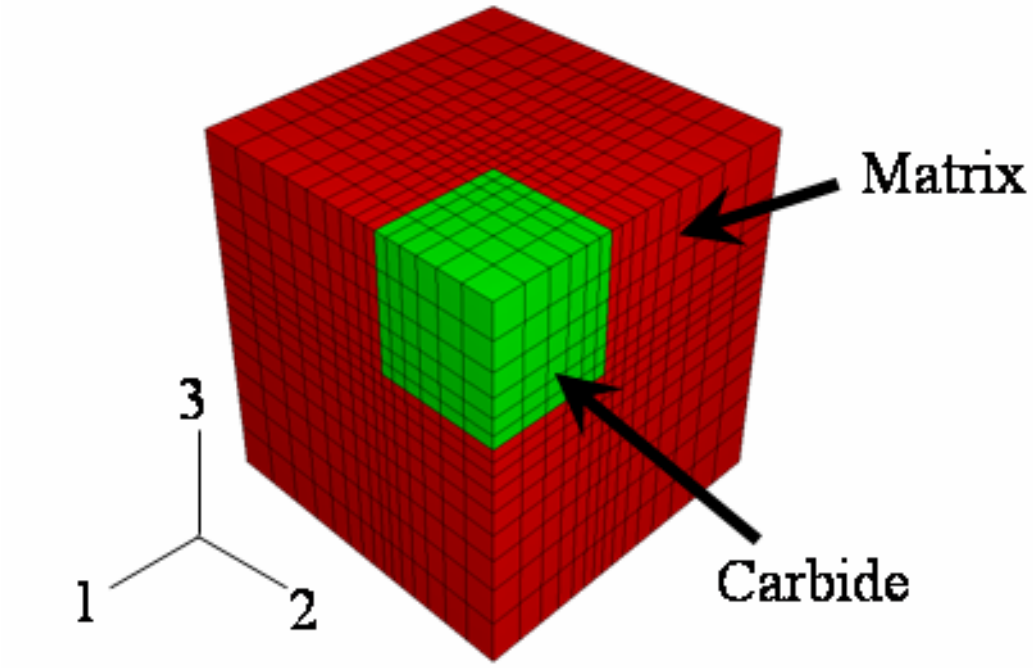

Figure 5.13: A schematic of the representative microstructure used to generate the FEM of the carbide and matrix interaction.

properties were estimated from similar carbides (Table 5.1) [152]. The matrix was modeled with an elastic-hardening bilinear curve, while the carbide was assumed to behave elastically. Each model used the experimental load levels as the applied load. The average of the FEM elastic strains in each element at each load point in the loading axis (3 direction) is analogous to the experimental lattice-parameter strains measured in the axial direction during loading. The average of the FEM strains in both the 1 and 2 directions for each element is analogous to the transverse lattice-parameter strains measured from the *in situ* neutron experiments. Residual strains present in HAYNES 230 in the as-received state were modeled by starting the simulation at a temperature of 600 ºC and cooling it to room temperature before load was applied. This arrangement mimics the thermal residual strains present due to differences in thermal expansion between the carbide and the matrix.

Table 5.1: Materials properties used in the FEM.

	Elastic Modulus (GPa)	Yield Strength (MPa)	σ at $\varepsilon = 47\%$ (MPa)	α (mm/mm/ºC)
Matrix	211	390	840	13×10^{-6}
Carbide	286	-	-	6×10^{-6}

5.4 Discussion

In the compression test, HAYNES 230 exhibits typical composite behavior in the lattice-parameter strains during loading. The behavior is consistent with the 7075 Al experiment shown in Figure 5.2, existing studies [79, 82, 83] and known composite FEM's [78]. As shown in Figure 5.14, little lattice-parameter strain accumulates in the matrix after the macroscopic yield of 390 MPa. Furthermore, the matrix behavior matches that of the FEM model very well. To preserve the force balance, this trend implies that the carbides take up additional stress (elastic strain) in the lattice after macroscopic yield. The strain in the 333 carbide reflection in the transverse direction exhibited this trend, which agreed well with the FEM results. It should be noted that there is a small, but significant difference between the experimental and predicted data in the matrix in the transverse direction. The calculated response of the matrix accumulates less elastic strain in the transverse direction than observed.

At this stage, the model, other than thermal stresses, contains nothing capable of producing tension-compression asymmetry. Thus, the calculated lattice response is necessarily similar in tension and compression. However, as previously illustrated (Figure 5.9), the measured lattice response to applied tension is strongly disparate from the response to compression. While the thermal residual strains will cause a small disparity in the behavior of tension and compression in a typical composite, the difference shown in Figure 5.9 cannot be explained by residual strains alone. As shown in Figure 5.15, in tension, the matrix accumulates elastic strain in the axial direction at an increasing rate

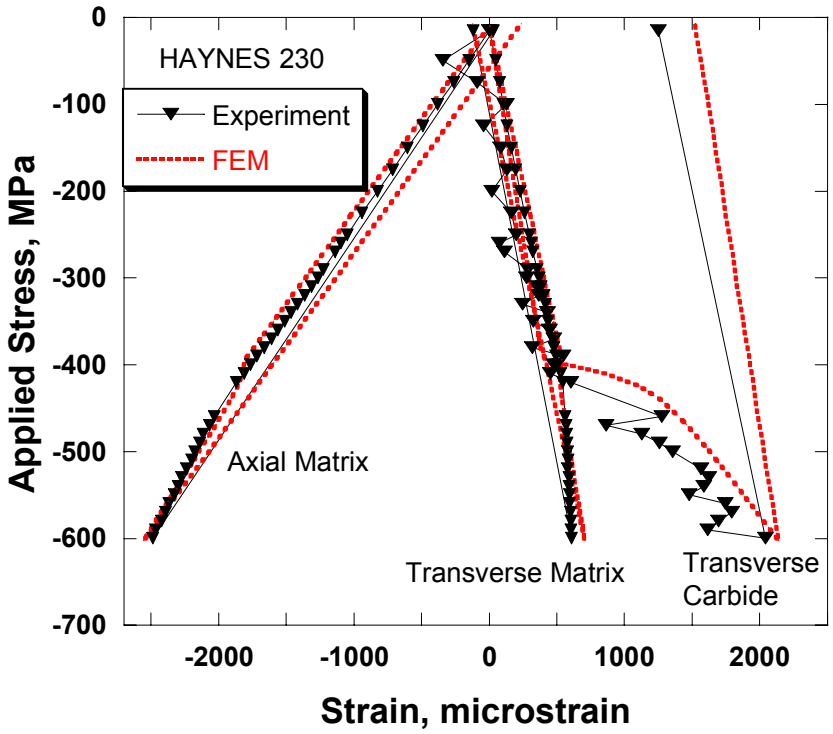

Figure 5.14: Experimental data vs. FEM for the *in situ* compression experiment.

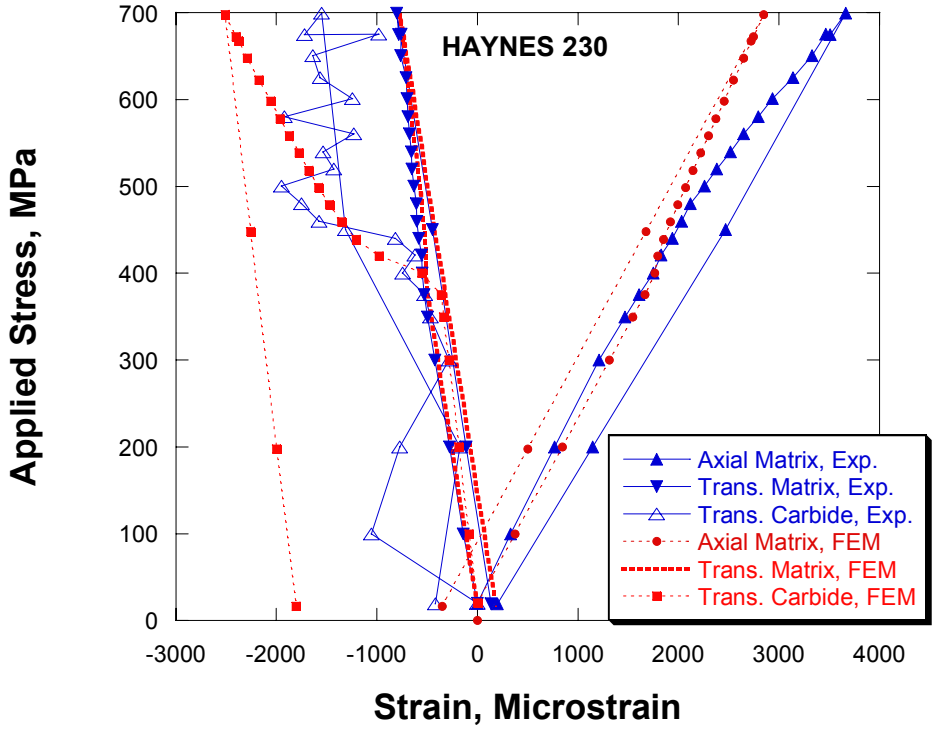

Figure 5.15: Experimental data vs. FEM for the *in situ* tension experiment, neutron data.

following macroscopic yield at 390 MPa, while the model predicts (and the behavior in compression shows) that little elastic strain should evolve in the matrix after yield. In contrast, the transverse response of the matrix was very well captured by the model. Again the 333 carbide peak in the transverse direction is the only experimental carbide data available from the *in situ* neutron test, but the statistics of this data are quite poor (~500 με error bars). The general trend in the experimental carbide data agrees with the FEM prediction.

In the axial direction in tension, however, we can add the carbide data from the *in situ* X-ray experiment, Figure 5.16. The experimental carbide data follows the predicted curve through the macroscopic yield of 390 MPa to approximately 420 MPa. Here the carbide behavior deflects from the predicted path and no longer accumulates elastic strain. Similarly, the experimental data for the matrix deviates from the predicted path at 420 MPa as well. The matrix clearly begins to accumulate elastic strain where the model predicts that it would shed strain.

The tension-compression asymmetry is consistent with carbide debonding and cracking in tension, which effectively prevents the expected load sharing between the carbide and the matrix in the axial direction. Perpendicular to the applied tensile load, Poisson's compression occurs, thus, no debonding or carbide cracking takes place and the load transfer is as expected, Figure 5.17. The tensile behavior discussed here is consistent with previous *in situ* neutron results showing debonding in continuous fiber reinforced composites when loaded perpendicularly to the fiber direction [83]. Similarly, in compression, neither debonding nor

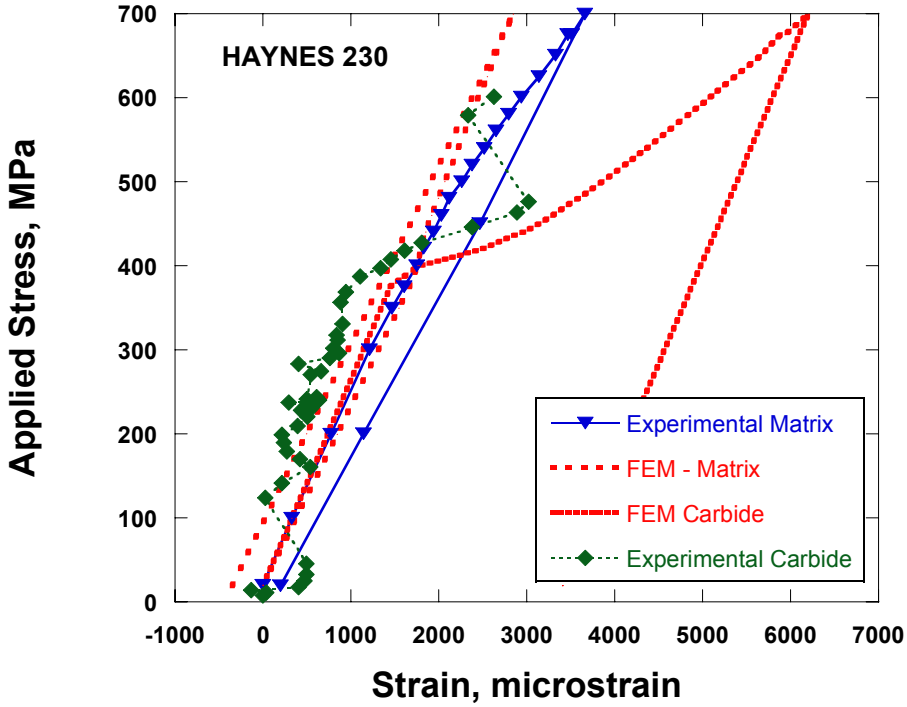

Figure 5.16: Experimental data vs. FEM for the *in situ* tension experiment in the axial direction with both neutron and X-ray data.

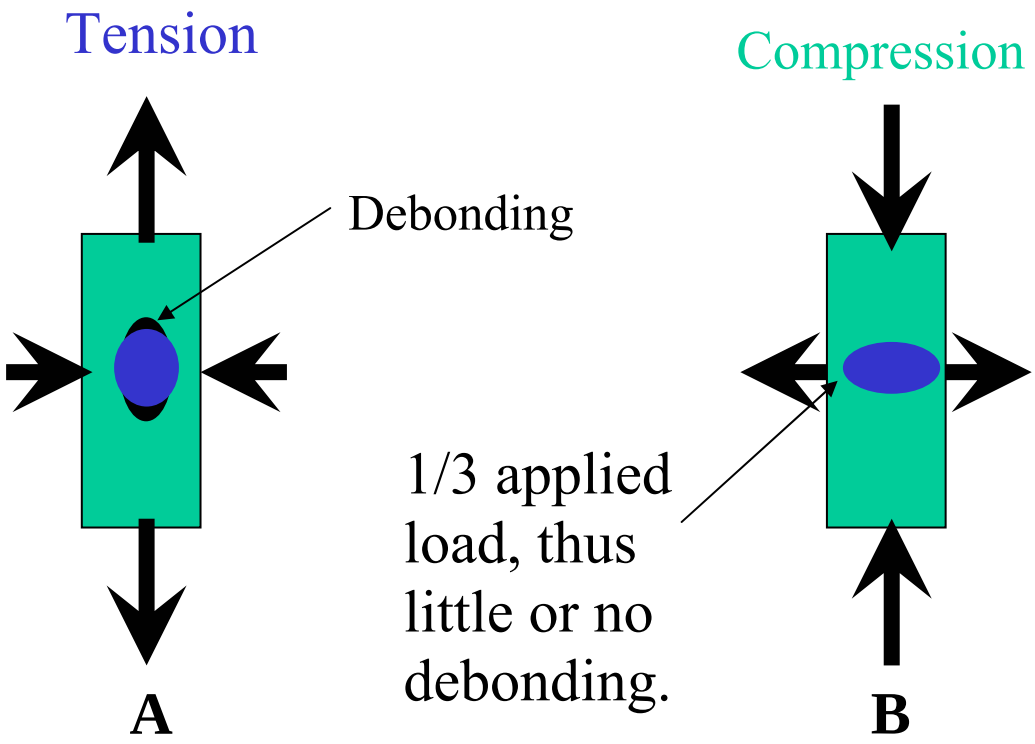

Figure 5.17: Proposed debonding mechanism in tension and compression.

cracking occurs parallel to the applied load. However, perpendicular to the applied compressive load, Poisson's tension occurs, which may be too weak to lead to debonding, or may only cause small amounts of debonding. Weak debonding may be responsible for the subtle differences between the experimental and predicted behavior of the matrix in the transverse direction during the compression test (Figure 5.14).

Careful investigation of the inflections in the *in situ* lattice parameter strains in the matrix and the carbides, along with a comparison to the FEM, reveals information about when debonding or cracking may occur. Most clearly shown in Figure 5.18, both the carbide and the matrix deviate from elasticity as expected at the macroscopic yield strength of 390 MPa. From this point forward the carbide strains follow the path predicted by the FEM until around 420 MPa. Similarly, it is here that the matrix phase changes from shedding elastic strain to accumulating it. Thus, it is possible to conjecture that the carbides debond from the matrix at 420 MPa.

Indeed, the carbide cracking and debonding is confirmed by microscopy of a cross section taken parallel to the loading direction in a sample loaded to 700 MPa, Figure 5.19. Here both debonding around carbides and some carbide cracking is present. Contrast this with the micrograph taken perpendicular to the loading direction of the sample, Figure 5.20, no carbide cracking is visible, and minor debonding is visible. This debonding is likely due to carbides being sectioned above or below their centerline, thus is not due to debonding in the direction perpendicular to the load.

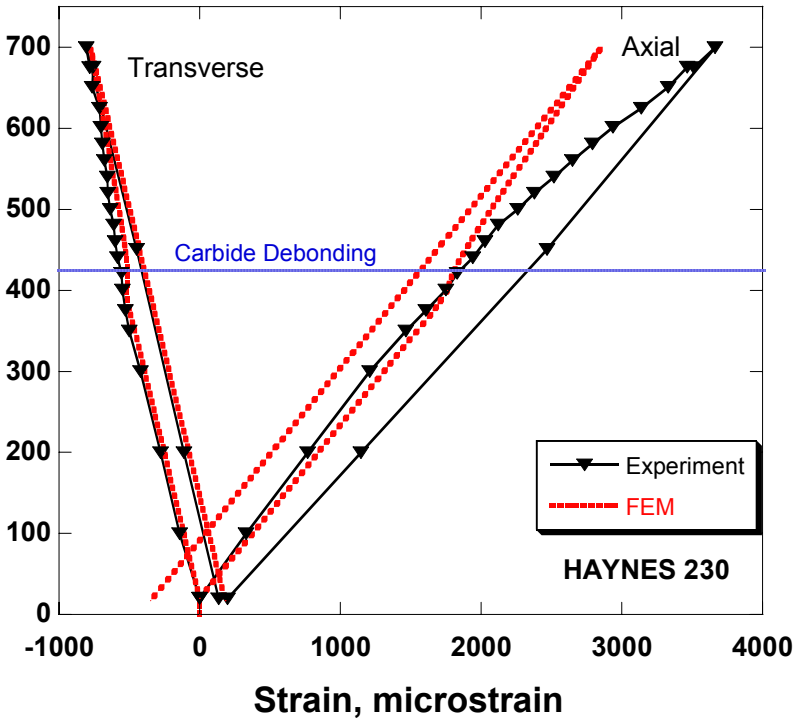

Figure 5.18: Experimental lattice strains in tension vs FEM model with macroscopic yield strength and proposed carbide debonding stress marked.

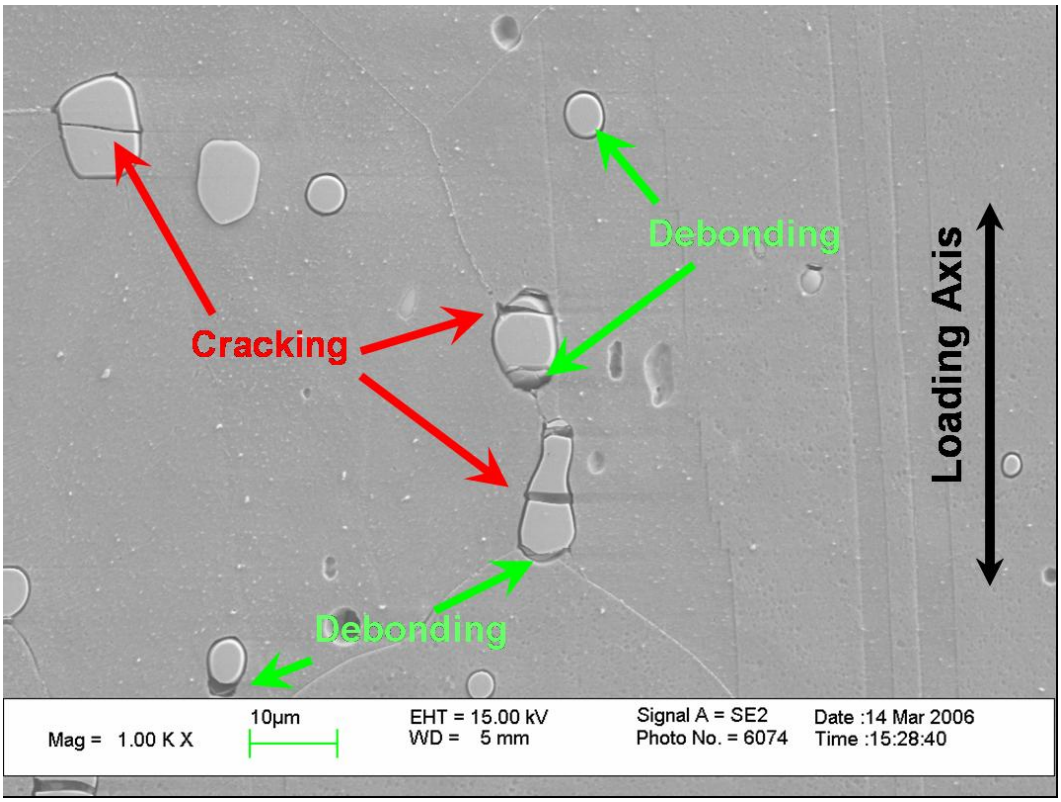

Figure 5.19: Micrograph of HAYNES 230 perpendicular to the applied load of 700 MPa, displaying carbide debonding and cracking.

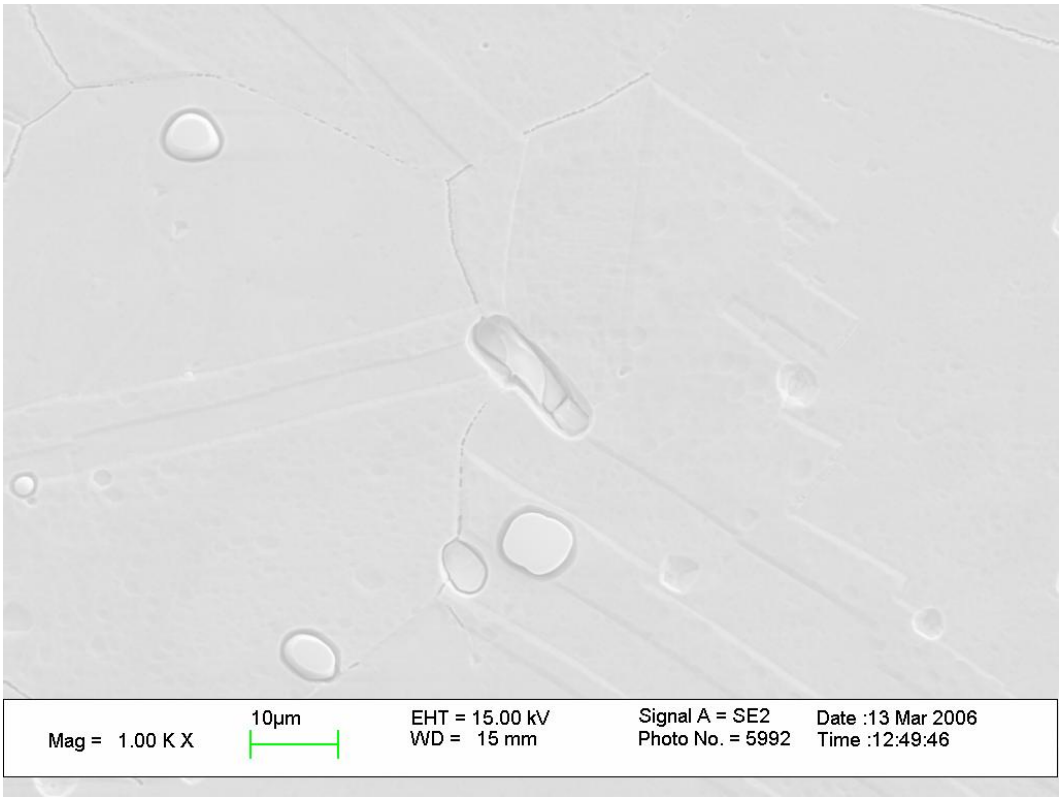

Figure 5.20: Micrograph of HAYNES 230 parallel to the applied load of 700 MPa, displaying carbide some debonding, but no cracking.

5.5 Conclusions

In contrast to the clear composite loading behavior of 7075 Aluminum and the single phase anisotropic behavior of HASTELLOY C-2000, the loading behavior of HAYNES 230 is unusual in tension and composite-like in compression. Modeling the expected behavior of HAYNES 230 also confirms that the tensile behavior is unusual. Carbide debonding and cracking in tension, but not in compression, explains this tension-compression asymmetry. *In situ* X-ray diffraction explicitly shows the carbide accepting and then shedding load as debonding occurs, while microscopy confirms that debonding and cracking have occurred. These mechanisms appear to occur at 420 MPa, just past the macroscopic yield of 390 MPa.

Chapter 6
In Situ Fatigue Experiments

6.1 Introduction

As shown in Chapters 3 and 4, neutron diffraction provides a nondestructive technique to evaluate the intergranular strain development due to mechanical loading in a material. Coupling neutron diffraction with a hydraulic testing machine, as at the Spectrometer for Materials Research at Temperature and Stress (SMARTS) at the Los Alamos Neutron Science Center (LANSCE), allows monitoring of internal strains during uniaxial or cyclic loading. Since the mechanisms of damage in fatigue are not completely understood, it is natural to use the *in situ* loading capabilities of an instrument like SMARTS and ENGIN-X to explore the changes in internal strains during cyclic loading.

6.2 Tension-Tension Experiment

Cylindrical test specimens were cut from 13 mm thick plate, with a gauge-length of 50 mm and a diameter of 6 mm. The specimens had a surface roughness of 0.2 μm along the gauge-length section. The ends of the specimens were threaded with a ½" UNC 13 thread [7].

The *in situ* loading measurement, to 700 MPa in tension, described in Chapter 5, serves as a single cycle fatigue test and was the baseline for comparison. Figure 5.1 displays the macroscopic loading for this experiment. The

first fatigue experiment was a complete fatigue test at an R ratio of 0.1 ($\sigma_{min}/\sigma_{max}$, where σ_{min} and σ_{max} are the minimum and maximum applied stresses, respectively) and a σ_{max} of 700 MPa. Testing was paused approximately every half order of magnitude to take a diffraction pattern at σ_{min} and σ_{max}. Cycling occurred at a frequency of 10 Hz between diffraction patterns. Diffraction patterns were taken for 45 minutes, instead of the 15-minute patterns taken during the loading experiment. Despite the longer count time, the carbide peaks were too indistinct to yield strain data. This test was designed to go to failure. Unfortunately, the grips failed at 45,000 cycles, invalidating the subsequent diffraction measurements, due to the loss of the critical sample positioning. The grips were replaced and the fatigue test continued. The sample failed at 50,613 cycles. The last measurement prior to the failed grips occurred at 42,417 cycles, which corresponds to 84% of the fatigue life of this sample.

The second fatigue experiment was a 110 cycle fatigue test under the same conditions as the first: an R ratio of 0.1 and a σ_{max} of 700 MPa. Diffraction patterns were taken at 20 MPa before the test began and after the 110 cycles were completed. During the experiment, a diffraction pattern was taken at σ_{max} for each cycle, for a total of 110 total measurements. This experiment was designed to focus on the residual strain development during the initial stages of fatigue.

6.3 Results for the Tension-Tension Experiment

Figures 6.1 and 6.2 display the axial and transverse internal strains in the matrix in the 111, 200 and 311 directions versus cycle during the complete fatigue

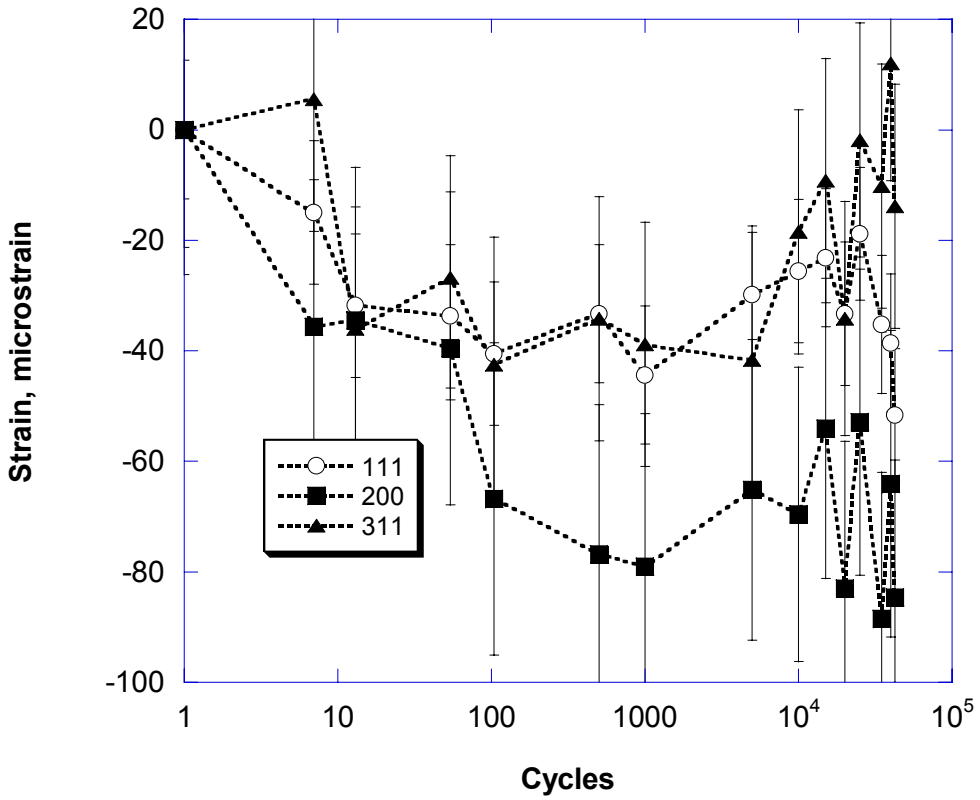

Figure 6.1: The *hkl* strains versus cycle at 700 MPa in the axial direction for the complete fatigue test.

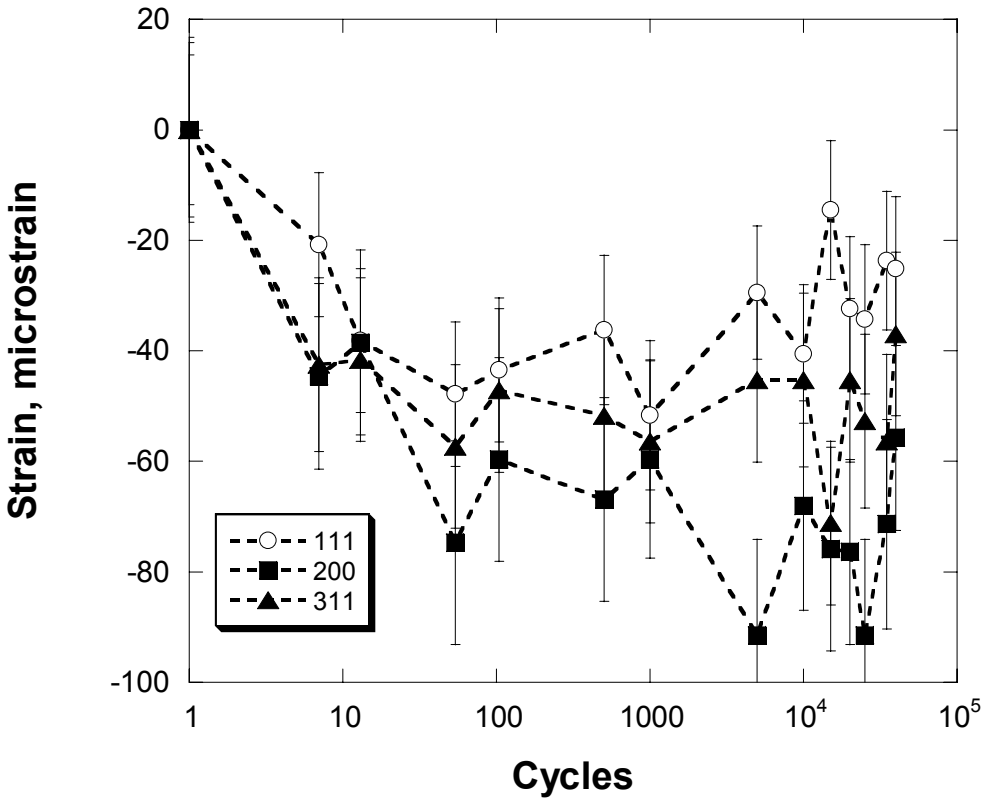

Figure 6.2: The *hkl* strains versus cycle at 700 MPa in the transverse direction for the complete fatigue test.

test. The strains plotted are at an applied load of 700 MPa. For clarity, the initial strains for each reflection are offset to zero. Similarly, Figures 6.3 and 6.4 show the development of axial and transverse internal strains in the same three reflections at an applied load of 70 MPa.

Figure 6.5 shows the stress versus internal strain data in the axial direction for the second test, 110 cycles of fatigue. The data is not a fully formed curve as patterns were taken only before the test began, at the peak load for each cycle, and then, after the last cycle was completed. The flat section at the top of each curve represents the scatter in the data taken at the peak load. The strain measurements at the peak load and the endpoints of the experiment are consistent with those of the *in situ* loading test, as shown in Figure 6.6. This comparison is made in Table 6.1. Table 6.2 presents the same comparison for the transverse direction.

6.4 Discussion of the Tension-Tension Experiment

Figure 6.1 displays the internal strains in various *hkl* directions versus cycle for the axial direction at 700 MPa during the complete fatigue test. There is a clear relaxation in the internal strains as the initial stages of fatigue progress. The magnitudes of the strains are fairly small, less than 100 με, but they are significant when compared to the ~20 με error bars. Strains relax over the first 1,000 cycles, but then remain constant for the remainder of the test. The data scatter increases at larger number of cycles. The strain in the 311 reflection returns to its original value as the test approaches 85% of the fatigue life. It is

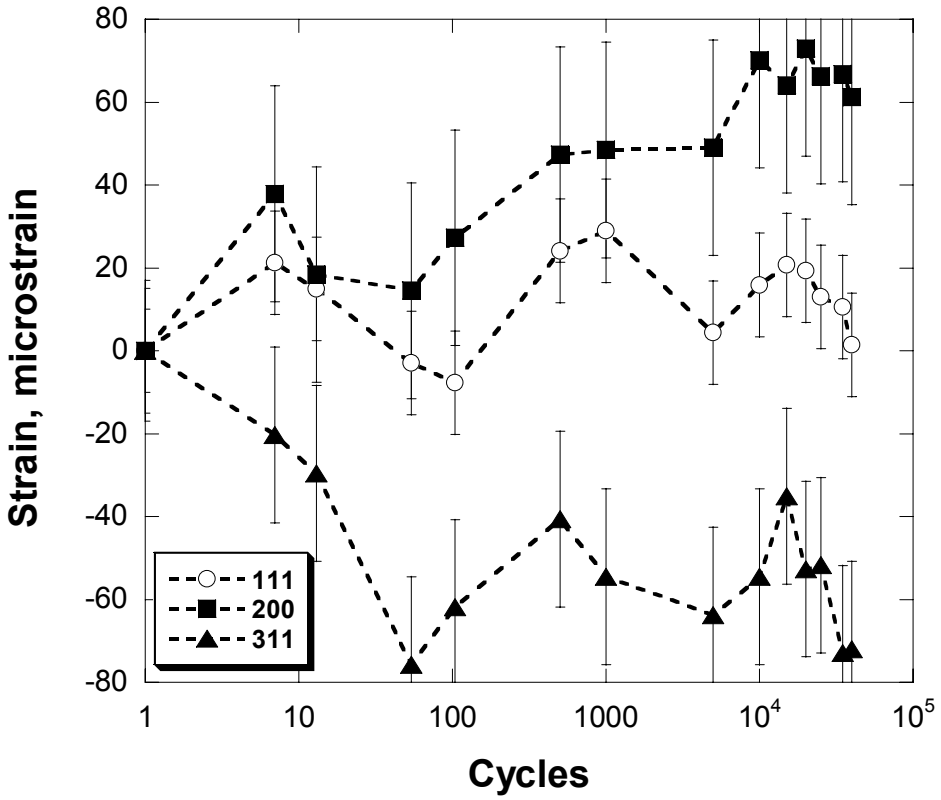

Figure 6.3: The *hkl* strains versus cycle at 70 MPa in the axial direction for the complete fatigue test.

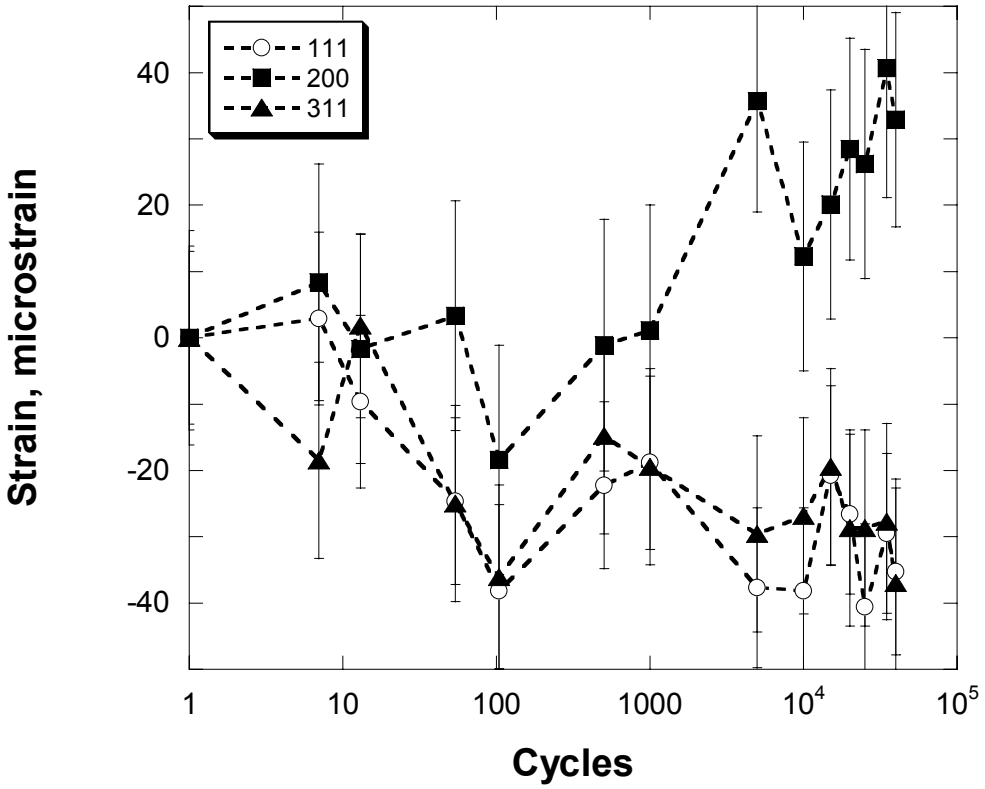

Figure 6.4: The *hkl* strains versus cycle at 70 MPa in the transverse direction for the complete fatigue test.

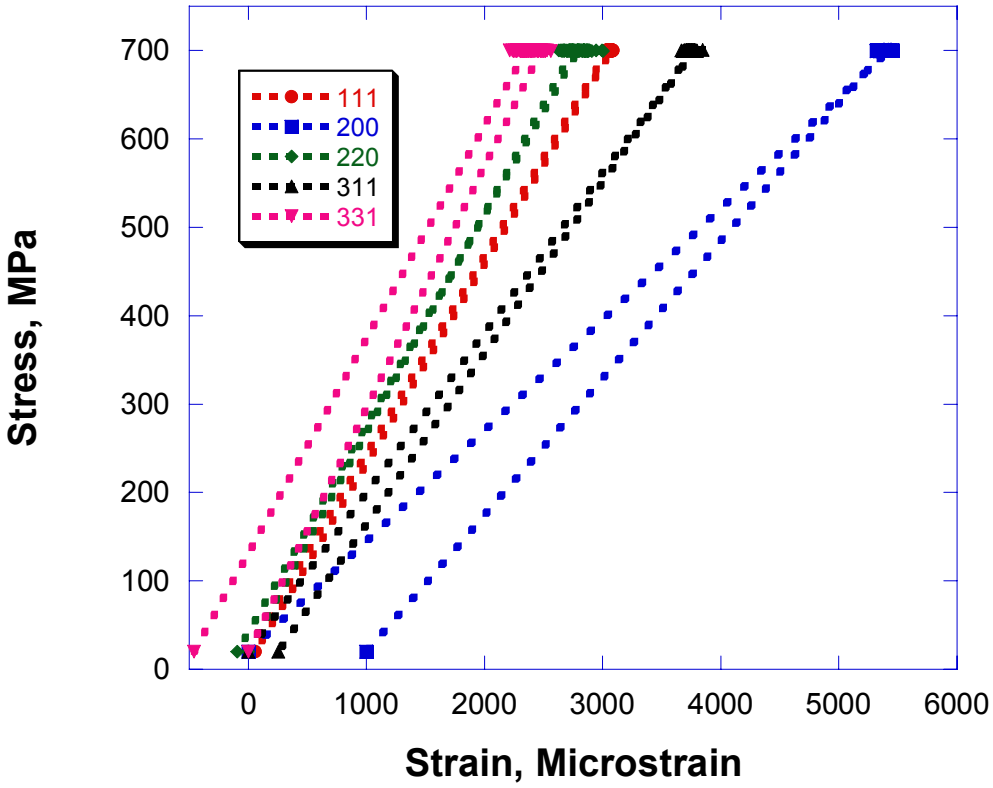

Figure 6.5: The *hkl* strains in the axial direction during the 110 cycle fatigue test.

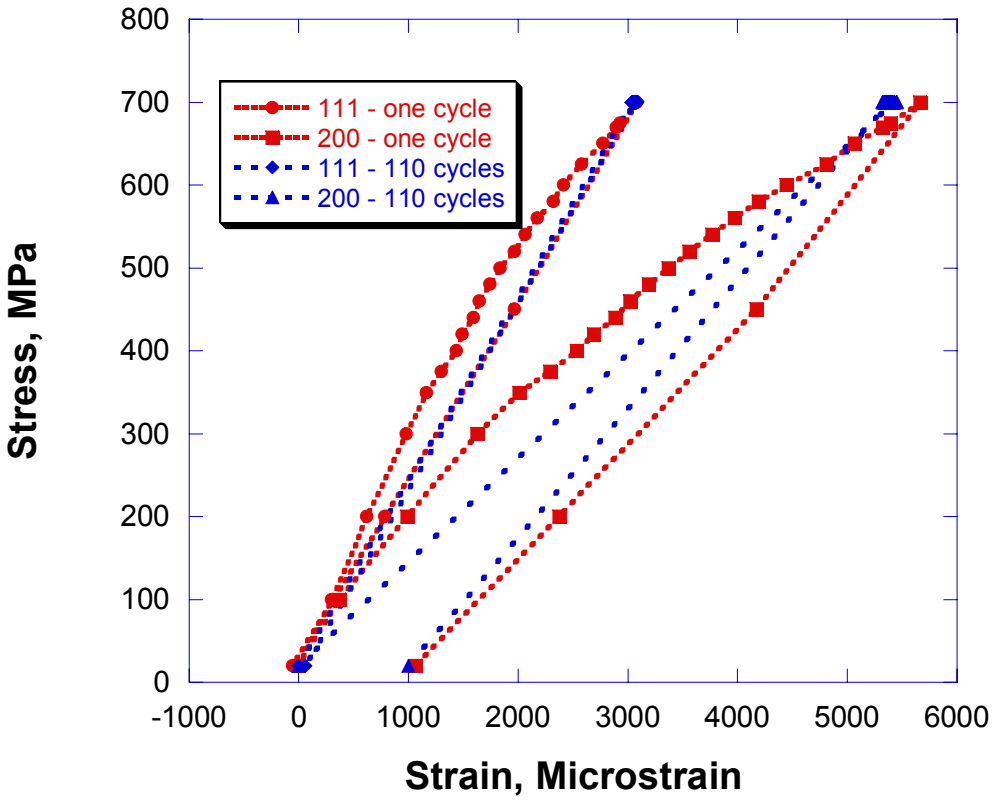

Figure 6.6: Comparison between 1 cycle of fatigue and 110 cycles of fatigue in the 111 and 200 axial directions.

Table 6.1: The *hkl* strains at 700 MPa and upon unloading in the axial direction for the single cycle and the 110 cycle test.

Reflection	"Single Cycle" experiment		110 cycle experiment	
	με at 700MPa	με after unloading	avg. με at 700MPa	με after unloading
111	3076 ± 32	-58 ± 32	3062 ± 37	59 ± 38
200	5663 ± 53	1063 ± 50	5384 ± 60	998 ± 55
220	3114 ± 114	135 ± 112	2786 ± 107	-92 ± 109
311	3934 ± 52	285 ± 51	3743 ± 58	252 ± 55
331	2764 ± 122	-344 ± 122	2383 ± 129	-459 ± 123

Table 6.2: The *hkl* strains at 700 MPa and upon unloading in the transverse direction for the single cycle and the 110 cycle test.

Reflection	Single cycle experiment		110 cycle experiment	
	με at 700MPa	με after unloading	avg. με at 700MPa	με after unloading
111	-709 ± 40	25 ± 42	-560 ± 32	80 ± 33
200	-1114 ± 43	258 ± 42	-1198 ± 33	180 ± 35
220	-874 ± 27	92 ± 28	-737 ± 36	103 ± 34
311	-788 ± 32	216± 32	-711 ± 34	215 ± 34
331	-695 ± 71	135 ± 71	-501 ± 68	250 ± 67

unclear whether this is significant in the context of the scatter seen in the other peaks. Figure 6.2 shows the development of internal strains with increasing cycles at 700 MPa in the transverse direction. The trends in the transverse direction are similar to the axial direction with relaxation of internal strains as fatigue progresses.

Figure 6.3 shows the internal strains in the axial direction at a load of 70 MPa as a function of number of fatigue cycles. In this case the 111 reflection remains roughly constant, while the strain in the 200 direction increases and the strain in the 311 direction decreases. Figure 6.4, showing the behavior of the same three reflections in the transverse direction, displays similar trends; however the strains in both the 111 and 311 directions decrease. Since there were no measurements taken after 85% of the fatigue life, no generalizations can be made about the behavior of the internal strains as failure is approached.

The trends seen in Figures 6.1 through 6.4 are consistent with slight cyclic hardening or softening in individual crystallographic directions as fatigue progresses. It is likely that any larger responses in the internal strains to fatigue are masked by the large plastic strain achieved in the first cycle. Future experiments should explore the internal response to tension-tension fatigue at lower stress ranges.

Interestingly the trends displayed during the experiment suggest that the elastic modulus is increasing slightly in each crystallographic direction as fatigue progresses. The effect is subtle and is based on only the end points, however, this effect has been seen before in stainless steel [99]. No convincing reasoning is

offered for this effect at this time; the effect is subtle and does not have a large statistical basis. However, a possible cause is the effect of continuing damage as fatigue progresses, particularly cracking and microvoid formation. This would effectively change the surrounds and constraints that each crystal interacts with. If we were to apply an EPSC type model to this, the effect would be that the HEM would be changing and weakening as fatigue progresses. This change may result in an increase in elastic modulus in various crystallographic directions. Again, carefully exploring this effect, perhaps at lower stress ranges where the changes in *hkl* strains will be greater, will allow for a better understanding and a basis for comparison for future modeling efforts. This is beyond current modeling capabilities, but efforts are underway to improve the EPSC models to include two phase materials and changes in the properties of the HEM as the model progresses.

The results summarized in Table 1 show, in every direction except the 220, a steeper unloading curve from the 110 cycle experiment than in the loading experiment. This suggests that the modulus change is visible in the early stages of fatigue. Again, the error bars on the measurements are significant compared to the change in modulus, but this issue merits further exploration. Figure 6.7 compares the internal strains versus fatigue cycle in the 200 axial direction for both the 110 cycle and the complete fatigue test. For clarity, the beginning strain, at 1 cycle, is offset to the same point for both experiments. In the complete fatigue test, a clear relaxation of 70 με is revealed over the first 100 cycles. The scatter in the 110 cycle test masks any clear trends. However it is clear that the data in the 110 cycle

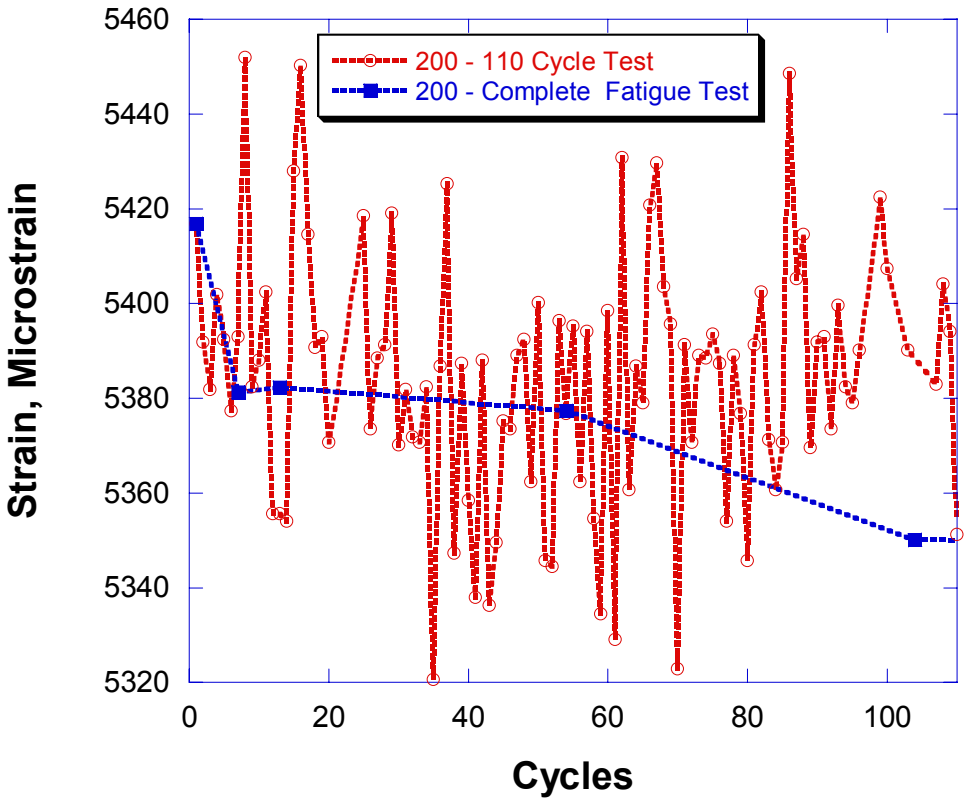

Figure 6.7: Strain versus cycle for 110 cycle and complete test in the 200 axial direction.

test is consistent with that taken over the complete fatigue test despite much higher scatter.

6.5 Tension-Compression Experiment

A complementary tension compression experiment took place at the ENGIN-X diffractometer at the ISIS accelerator. Cylindrical test specimens were used, cut from 13 mm thick plate, with a gauge-length of 50 mm and a diameter of 6 mm. A reduced section of 5 mm diameter and 12 mm in length was cut into the samples to avoid buckling by achieving a 2.5:1 gauge length to diameter ratio. The specimens had a surface roughness of 0.2 μm along the gauge length. The fatigue experiment was a performed under strain controlled conditions at an R ratio of -1 ($\varepsilon_{min}/\varepsilon_{max}$, where ε_{min} and ε_{max} are the minimum and maximum applied strains, respectively) and a ε_{max} of 0.75%. As shown in Figure 6.8, testing was paused periodically to take a diffraction pattern at four points along the cyclic stress-strain curve: the maximum applied strain, zero stress (tensile residual strain), maximum compressive strain, and zero stress (compressive residual strain). All measured strains are taken with respect to the initial position of zero strain. Cycling occurred at a frequency of 0.5 Hz between diffraction patterns. Diffraction patterns were taken for 12 minutes. The test was expected to run approximately 10,000 cycles; however alignment issues caused the sample to buckle during the course of the experiment. The buckling occurred outside the diffraction volume and the strain gauge. This caused the sample to fail prematurely outside the gauge volume, but the desired fatigue conditions were

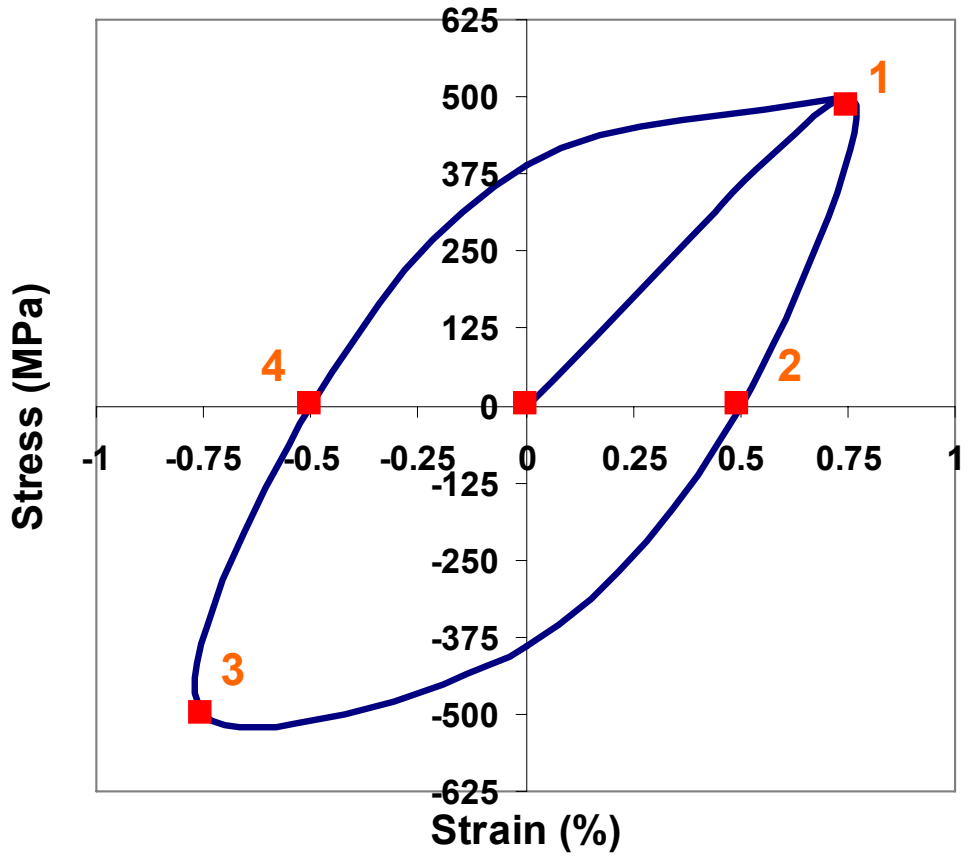

Figure 6.8: Schematic of the cyclic stress-strain curve during the tension-compression fatigue experiment.

achieved in the area being measured. The diffraction patterns were similar to those of taken on SMARTS (Figure 3.1). Again, the only carbide peak resolvable was the 333 reflection in the transverse detectors.

6.6 Results and Discussion of the Tension-Compression Fatigue Experiment

Figure 6.9 displays the *hkl* specific strains vs fatigue cycles at the maximum tensile strain for 5 crystallographic directions. The qualitative trends of accumulation of elastic strain are very similar to that shown in both the *in situ* loading experiment and the 110 cycle tension-tension fatigue test, Figures 6.4 and 6.5, respectively. The 200 direction accumulates the most elastic strain, the 311 direction, the next most, with the 111, 220 and 331 directions accumulating similarly small amounts of strain. However, the total amount of strain accumulated in each direction over the course of the first 100 cycles is much greater than seen in the tension-tension fatigue experiment. While the total change in elastic strain during the tension-tension experiments was less than 100 με in all directions, the tension-compression experiment shows changes in elastic strains ranging from 500 με in the 331 direction to 1500 με in the 200 direction. After the initial accumulation over the first 100 cycles, the strains appear to relax slightly over the remainder of the experiment. As mentioned, the total cycles explored were only 15% of the fatigue life, so no generalizations can be made about the behavior of internal strains at longer fatigue life.

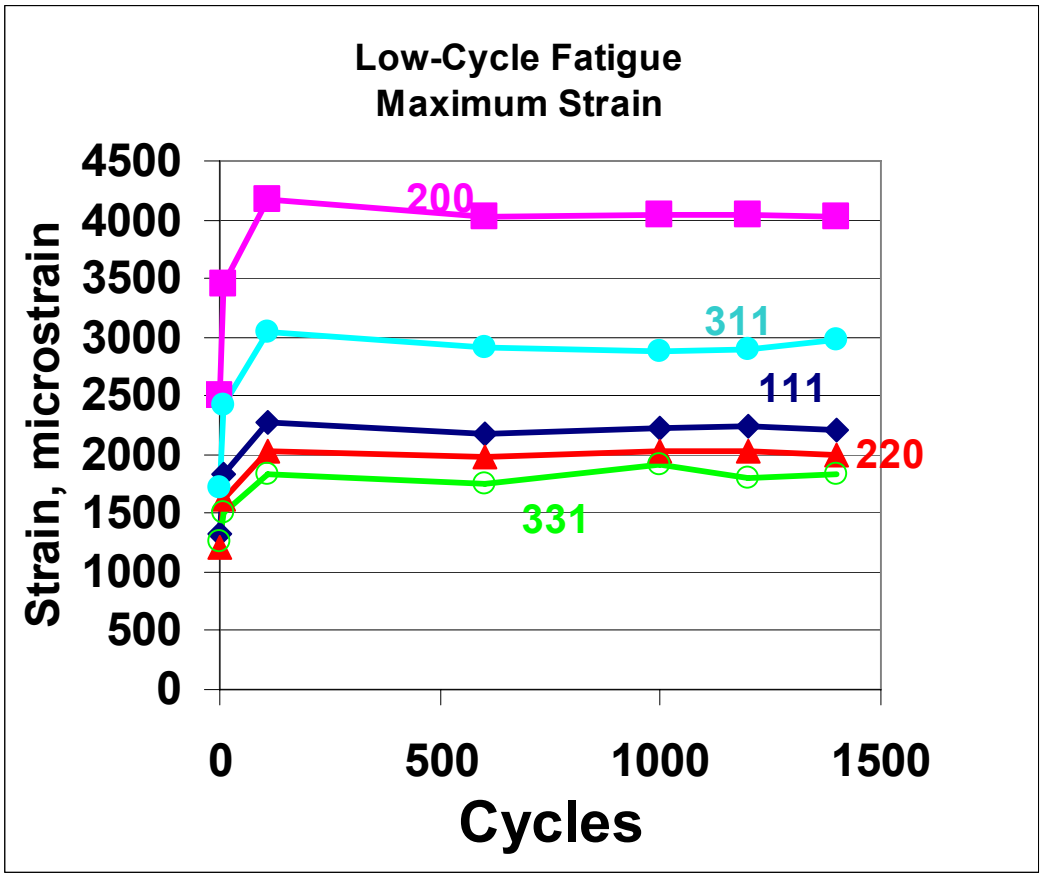

Figure 6.9: The *hkl* strains versus cycles of fatigue at the maximum tensile strain, axial direction.

Exploring the 200 direction more carefully, shown in Figure 6.10, the behavior around the cyclic stress strain curve can be determined. The qualitative behavior is similar for each reflection, but the magnitudes are less per the elastic anisotropy seen in the loading experiment and Figure 6.9. The trends in elastic strain are consistent with the applied strain and the position on the cyclic stress-strain curve. The largest strains are found at the maximum and minimum applied strain. The tensile and compressive residual strains are much smaller in magnitude and, as expected, consistent with elastic unloading from the maximum applied strains. The tensile and compressive elastic strains measured are not exactly symmetric, shown in Figure 6.11. This suggests that the tension-compression anisotropy described in Chapter 5 affects the residual strains in this experiment. The maximum applied strain is not much more than that at which debonding occurs, so the differences in tension and compression are not large.

In the transverse direction, Figure 6.12, the behavior is consistent with that seen in the *in situ* loading experiment shown in Figure 5.5. Additionally, the carbide data shows the same effect seen in the loading experiment, with the carbide taking far more strain in the transverse direction than the matrix. Unfortunately there is no axial carbide data as the peak was not resolvable in the axial diffraction pattern. The strain accumulation in the carbide looks to be consistent with that of the other crystallographic directions; however there is more scatter in the data after the first 100 cycles. This is caused by the poor statistics of the smaller peak, leading to error bars in excess of 200 με, compared to the 20 με error bars in the matrix reflections.

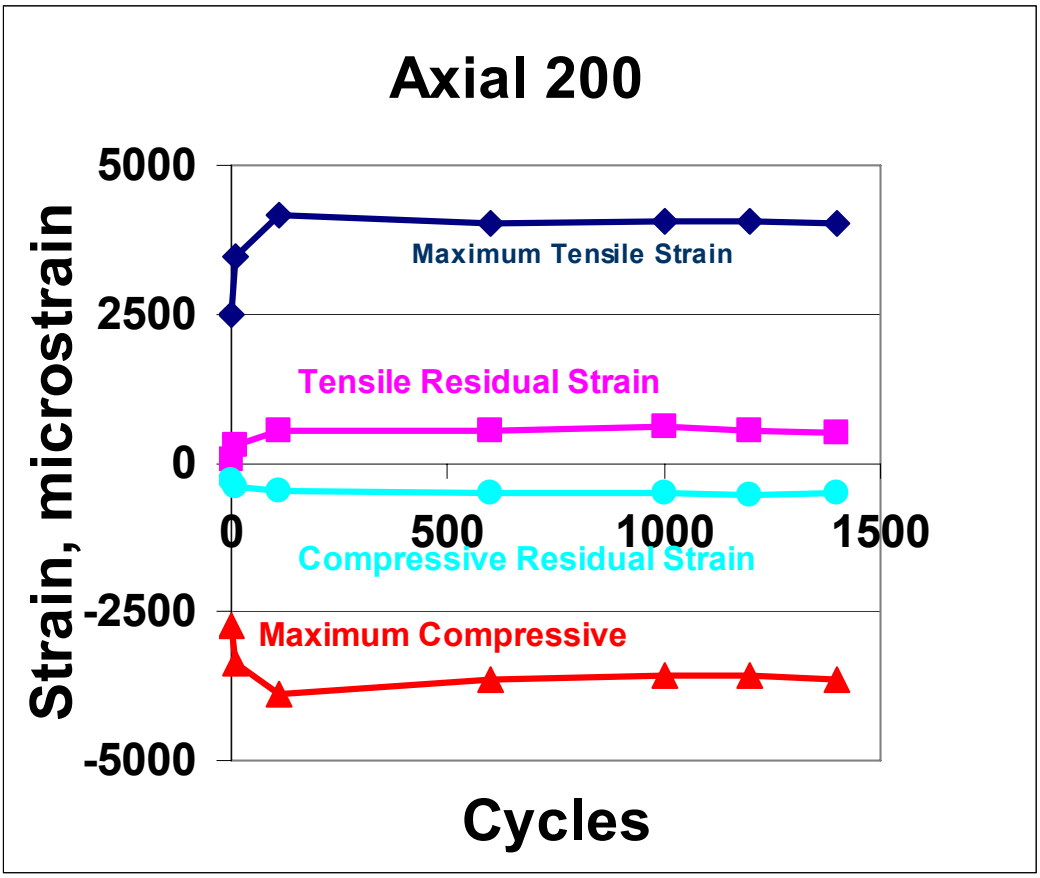

Figure 6.10: Strain accumulation in the 200 reflection, axial direction, at different points along the cyclic stress-strain curve.

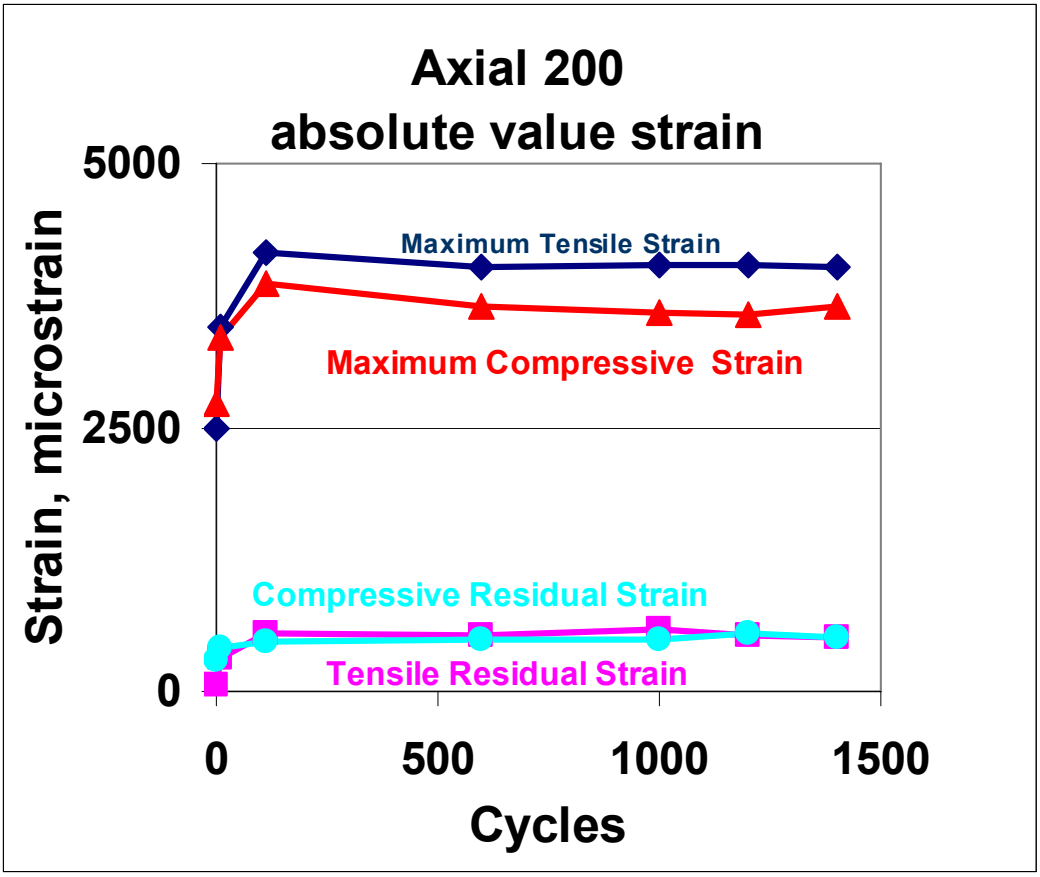

Figure 6.11: Absolute value of the strain accumulation in the 200 reflection, axial direction, at different points along the cyclic stress-strain curve.

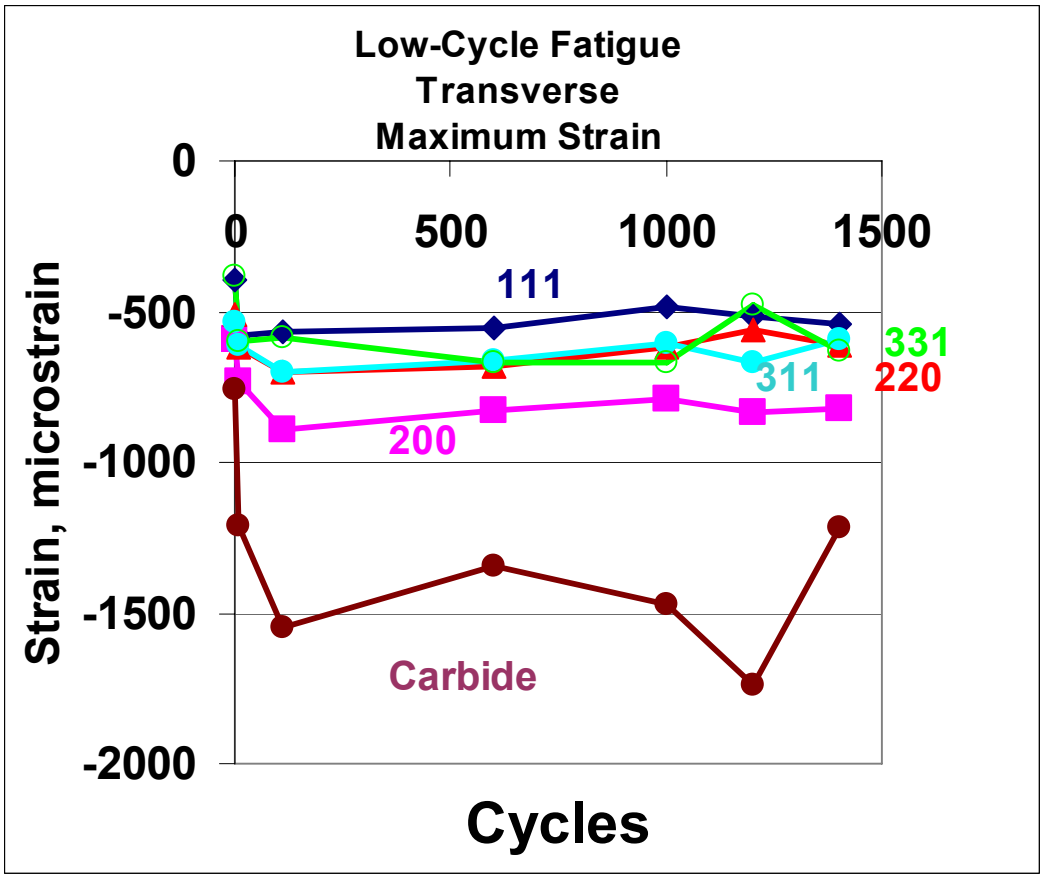

Figure 6.12: The *hkl* strains versus cycles of fatigue at the maximum tensile strain, transverse direction.

The transverse strain behavior in the 200 reflection and the carbide reflection, Figures 6.13 and 6.14 respectively, yields an interesting comparison. While the strain accumulates in the 200 direction as fatigue progresses, the strain in the carbide, based on the transverse direction compressive strains, appears to relax strongly after the initial large accumulation in the first 10 cycles. Recall that the transverse direction in compression has a tensile load on the carbide. The relaxation of strains here suggests that the poisson's tension during compression in fatigue may cause debonding or cracking in the carbides during repeated cyclic loading.

6.7 Conclusions

In tension-tension fatigue of HAYNES 230 alloy, at high loads, the internal strains saturate in the first 1000 cycles. Under the conditions tested, the residual strains after a uniaxial tension test and 42,417 cycles of fatigue are very similar. There are slight trends in relaxing and increasing residual strains over the first 100-1000 cycles. There appears to be no significant relaxation by 85% of the fatigue life. The initial macroscopic strain of 15% appears to have largely saturated the internal strains by the first cycle. Future testing at lower σ_{max} should reveal the internal strain behavior over the initial stages of fatigue.

In tension-compression fatigue the internal strain accumulation is significant in the initial stages of fatigue. This is a much larger effect than seen in the higher maximum stress tension-tension test. Although the strain controlled nature of the experiment meant that there was plastic strain occurring on every

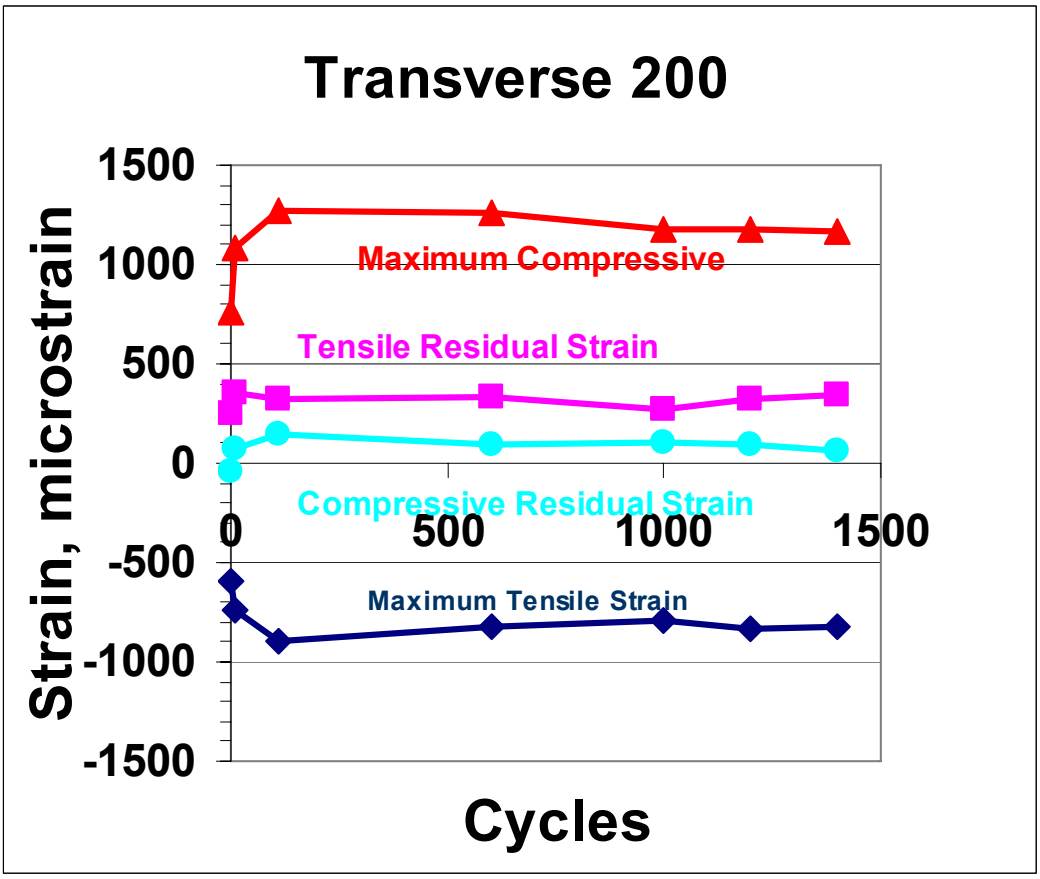

Figure 6.13: Strain accumulation in the 200 reflection, transverse direction, at different points along the cyclic stress-strain curve.

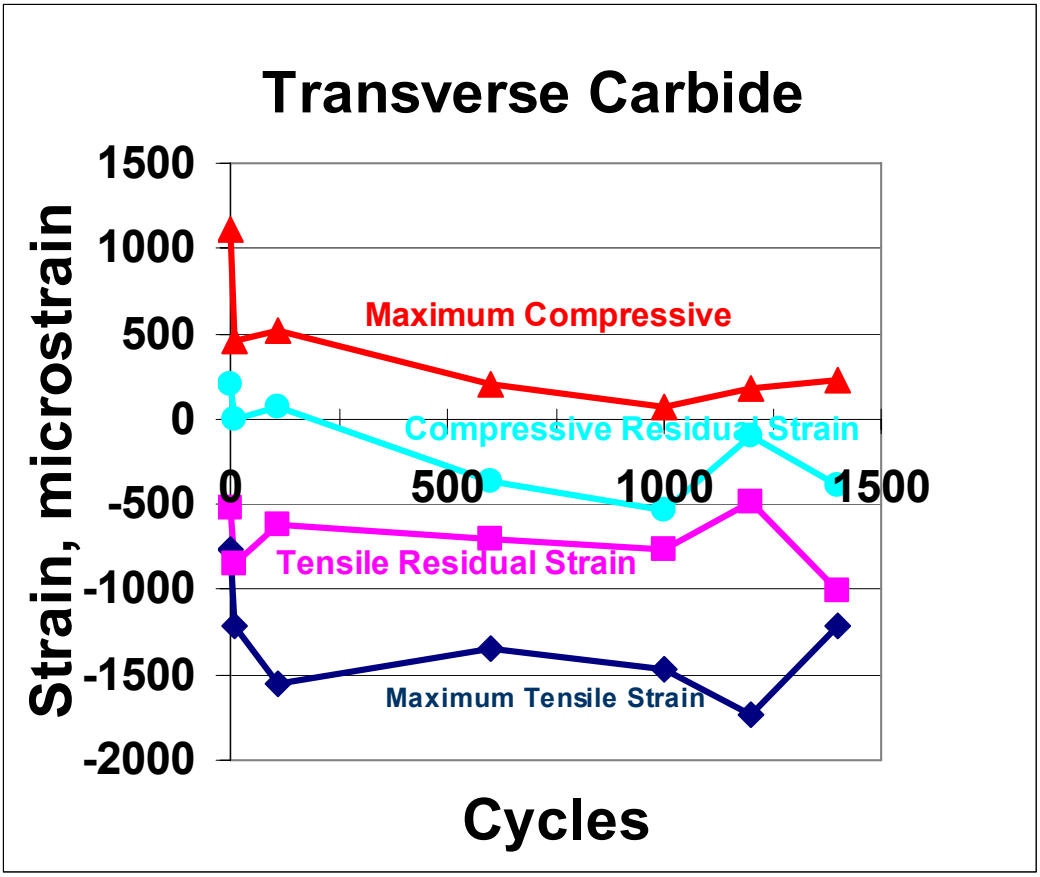

Figure 6.14: Strain accumulation in the 333 carbide reflection, transverse direction, at different points along the cyclic stress-strain curve.

cycle, internal elastic strains did saturate after the first 100 cycles of fatigue. The experiment ended prematurely due to sample alignment issues, so only the first 15% of the fatigue life was explored. However, the strains in the transverse direction in the carbide reveal a relaxation during the compression part of the cycle. This may be a sign of incremental debonding or cracking in the carbides as fatigue progresses.

Chapter 7

Texture

7.1 Introduction

Initial crystallographic texture has important effects on the tensile loading behavior of alloys. Depending on the plate thickness and heat treatment state of HAYNES 230, various initial textures were measured in as-received samples. The implications of these as-received textures on the subsequent loading behavior of this alloy are discussed in this chapter, as well as modeling to show that the final texture is a logical result of the initial conditions.

7.2 Experiment

All textures were measured on the HIPPO diffractometer at LANSCE. The sample was placed in the instrument with the loading axis perpendicular to the incident neutron beam. The neutron beam was collimated to 10 x 10 mm^2, which illuminated approximately 300 – 800 mm^3 of the sample's volume, depending on the sample diameter. Patterns were taken in four different orientations rotated about the sample's loading axis (0, 45, 67.5 and 90 degrees), creating 98 unique histograms. For the HAYNES 230 sample, patterns were taken for 2 minutes per sample orientation for a total beam time of 8 minutes per sample.

Pole figures were calculated using the spherical harmonics representation of the orientation distribution function (ODF) found in the GSAS software [17]. More detailed description of the data analysis can be found in papers by Von Dreele and Vogel [29, 153, 154]. Rietveld refinement was performed on all histograms simultaneously, refining background, lattice parameter, peak profile coefficients, and finally spherical harmonics. No sample symmetry was assumed. Eighth order spherical harmonics were used, as higher order spherical harmonics did not improve the convergence and χ^2 of the data. GSAS output was plotted into pole figures using the Program POD [155].

7.3 Initial Textures

There were two separate as-received textures for the HAYNES 230 samples used for the *in situ* fatigue measurements. The sample's loading direction is out of the page. Figure 7.1 shows the as-received texture of a textureless sample. The maximum texture is 1.06 times random, which is indicates no preferred orientation. Figure 7.2 shows the texture of the second group of as received samples. Here the sample has an interesting bi-modal texture. The maximum texture is 2.62 times random, with the 111 aligned with the sample axis, and the 110 direction aligned perpendicular to the samples axis. This texture resembles a shear texture [25, 156], and is likely to be a product of cross-rolling and an incomplete annealing due to a thicker sample [157].

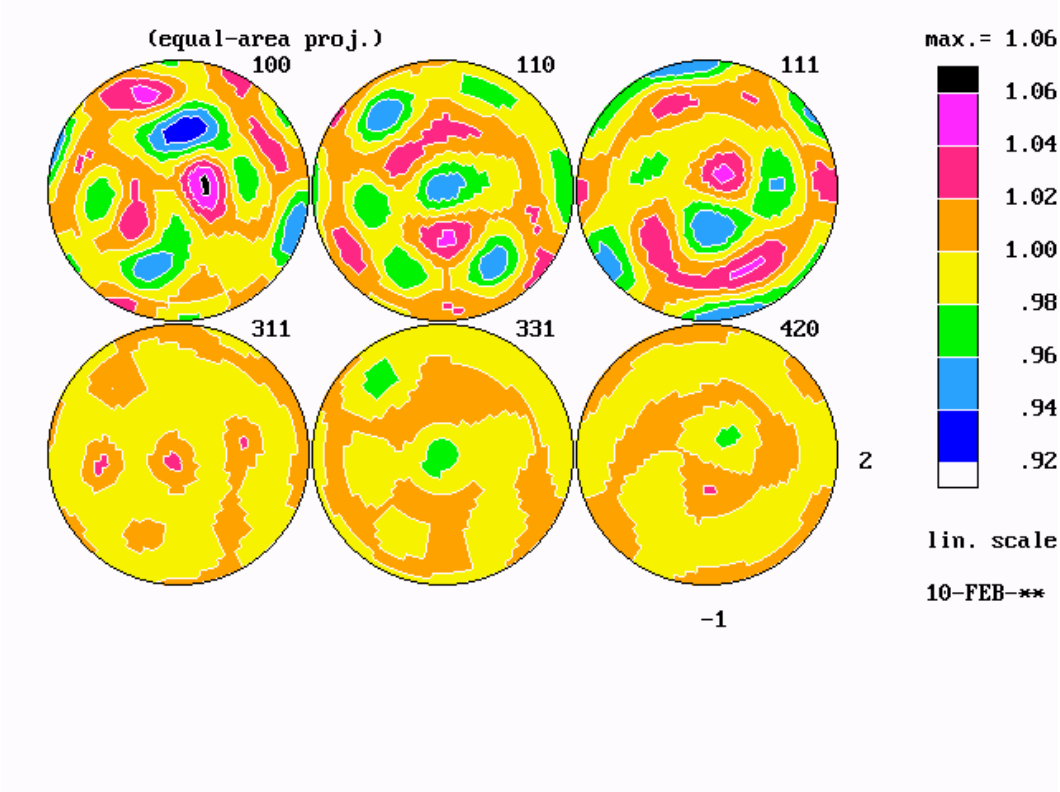

Figure 7.1: As-received texture for HAYNES 230, showing a random, texture-free orientation.

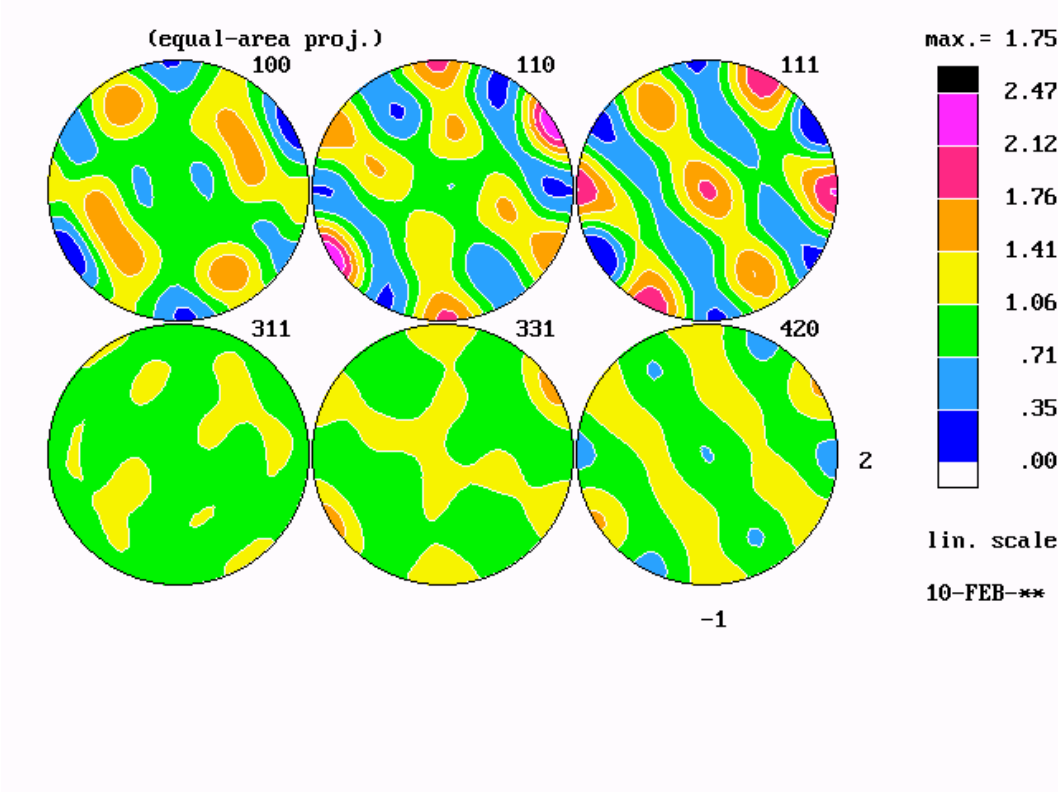

Figure 7.2: As-received texture for HAYNES 230, showing cross rolled plate texture.

Figure 7.3 displays the texture after compression when starting with a texture-free sample. Since the macroscopic compression is only 7%, there is a very weak fiber texture of 1.36 times random. The 110 direction aligned with the loading axis and the 111 direction is perpendicular to it. Figure 7.4 displays the texture after tension when starting with a texture-free sample. Here a stronger fiber texture of 2.21 times random is seen, with the 111 direction oriented in the loading axis. These compression and tension textures are very typical for FCC materials [25, 156].

Figure 7.5 shows the texture after fatigue and tension experiments when starting with the cross-rolled texture. The resulting texture is similar to the starting texture, but with a much stronger 111 texture in the loading axis. Remarkably the texture is very similar after one loading cycle and 110 cycles of fatigue. This shows that the texture does not change in the first stages of fatigue, which is unsurprising in light of the relative similarity in internal strains detailed in Chapter 5 as well as previous studies of texture development during room temperature fatigue of nickel [158].

7.4 Modeling

Similar to the EPSC modeling technique detailed in Chapter 4, viscoplastic self-consistent modeling (VPSC) can be used to model the texture development during loading operations [159, 160]. Instead of an elastoplastic hardening model, a viscoplastic model is used. The model is still based on an idea of an Eshleby inclusion in an HEM, but here the grain rotations with applied

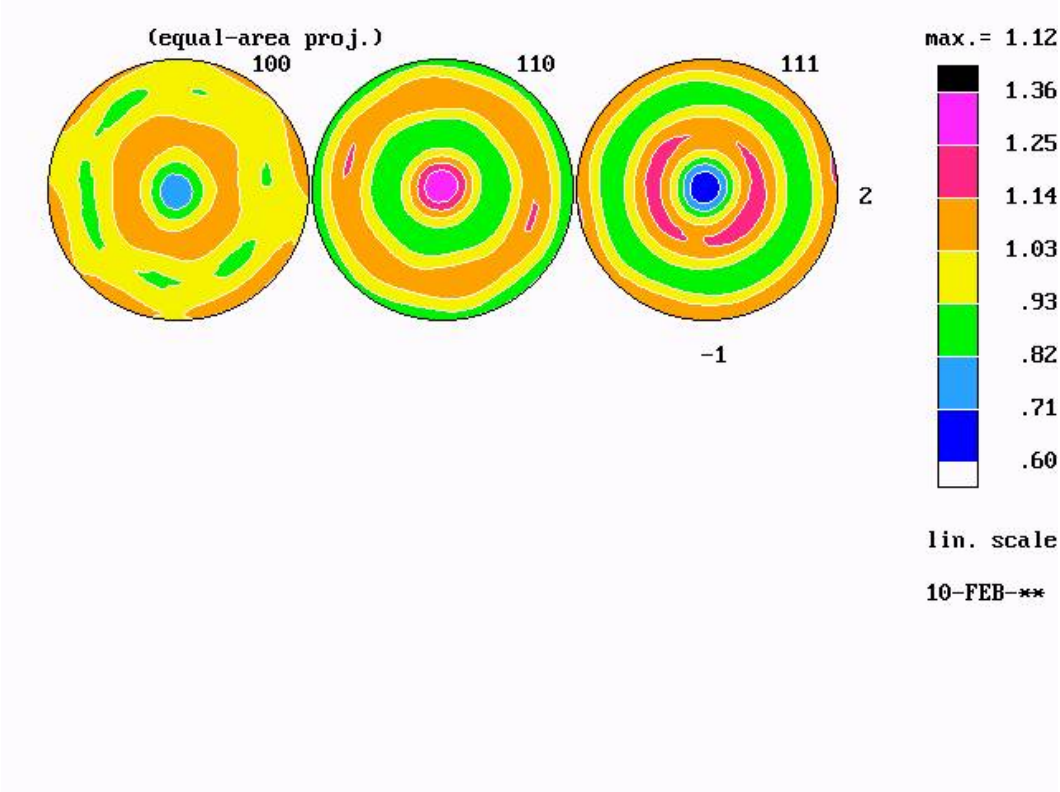

Figure 7.3: Texture for HAYNES 230 after 7% strain in compression, starting from a texture-free sample.

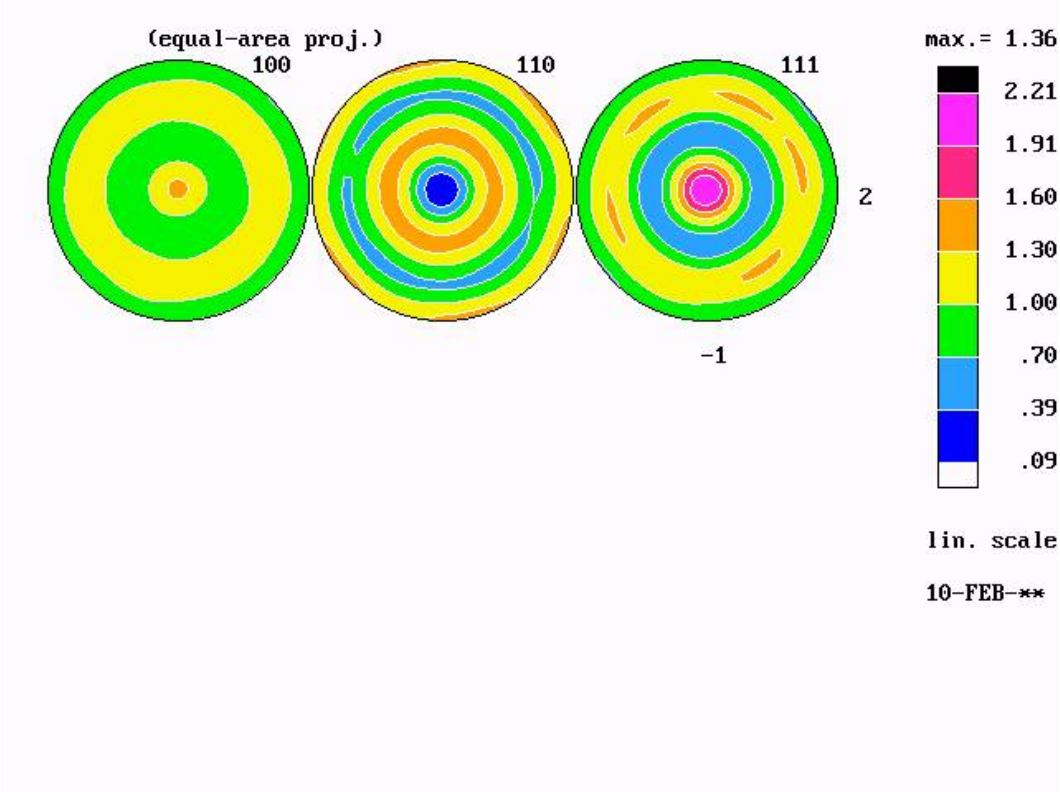

Figure 7.4: Texture for HAYNES 230 after 15% strain in tension, starting from a texture-free sample.

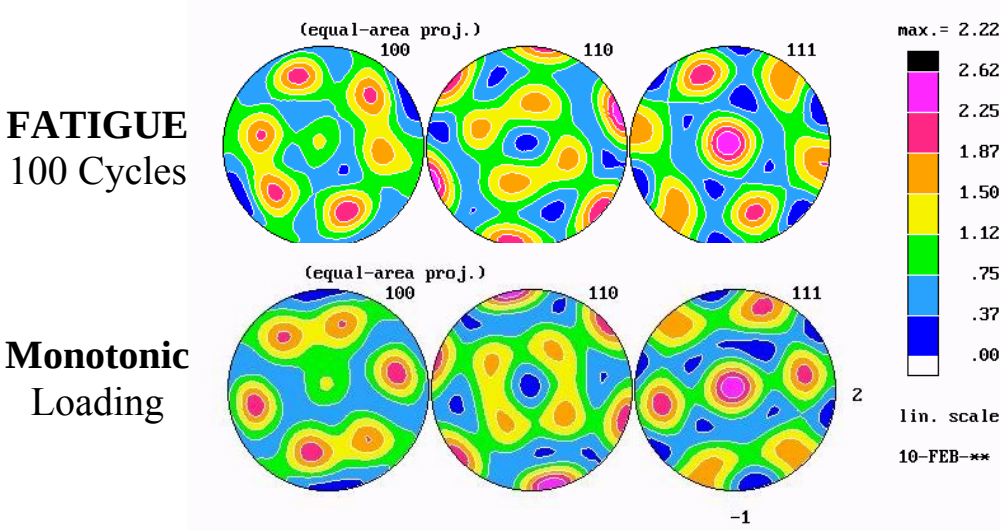

Figure 7.5: Texture for HAYNES 230 after 15% strain in fatigue (top) and simple tension (bottom), starting from a cross-rolled sample.

strain are modeled. No elastic deformation takes place. Each included grain is allowed to deform via twining or slip mechanisms. The grain slips and reorients with the applied deformation and within the constraints of the HEM. The 111/<110> slip mechanism is assumed for FCC crystals, with no twinning mechanism allowed. Hardening occurs according to a Vocce model, however the interplay of various slip and twinning mechanisms seen in lower symmetry materials [70, 71, 159] does not occur in an FCC material.

The actual initial measured textures (as seen in Figures 7.1 and 7.2) are used as the starting point of the model. Figure 7.6 displays a comparison between the modeled texture and the experimentally measured texture for the *in situ* loading experiment (Figure 7.5). The model very closely captures both the form of the texture pole figure as well as the degree of texture. The model slightly over estimates the maximum texture, but this is typical of this type of model due to the bulk average nature of the neutron measurements versus the smaller volumes treated in the model [159]. This clearly shows that the final textures seen in figure 7.5 are a result of typical FCC deformation mechanisms superimposed on the initial cross-rolled texture, seen in Figure 7.2.

Similarly, the experimental and modeled final textures after compression and tension on the texture-free samples are displayed in Figure 7.7 and 7.8, respectively. As expected, a fiber texture is predicted in the model, matching the experimental data closely, except for the usual slight overestimation of the maximum texture. This fiber texture is typical for FCC metals when starting from a texture-free sample [25, 27].

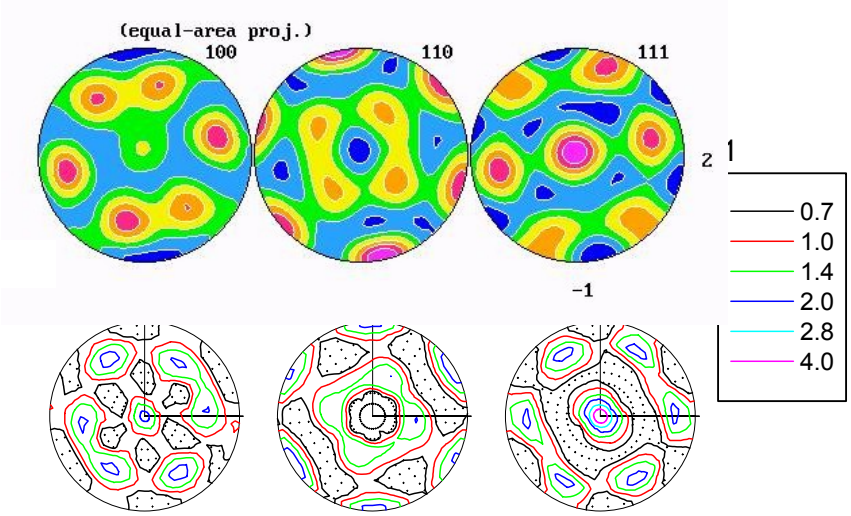

Figure 7.6: Experimental (top) and modeled (bottom) texture for HAYNES 230 after 15% strain in tension starting from a cross-rolled sample texture.

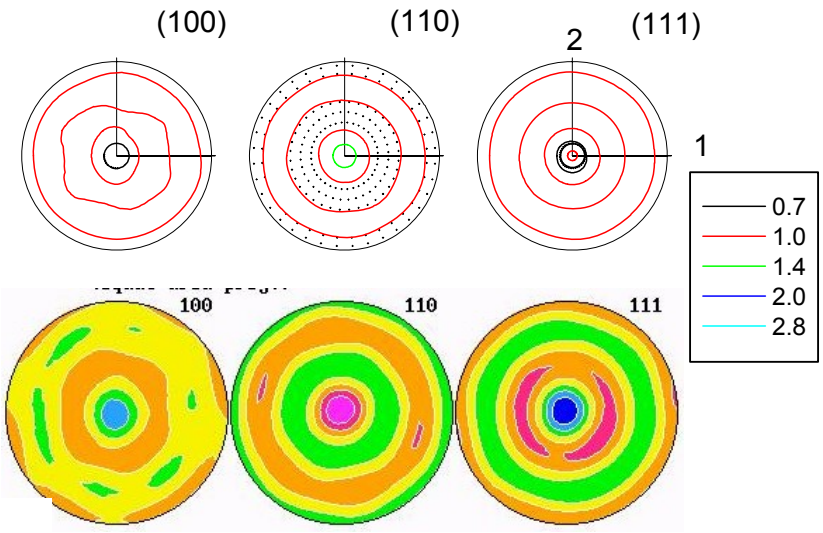

Figure 7.7: Modeled (top) and experimental (bottom) texture for HAYNES 230 after 7% strain in compression starting from a random sample texture.

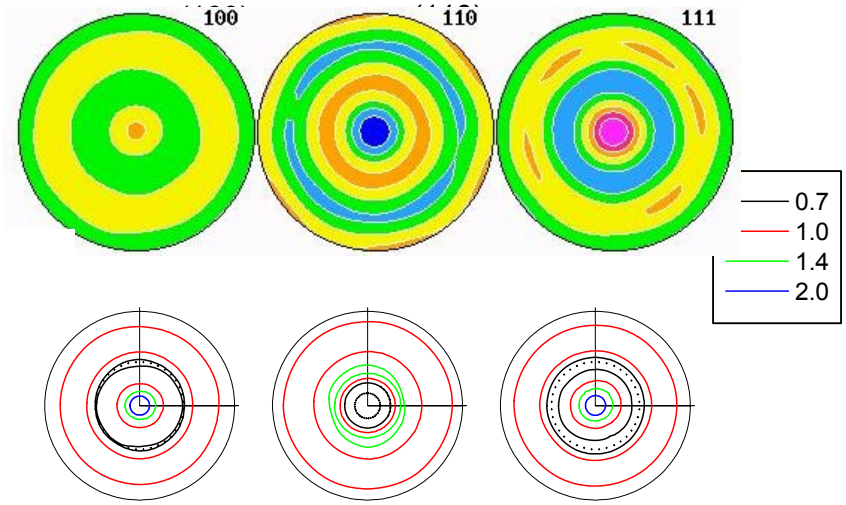

Figure 7.8: Experimental (top) and modeled (bottom) texture for Haynes 230 after 14% strain in tension starting from a random sample texture.

7.5 Texture's Effect on Internal Strains

An initial starting texture implies a degree of preexisting work hardening in a material. The material has already undergone a series of deformations and grain rotations and may be resistant to further loading because of this. The texture pole figure seen in figure 7.2 shows that not only is there an existing texture in the as-received condition, but it is already aligned with the sample axis. Meaning the expected final texture after loading, 111 direction oriented with the loading axis, is already in the sample. For a subsequent tensile experiment, the material would act as if it had been work hardened.

Figure 7.9 shows the macroscopic stress-strain curves strains measured during tensile experiments for two samples: the texture-free initial condition (Figure 7.1) and the textured initial condition (Figure 7.2). The final textures for these two experiments are shown in Figures 7.4 and 7.5, respectively. The texture-free sample yields before the textured sample. Additionally, the texture-free sample has a much higher strain at the maximum load of 700 MPa than the textured sample, 18% versus 15%. Both of these behaviors are similar to the effect one would see from initial work hardening of a material.

Figure 7.10 displays the elastic lattice parameter strains measured in the axial direction. The textured sample clearly accumulates less strain than the texture-free sample. Again, this is consistent with the work hardening needed to create the texture. The same effect is noted in the *hkl* specific strains, as seen in Figure 7.11. The strain in both the 111 and 200 reflections is less in the textured sample.

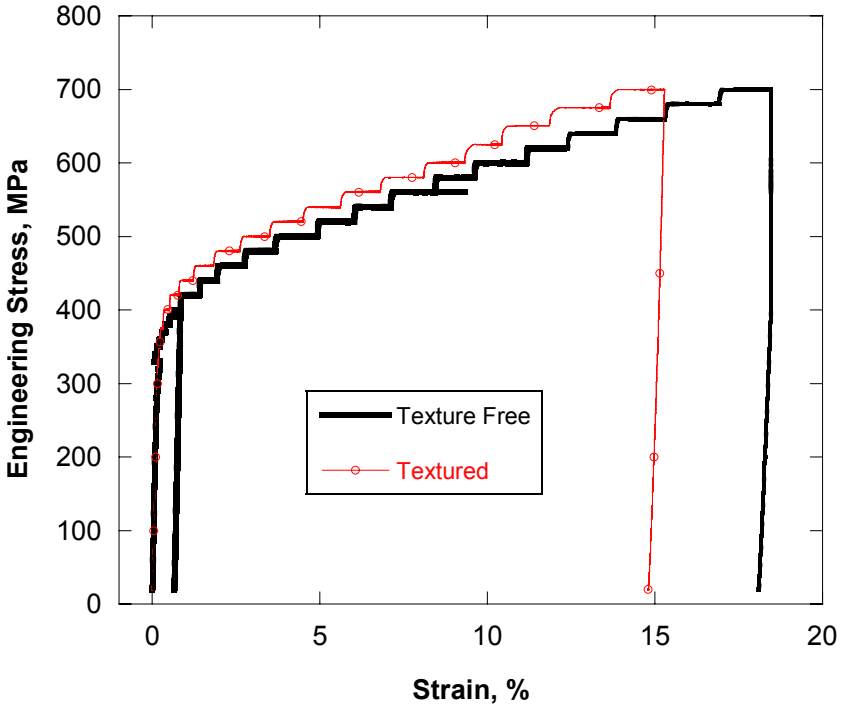

Figure 7.9: Difference in macroscopic loading curves between the random sample and the pre-textured sample.

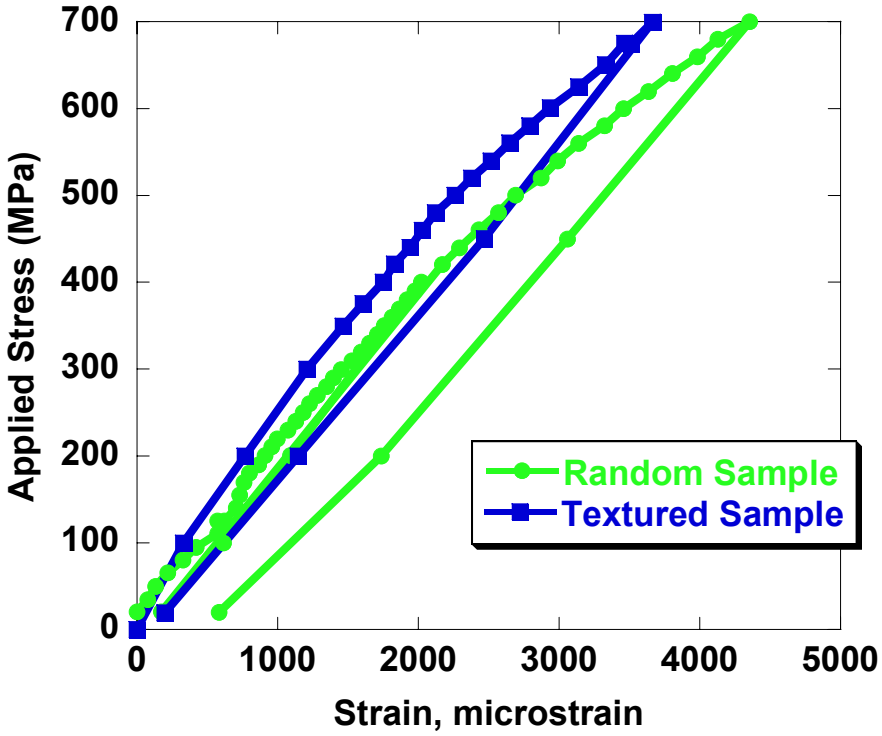

Figure 7.10: Difference in elastic lattice strains between random and pre-textured samples.

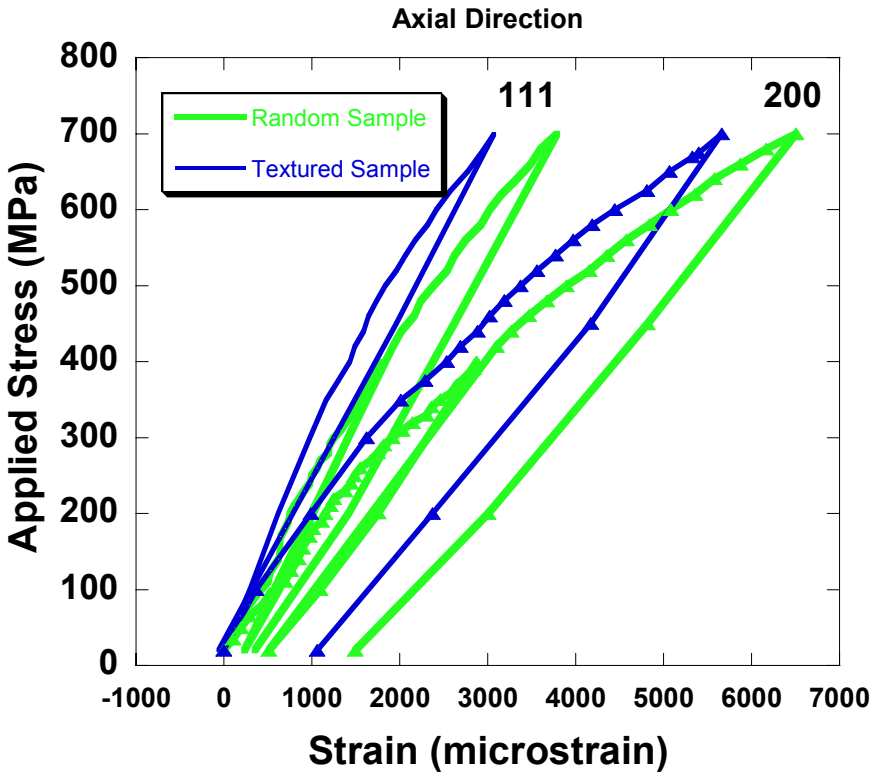

Figure 7.11: Difference in *hkl* specific strains between random sample pre-textured samples.

7.6 Conclusions

Clear differences in the loading behavior of HAYNES 230 are noted with respect to the initial texture. The unusual bimodal textures seen in some samples are a result of incomplete annealing after material processing, particularly cross rolling. The final textures, as shown by experiment and VPSC modeling, are a superposition of the initial texture and typical FCC deformation mechanisms. The effect of initial texture on the macroscopic and internal strain during loading underscores the importance of understanding the texture of samples before using them as basis for comparison. Small changes in starting texture can easily obscure other subtle changes during loading experiments.

Chapter 8
Nonlinear Resonant Ultrasound Spectroscopy

8.1 Introduction

While internal strains are easily measured by peak position shifts, there are a host of fatigue effects that are not easily measured using neutron diffraction. Plastic deformation and the resulting increase in dislocation density is convoluted with grain size effects and strain inhomogeneity in changes in the peak width [13]. Additionally, diffraction is not directly sensitive to microcracking and void formation. Nonlinear acoustic techniques [128, 130] however, are more able to determine a degree of damage in a material, giving a qualitative measure of plastic and cracking effects due to fatigue testing. This chapter compares a series of measurements made using Nonlinear Resonant Ultrasound Spectroscopy (NRUS) and *ex situ* neutron diffraction on the same set of prefatigued samples of HAYNES 230.

8.2 Experiment

Samples were tested on a Materials Test System (MTS) machine, model 810, under load control conditions using a sinusoidal wave form at 10 Hz. The samples were tested at an R ratio of 0.1 with a σ_{max} of 700 MPa. The cylindrical, button-head test specimens employed had a gauge-length of 1.464 cm and a diameter of 0.488 cm. The specimens had a surface roughness of 0.2 μm along the

gauge-length section. An as-received sample and five prefatigued samples were prepared for these experiments. The prefatigued samples were created by interrupting the fatigue tests at 10, 40, 50, 60 and 70 thousand cycles. The fatigue life under these conditions was found to be approximately 75,000 cycles to failure.

During the neutron experiment, each sample was placed in the center of the beam on the SMARTS diffractometer using a jig to ensure accurate positioning. Each sample was exposed for approximately $1x10^6$ microamp hours, ensuring low error bars on the strain measurement of approximately 20-60 με. The as-received sample was tested multiple times to determine the error bars due to positioning. The strain measurements were repeatable within 20 με.

During the NRUS experiments, each sample was glued to a transducer. The transducer was attached to a signal generator to create waves in specified frequency ranges. The vibrations and resonance peaks in the sample were measured with a laser reflectometer and recorded with Labview software. A schematic of the experiment is seen in Figure 8.1. Initially a sweep across a wide range of frequencies is performed to see all the resonant peaks, Figure 8.2. Then a strong single resonant peak is chosen, in this case, the large peak around 12 KHz. Finally, sweeping at a small range around the resonant peak occurs at increasing voltages.

In classically elastic materials, the amplitude of the resonant peak changes as the voltage is increased. However, in samples with discontinuities and inelastic behavior, the resonance peak will change both in amplitude and in frequency [128, 130]. The amount of the shift is related to how inelastic the material is. This

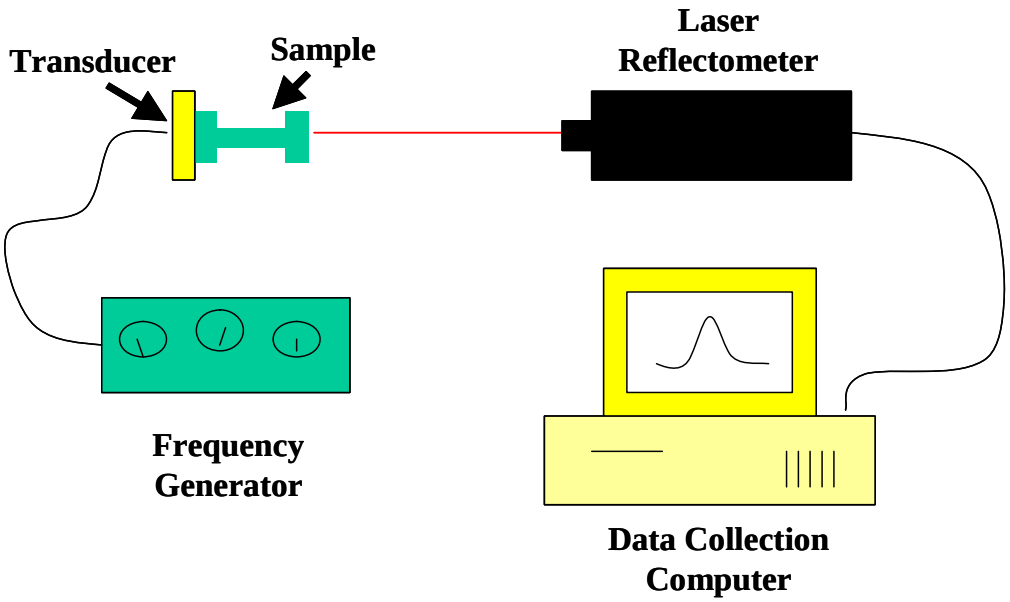

Figure 8.1: A schematic of the experimental set up for the NRUS experiments.

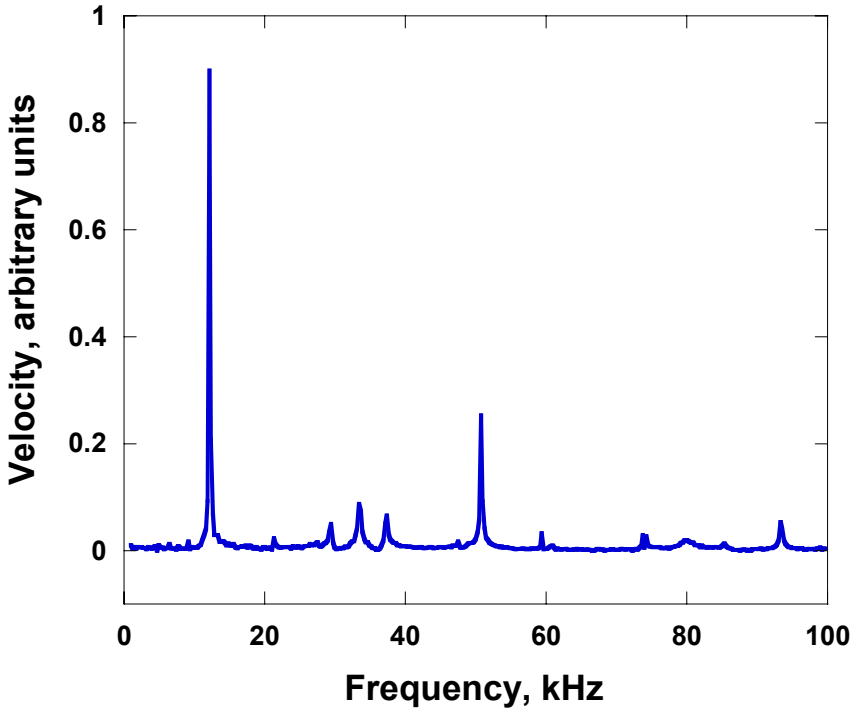

Figure 8.2: Resonance peaks for the as-received HAYNES 230 sample.

technique is used frequently with rocks, which are highly inelastic materials due to amorphous regions, voids, cracks, and composition changes [130]. Typical metals are very crystalline and highly coherent, thus behaving elastically. Fatigue damage manifests itself in a variety of mechanisms such as, high dislocation density, microcracking and void formation. These mechanisms will result in an inelastic type response to the acoustic input allowing for a qualitative measurement of fatigue damage.

8.3 *Ex Situ* Neutron Results

As seen in the chapter on fatigue, neutron diffraction is relatively insensitive to the effects of fatigue under the tested conditions after the first cycle. These *ex situ* experiments confirm the *in situ* results presented earlier. The elastic *hkl* strains, Figure 8.3, do not change appreciably between the 10,000 cycle and 70,000 cycle samples. More significantly there is virtually no change in the peak width between the 10 and 70,000 cycle samples, Figure 8.4, and these samples are virtually indistinguishable using neutron diffraction. Finally, Figure 8.5 shows the peak intensity as fatigue progresses for these samples. Changes in intensity suggest changes in texture; however there is virtually no difference between the 10,000 cycle sample and the 70,000 cycle sample. The cumulative effects of fatigue are not measured in these neutron experiments.

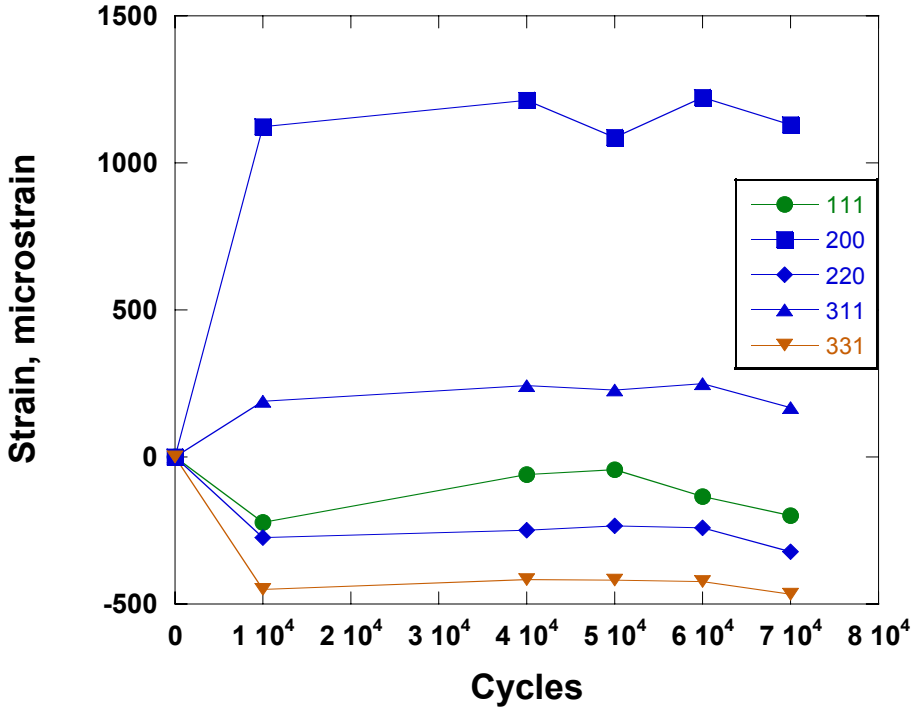

Figure 8.3: Internal strains measured using neutron diffraction for the *ex situ* samples.

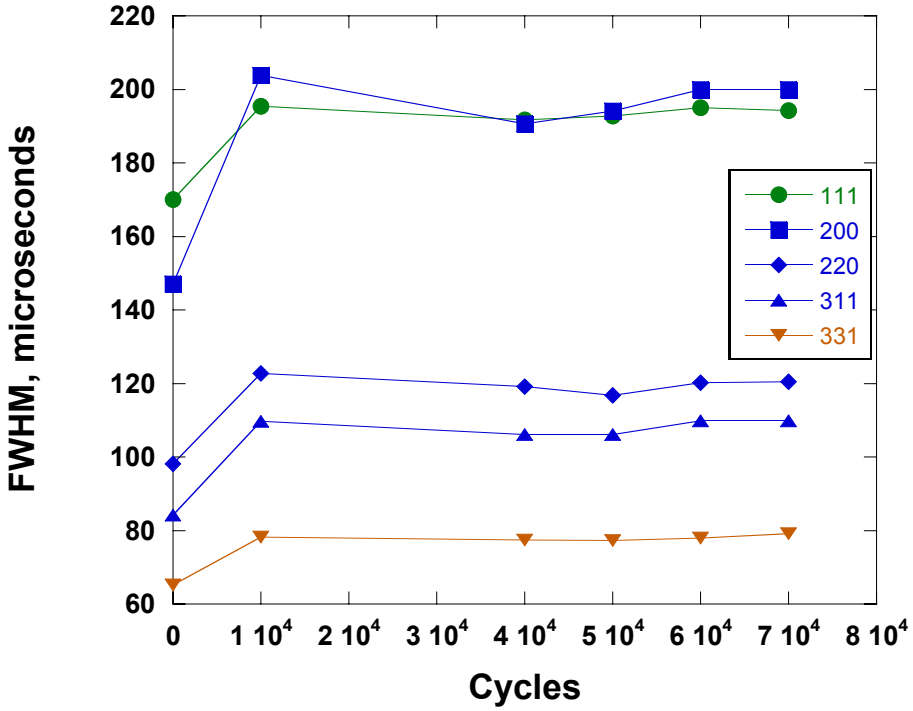

Figure 8.4: Peak width measured using neutron diffraction for the *ex situ* samples.

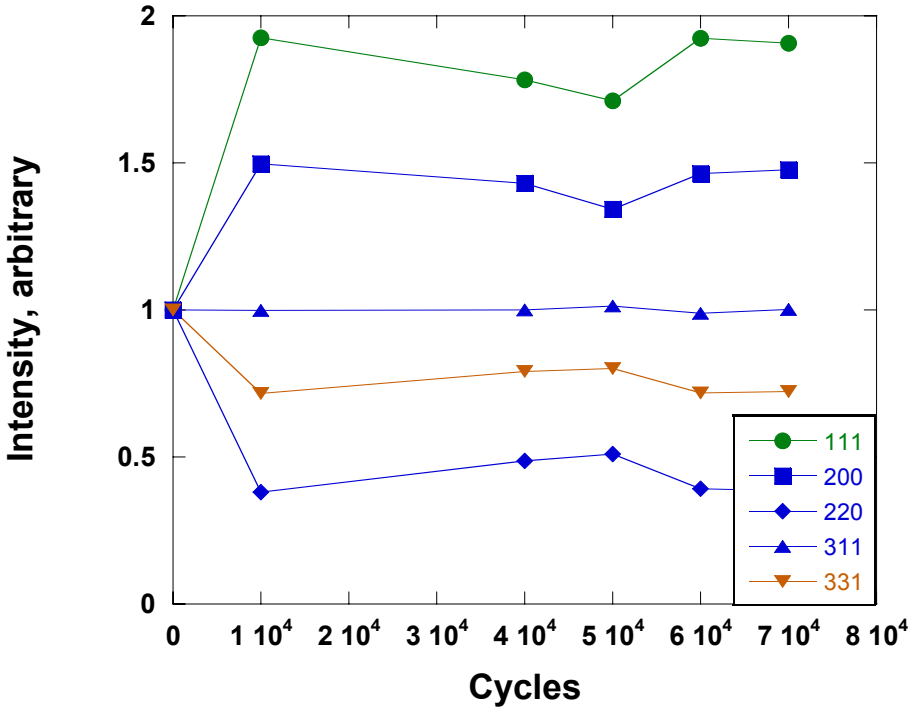

Figure 8.5: Peak intensity measured using neutron diffraction for the *ex situ* samples.

8.4 NRUS Results

Figures 8.6 and 8.7 display the behavior of the resonance peak around 12 KHz as voltage is increased for the as-received and the 70,000 cycle samples, respectively. The as-received sample shows an increase in the amplitude of the resonance peak as the voltage is increased. The peak position, however, does not shift appreciably or systematically. The resonance peak for the 70,000 cycle sample shifts dramatically as the voltage is increased. This difference shows that the 70,000 cycle sample is more damaged than the as-received sample.

By plotting the dependency, or the peak position with applied voltage, for each sample, we can see the degree of peak shift, signifying damage, for each sample, shown in Figure 8.8. There is a clear progression of damage from the as received sample to the 70,000 cycle sample. Significantly, the as-received and 10,000 cycle samples are very similar. This contrasts greatly with the neutron results where the only significant differences noted are between the as-received and 10,000 cycle samples.

8.5 Conclusions

The diffraction results presented here and in Chapters 5-7 clearly show that elastic strain, texture and dislocation development are primarily noted during the initial plastic strain. However these effects no longer play a large role during subsequent tension-tension fatigue deformation. These initial effects are easily measured by neutron diffraction. The accumulation of damage, in the form of

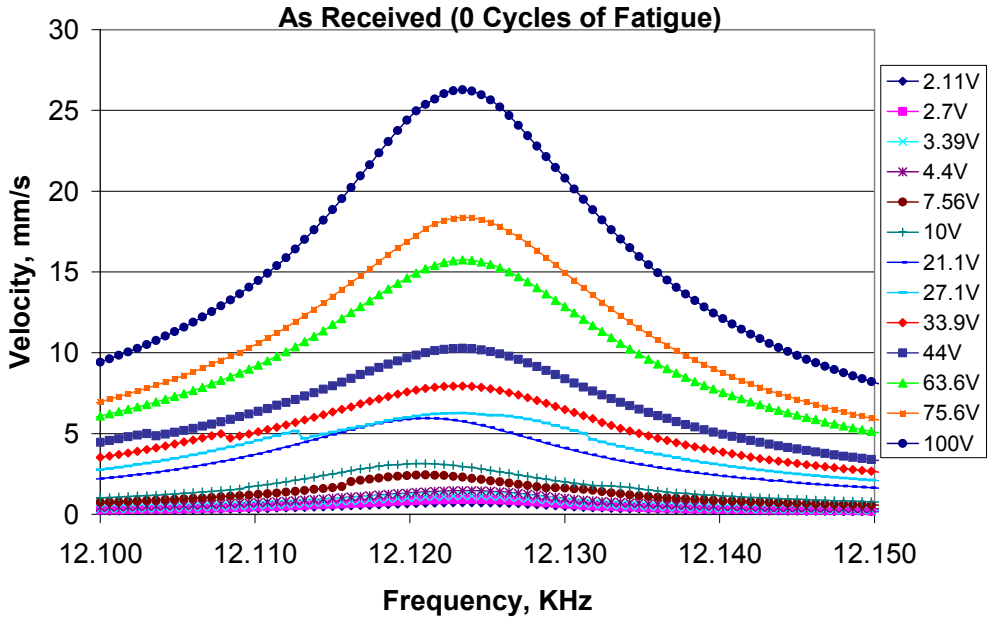

Figure 8.6: Resonance peak shift with increasing voltage for the as-received sample.

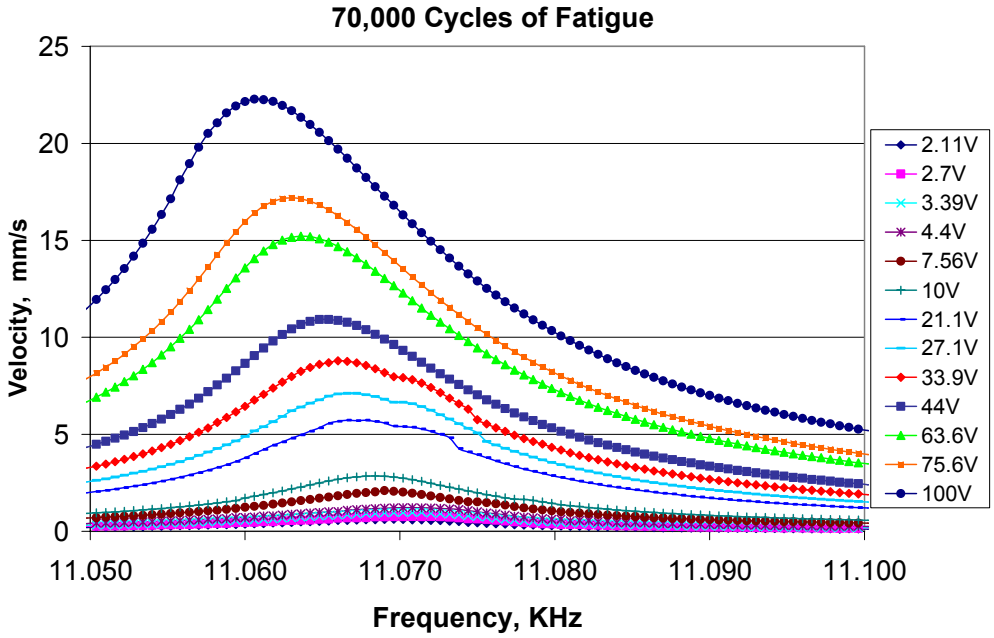

Figure 8.7: Resonance peak shift with increasing voltage for the as 70,000 cycle sample.

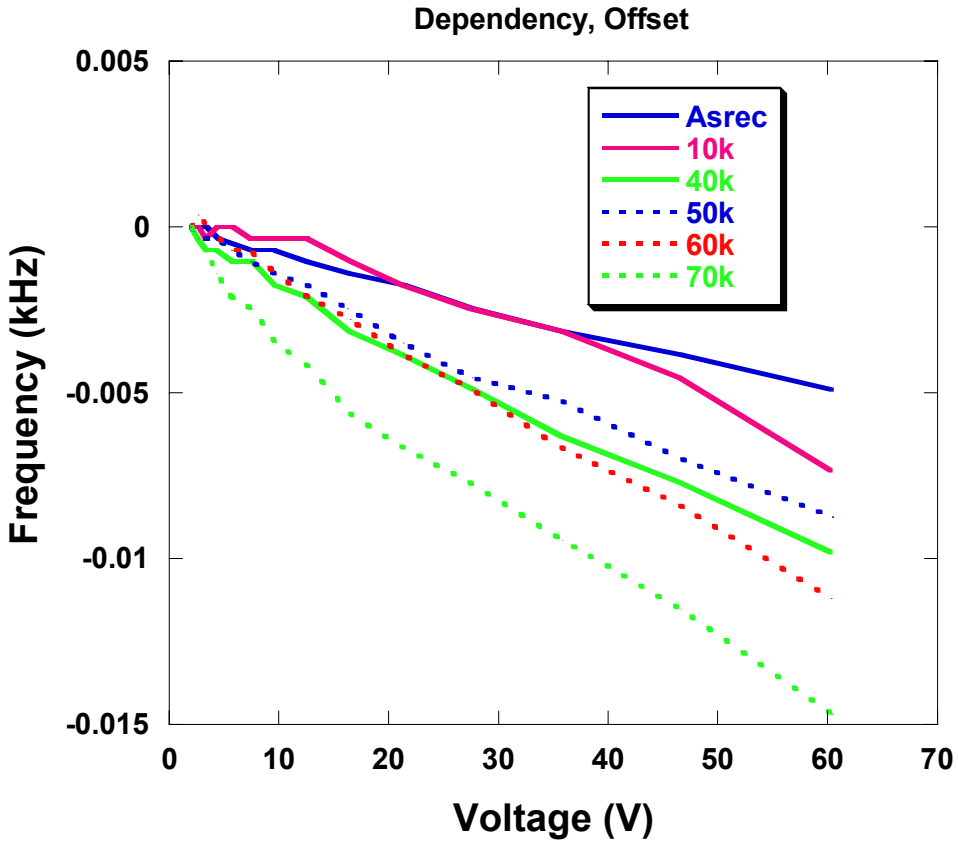

Figure 8.8: Summary of the dependency (resonance peak shift with increasing voltage) for the complete set of *ex situ* samples.

cracking, voids and other inhomogeneities, is shown clearly in the NRUS measurements. Thus, these two techniques are complimentary showing both the initial changes over the first cycle and the accumulation of fatigue effects as failure is approached.

Chapter 9
Infrared Thermography

9.1 Experimental Procedures

Uniaxial high-cycle fatigue (HCF) tests were performed on HASTELLOY C-2000 alloy test specimens. The test specimens were machined from bars which had been hot rolled in the temperature range of 1176-1204 ºC, annealed at 1149 ºC, and then water quenched. The cylindrical test specimens employed had a gauge-length of 1.464 cm and a diameter of 0.488 cm. The specimens had a surface roughness of 0.2 μm along the gauge-length section. The fatigue tests were performed in air on a MTS (Materials Test System) machine (Model 810) using a sinusoidal waveform at 20 Hz under load-controlled conditions. The experiments were conducted under tension-tension conditions with an R ratio ($\sigma_{min}/\sigma_{max}$, where σ_{min} and σ_{max} are the applied minimum and maximum stresses, respectively) of 0.1.

An Indigo Phoenix thermographic infrared (IR) imaging system was used with a 256 x 256 pixel focal plane array InSb detector. The temperature resolution was 0.015 ºC, and the spatial resolution was 5.4 μm with a microscopic lens. Full frame data could be acquired at 128 Hz; reduced frame sizes could be used at much higher rates. The present thermographic results were acquired at a rate of 60 Hz for all but the data presented in Figure 3, which contains 60 Hz and 1 Hz data.

During testing, the samples were coated with a thin layer of matte black paint to reduce IR reflections.

9.2 Results and Discussion

The S versus N (applied stress versus fatigue cycles) curve of HASTELLOY C-2000 alloy at 20 Hz is shown in Figure 9.1. The fatigue-endurance limit (corresponding to a fatigue life of 2 x 10^6 cycles) is at a stress range ($\sigma_r = \sigma_{max} - \sigma_{min}$) of 382 MPa. Figure 9.2 shows the average temperature versus time across a 3 mm x 3 mm region at the center of the gauge-length section during the first 15-20 seconds of fatigue tests at different stress ranges.

Figure 9.3 shows the temperature as a function of time for a complete test measured at the center of the gauge-length section for a sample tested at a σ_r of 626 MPa. Note that this σ_r was quite large, with the σ_{max} approximately equal to 180% of the yield strength. As the test began, the temperature increased from room temperature to a maximum of 73 ºC (Stage I). The sample then slowly cooled to an equilibrium temperature of approximately 70 ºC as the test proceeded (Stage II). Finally, the temperature increased to 103 ºC as the specimen failed (Stage III). After failure, the temperature then dropped to room temperature (Stage IV). The initial maximum and equilibrium values varied with the stress range as seen in Figure 9.2. Increasing the stress range from 382 MPa to 516 MPa increased the temperature in Stage II from 24 °C to 38 °C (Figure 9.2).

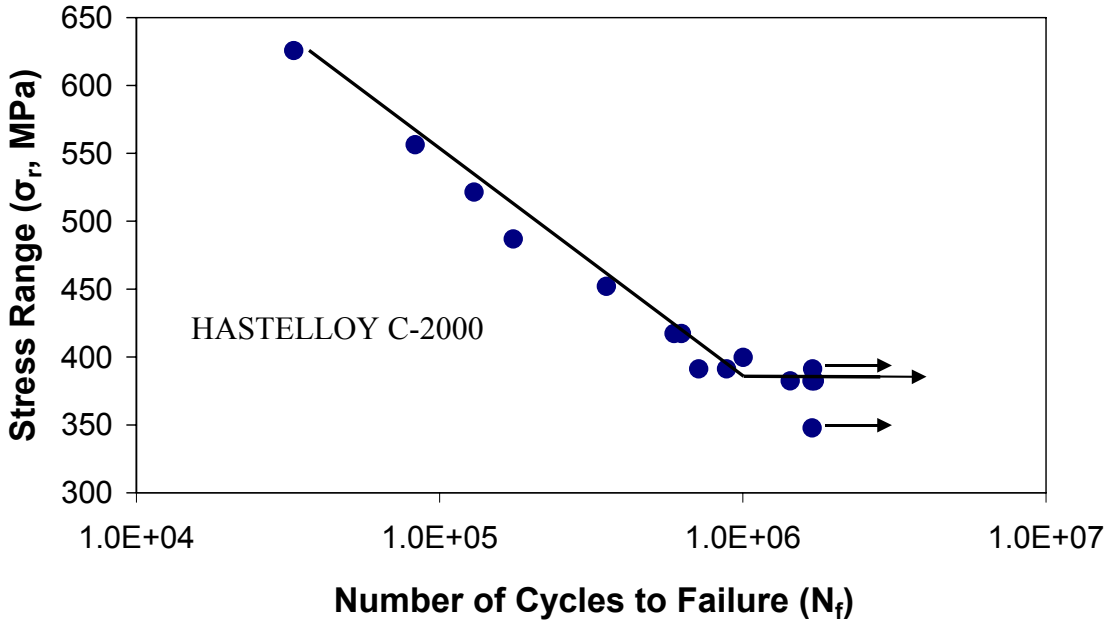

Figure 9.1: S-N curve for C-2000 alloy at R = 0.1, 20 Hz.

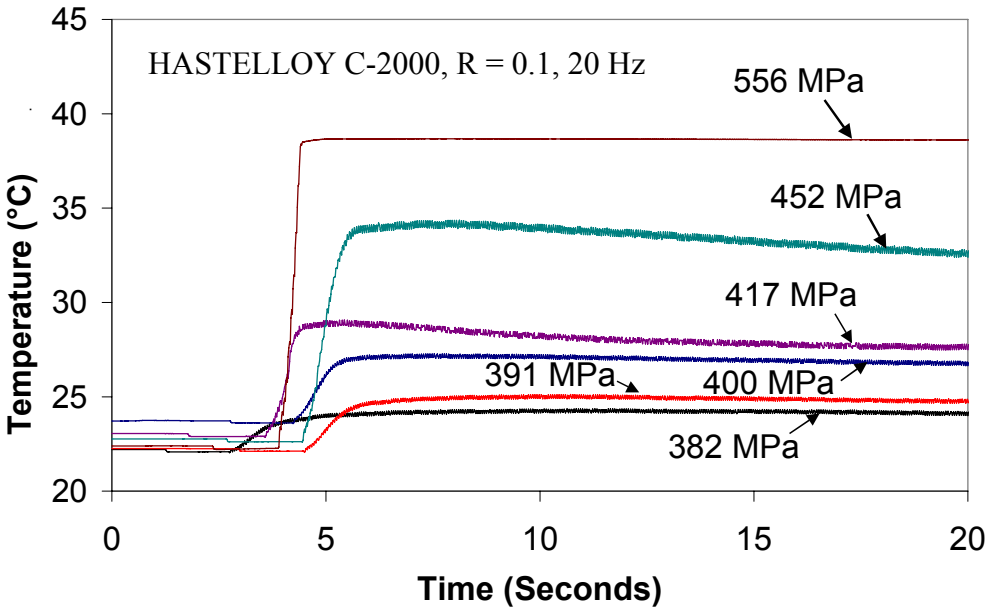

Figure 9.2: Temperature profiles at different stress ranges.

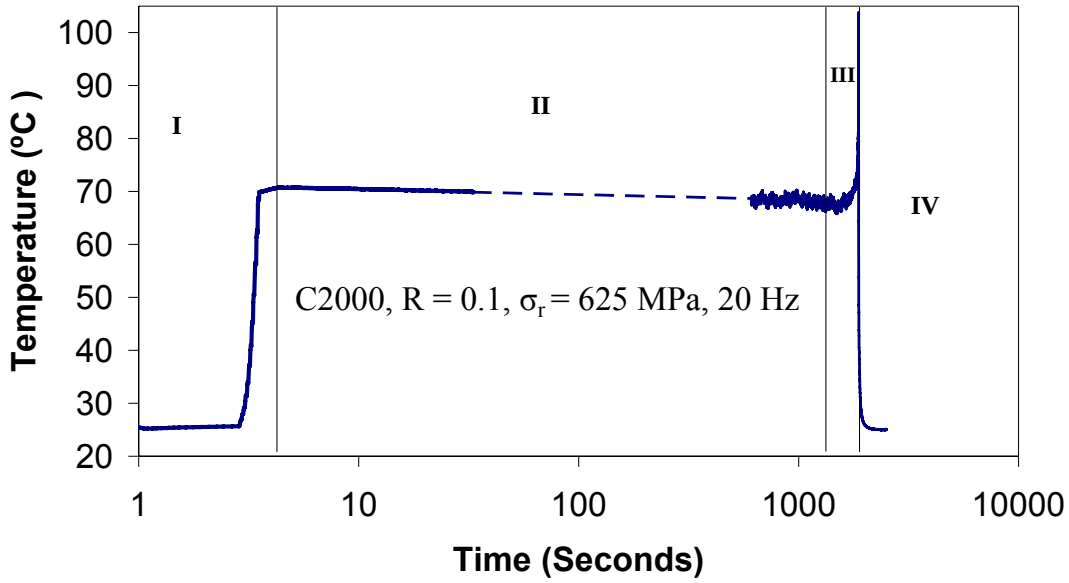

Figure 9.3: Typical temperature profile during complete fatigue test.

The temperature-time profiles in Figures 9.2 and 9.3 result from the following effects. In Stage I, the main temperature rise was due to the inelastic effects, such as plastic deformation and internal friction; in this case plastic deformation was responsible for the bulk of the temperature rise. The thermoelastic effects were responsible for the temperature oscillations. During Stage II an equilibrium was reached. Heat generated from the inelastic effects was balanced by heat losses to the sample's environment. Again, the small temperature oscillations in Stage II were due to thermoelastic effects, which will be discussed later (Figure 9.4). In Stage III, the rapid increase of temperature was due to the inelastic effects associated with the initiation and propagation of cracks and plastic deformation, as the sample began to fail. The peak temperature was associated with final failure. Stage IV consisted of the sample cooling back to room temperature following failure.

The detail of the temperature-time profile due to thermoelastic effects on a sample tested in air at 20 Hz and with a σ_r of 382 MPa is presented in Figure 9.4. This data was taken after the temperature equilibrium had been reached. The heat generated within the sample due to plastic, thermoelastic, and inelastic effects was in equilibrium with the heat loss due to conduction and radiation. The temperature fluctuations occurred due to the thermoelastic effects. The application of a tensile load causes a temperature decrease, and the application of a compressive load causes an increase in temperature [143, 144, 147, 161-163]. In this case, since the R ratio is positive and the only stresses present were tensile, the local maxima in temperature occurred at σ_{min}, where the least thermoelastic cooling occurred. The

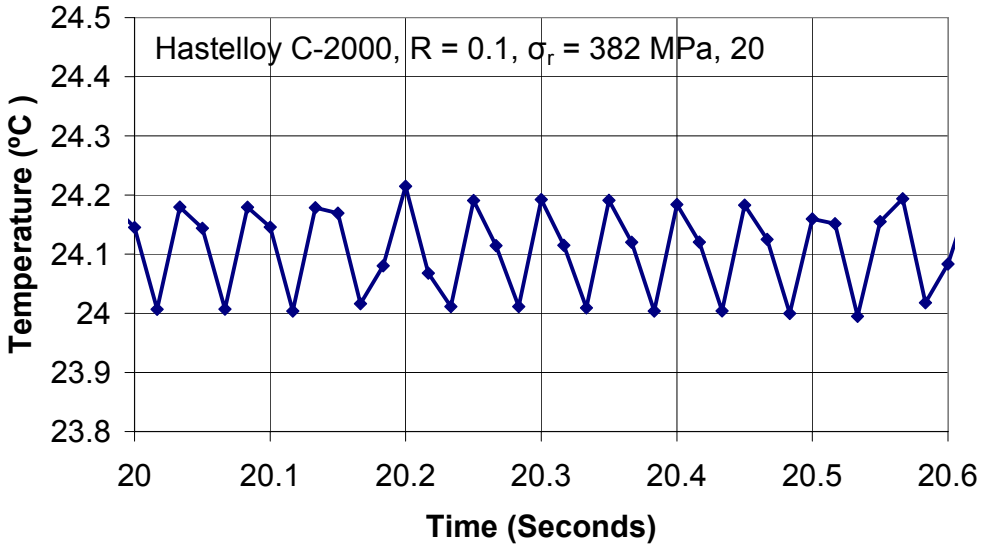

Figure 9.4: Detail of the thermoelastic effects during a σ_r = 382 MPa test.

local minima in temperature occurred at σ_{max}, where the most thermoelastic cooling occurred. Without the thermoelastic effect, the equilibrium temperature would have been slightly higher than the local temperature maxima [146].

Digital images taken from the IR camera at different points during the fatigue life of the sample tested at a σ_r of 391 MPa are exhibited in Figure 9.5. The intensity of the image corresponds to the temperature of the object. Light areas denote higher temperatures and dark areas represent lower temperatures. The images shown in Figure 9.5, from left to right, are taken at 0, 150, and 600 cycles of testing, respectively. The image taken at 0 cycles shows a small temperature gradient from the bottom of the sample to the top. This gradient corresponded to heat being conducted up the sample from the lower hydraulic grip, which was connected to the hydraulic actuator. The middle image, taken at 150 cycles, shows a high-temperature region at the center of the sample and lower temperature regions at the ends of the sample. The far right image, taken at 600 cycles, exhibits a high-temperature region at the center of the sample and lower temperatures at the ends of the sample. However, the temperatures of the end regions at 600 cycles were slightly higher than those at 150 cycles.

Figure 9.6 shows the temperature profile along the center of the sample in the gauge-length direction for each image shown in Figure 9.5. This temperature profile quantifies the information in Figure 9.5. The data at 0 cycles, as mentioned previously, shows the small temperature increase from the top to the bottom of the sample due to the heating of the lower hydraulic grip. The data at 150 cycles indicates that the temperature at the ends of the sample remained constant, but the

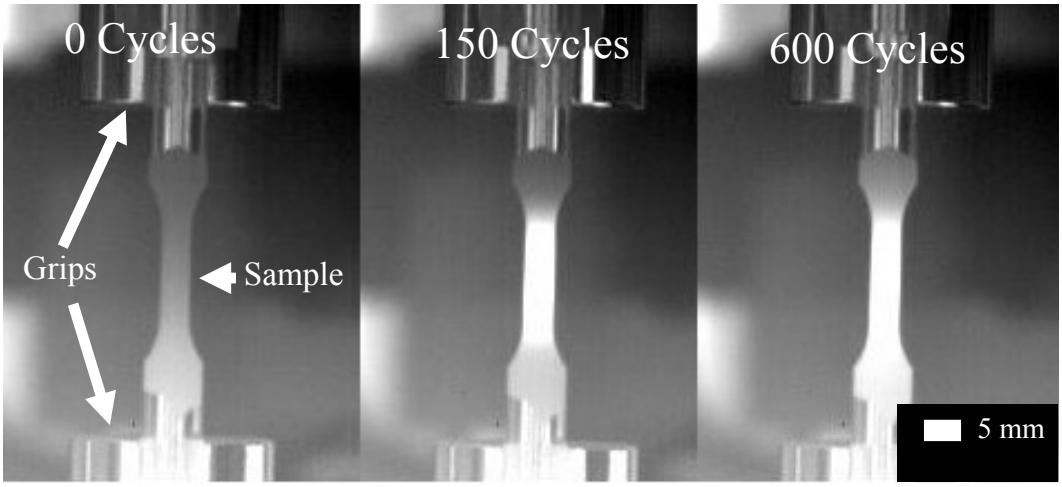

Figure 9.5: Infrared images of the sample tested at σ_r = 391 MPa. Images taken, at 0, 150, and 600 cycles, from left to right.

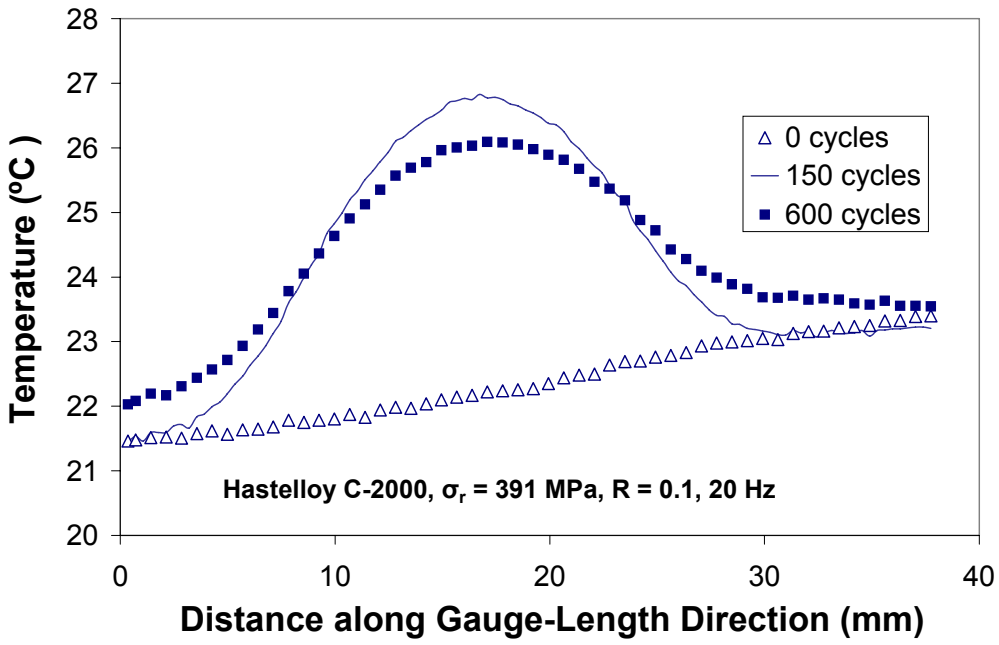

Figure 9.6: Temperature profiles along the center in the gauge-length direction of the sample tested at σ_r = 391 MPa, taken at 0, 150, and 600 cycles.

temperature at the center of the sample was at its peak of about 27 °C. The data at 600 cycles indicates the temperature at the center had dropped as the heat began to conduct away from the center, and the heat generated due to the initial plastic deformation had dissipated. The temperature at the ends of the specimen, however, increased due to heat conduction away from the center.

Furthermore, Figure 9.7 presents the average temperature profile at the center of the sample of the same test shown in Figures 5 and 6. It is clear that the data at 150 cycles was near the peak average temperature, while the temperature at 600 cycles was lower and very close to the equilibrium temperature. Again, these temperature results show the pattern of heat generation and dissipation in a typical fatigue specimen.

9.3 Life Predicition

Plotting the steady-state temperature reached in each fatigue test versus the fatigue life on a logarithmic scale yields a linear relationship, as shown in Figure 9.8. As the temperature increases, the life decreases. Using the given sample geometry, test frequency, material, and R ratio, the relationship between the fatigue life and steady-state temperature can be described by:

$$N_f = 1825.04 T_s^{-3.823} \tag{9.1}$$

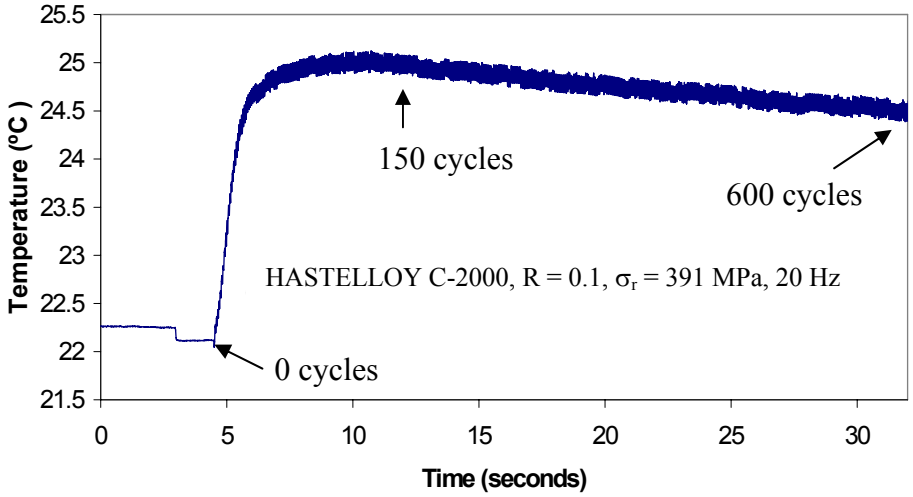

Figure 9.7: Average center temperature of the sample tested at σ_r = 391 MPa.

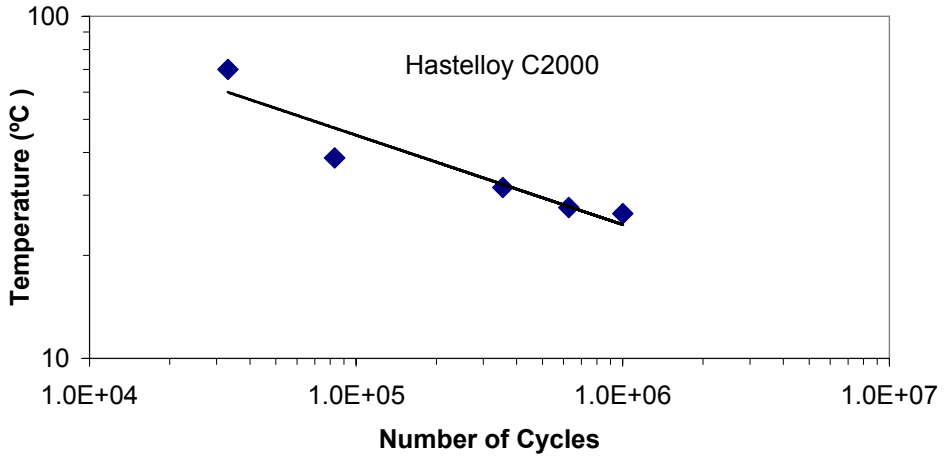

Figure 9.8: Log-log plot of the steady-state temperature versus number of cycles to failure for C-2000 alloy.

with T_s being the steady-state temperature, and N_f the number of cycles until failure. This empirical method is useful in predicting lifetime from temperature, however, more exact methods can be used to predict lifetime from the steady state temperature. Using first-principle calculations, accurate fatigue life predictions can be made after one experiment.

Based on work begun by Jiang [141] and completed by Yang [138, 146], the steady-state temperature can be related to fatigue life from the thermodynamic model:

$$N_f = \frac{C}{\frac{8k(T_s - T_0)}{L_e^{\,2} f} \times \left(\frac{\rho C_p \Delta T}{2\alpha T_s} \right)^4} \tag{9.2}$$

with N_f representing the number of cycles to failure, f the test frequency, L_e the gauge length of the sample, Ts the steady state temperature achieved during fatigue, To room temperature, k the thermal conductivity of the sample, ρ the density of the material, Cp the specific heat, α the thermal expansion coefficient, and ΔT the change in temperature due to the thermoelastic effect. The constant C must be obtained experimentally from an actual experiment. Thus, the steady-state temperature of the specimen, which is typically reached in the first 15-30 seconds of the fatigue test, can be an indication of the fatigue life.

Figure 9.9 displays the fatigue life predicted using Equation 9.2, along with the experimental fatigue life. The constant C was determined using the data from the experiment at a stress range of 382 MPa, so the experimental and

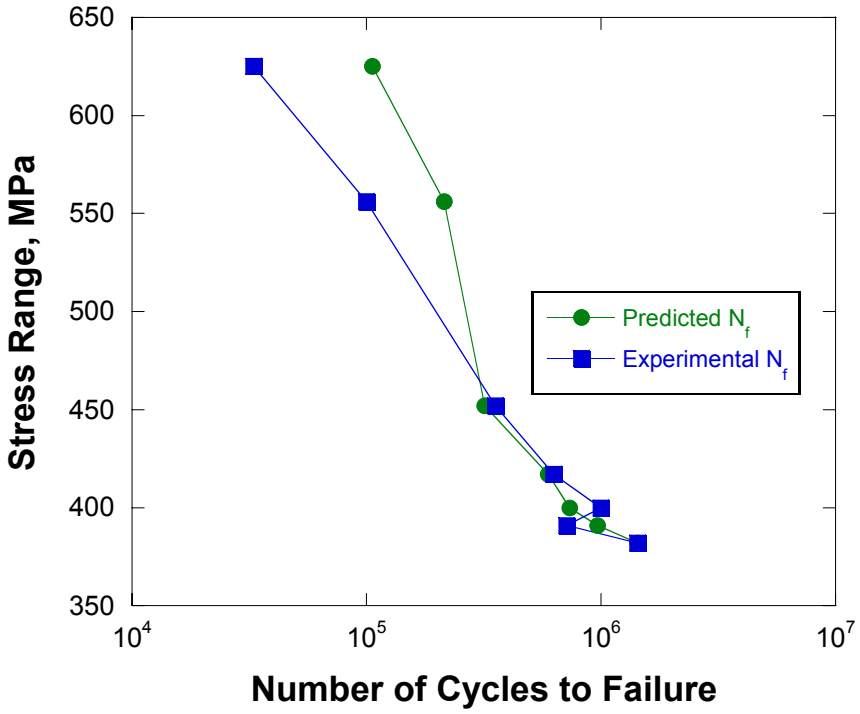

Figure 9.9: Predicted and experimental fatigue life using thermographic data.

predicted life are the same here. The experimental and predicted fatigue life is very similar at stress ranges below 450 MPa, however the experiment deviates at the two higher stresses. The experimental fatigue life is shorter than the predicted life. Stress-controlled fatigue experiments at high stress ranges are very flaw sensitive. Small defects at the surface can drastically decrease the fatigue life. Thus, the fatigue life may be shorter than one would expect. Secondarily, the maximum temperature reached at the stress ranges is on the margins of the calibrated temperature range of the infrared camera. Thus the maximum temperature may be slightly off in the two largest measurements.

9.4 Conclusions

The results of high-cycle fatigue tests on HASTELLOY C-2000 alloy monitored by infrared thermography have been reported. Thermographic analyses have shown that there is a distinct temperature-time sequence that took place during a room-temperature fatigue test; an initial temperature rise, followed by an equilibrium region, a sharp increase of temperature at failure and, finally, a cooling back to room temperature in the post-failure region. The thermographic profile of a single sample was analyzed in depth. Lastly, an empirical relationship between the equilibrium temperature during the fatigue test and the fatigue life was developed, as well as a calculation based on thermodynamic principles, both of which are useful for predicting fatigue life based on the steady-state temperature reached during fatigue.

Chapter 10
Conclusions

A comprehensive study of fatigue and deformation of two nickel based superalloys has been completed and presented in this dissertation.

The highlight of this research was the discovery, using both neutron and X-ray diffraction, of carbide debonding and cracking in tension of HAYNES 230. In contrast to the clear composite loading behavior of 7075 Aluminum and the single phase anisotropic behavior of HASTELLOY C-2000, the loading behavior of HAYNES 230 is unusual in tension and composite-like in compression. Modeling the expected behavior of HAYNES 230 also confirms that the tensile behavior is unusual. Carbide debonding and cracking in tension, but not in compression explains this tension-compression asymmetry. *In situ* X-ray diffraction explicitly shows the carbide accepting and then shedding load as debonding and cracking occurs, while microscopy confirmed that debonding and cracking had occurred. These mechanisms appear to occur at 420 MPa, just past the macroscopic yield of 390 MPa.

In tension-tension fatigue of HAYNES 230 alloy, at high loads, the internal strains saturate in the first 1000 cycles. Under the conditions tested, the residual strains after a uniaxial tension test and 42,417 cycles of fatigue are very similar. There are slight trends in relaxing and increasing residual strains over the first 100-1000 cycles. There appears to be no significant relaxation by 85% of the

fatigue life. The initial macroscopic strain of 15% appears to have largely saturated the internal strains by the first cycle. Future testing at lower σ_{max} should reveal the internal strain behavior over the initial stages of fatigue.

In tension-compression fatigue of HAYNES 230 alloy the internal strain accumulation is significant in the initial stages of fatigue. This is a much larger effect than seen in the higher maximum stress tension-tension test. Although the strain controlled nature of the experiment meant that there was plastic strain occurring on every cycle, internal elastic strains did saturate after the first 100 cycles of fatigue. The experiment ended prematurely due to sample alignment issues, so only the first 15% of the fatigue life was explored. However, the strains in the transverse direction in the carbide reveal a relaxation during the compression part of the cycle. This may be a sign of incremental debonding or cracking in the carbides as fatigue progressed.

Clear differences in the loading behavior of HAYNES 230 are noted with respect to the initial texture. The unusual bimodal textures seen in some samples are a result of incomplete annealing after material processing, particularly cross rolling. The final textures, as shown by experiment and VPSC modeling, are a superposition of the initial texture and typical FCC deformation mechanisms. The effect of initial texture on the macroscopic and internal strain during loading underscores the importance of understanding the texture of samples before using them as basis for comparison. Small changes in starting texture can easily obscure other subtle changes during loading experiments.

The *ex situ* diffraction results presented in Chapter 8 and the *in situ* results in Chapters 5-7 clearly show that elastic strain, texture and dislocation development are primarily noted during the initial plastic strain. However these effects no longer play a large role during subsequent tension-tension fatigue deformation. These initial effects are easily measured by neutron diffraction. The accumulation of damage, in the form of cracking, voids and other inhomogeneities, is shown clearly in the NRUS measurements, revealing progressive damage as fatigue cycles increase. Thus, these two techniques are complimentary showing both the initial changes over the first cycle and the accumulation of fatigue effects as failure is approached.

The results of high-cycle fatigue tests on HASTELLOY C-2000 alloy monitored by infrared thermography have been reported. Thermographic analyses have shown that there is a distinct temperature-time sequence that took place during a room-temperature fatigue test; an initial temperature rise, followed by an equilibrium region, a sharp increase of temperature at failure and, finally, a cooling back to room temperature in the post-failure region. The thermographic profile of a single sample was analyzed in depth. Lastly, an empirical relationship between the equilibrium temperature during the fatigue test and the fatigue life was developed, as well as a calculation based on thermodynamic principles, both of which are useful for predicting fatigue life based on the steady-state temperature reached during fatigue.

Chapter 11
Future Work

There are a few obvious continuing research projects from this dissertation. The carbide debonding and cracking shown in Chapter 5 would benefit from a more complete microscopy study, showing both tension and compression, perpendicular and parallel to applied loads. Similarly a set of *ex situ* loading samples, loaded to increasing levels, could be created and sectioned to show the onset of debonding and cracking. It is obvious from the neutron analysis that the strengthening mechanism fails in tension around 425 MPa, but neither neutron nor X-ray studies make it clear whether debonding or cracking is responsible for this. Based on the lack of doubling in the carbide spots in the X-ray patterns, it would appear that debonding is the primary mechanism, followed by cracking at higher stresses, but microscopy could confirm this trend. Similarly more in-depth microscopy could be used to see the role of carbides in fatigue, especially whether progressive debonding/cracking is responsible for the carbide behavior during the tension-compression experiments.

The *in situ* tension-tension experiments would benefit from lower R-ratio tests to see if there is more accumulation of elastic strains than the higher R-ratio presented here. Similarly, a single comprehensive *in situ* fatigue study with a single-phase FCC material would allow for a better understanding of fatigue effects on internal strains and texture. A single phase stainless steel or copper sample could be used for tests at low and high R ratios using stress and strain

controlled fatigue. Special care should be taken to allow for experiments to last to a high percentage of the fatigue life and focus on capturing the elusive final stages of fatigue. The new load frame at the 1-ID beam line at the APS should allow for high-frequency experiments to be conducted with a high capture rate image plate. With an appropriate small grained, thin sample, long *in situ* fatigue tests should be able to be completed quickly.

The NRUS has great potential for use in both fatigue and high pressure experiments for characterizing damage. With respect to HAYNES 230, more *ex situ* experiments could be conducted, in concert with neutron analyses, with tension-compression samples and lower R-ratio tension-tension samples to explore the sensitivity of the technique to various states of plastic deformation, cracking and other damage mechanisms. Similarly, these NRUS experiments could be used to characterize damage in single-phase FCC materials to compliment the experiments outlined in the previous paragraph.

It would be useful to integrate the neutron techniques more fully with both the NRUS and infrared thermography methods. The role of plastic and internal elastic strains, cracking and heat generation in a single fatigue experiments could be explored in depth. *In situ* neutron and infrared thermography experiments could be conducted at the exact same conditions as well as interrupted experiments for creating a large number *ex situ* samples for NRUS.

Finally, high-temperature fatigue effects in HAYNES 230 should be explored. Temperature and stress induced $M_{23}C_6$ carbide formation could be studied *in situ* and may explain both the plateau in yield strength between 600 and

900°C as well as the unusual longer fatigue life seen in low-cycle fatigue at high strain ranges at 927°C versus that at 816°C. The low percentage and small size of $M_{23}C_6$ carbides in the as-received state as well as in the heat-treated condition may require the use of synchrotron X-rays rather than neutrons to study this issue completely.

Bibliography

Bibliography

[1] Klarstrom DL. The development of HAYNES(R) 230(R) alloy. Materials Design Approaches and Experiences. Proceedings of Symposium, 4-8 Nov. 2001, Indianapolis, IN, USA 2001:p.297.

[2] Tawancy HM, Klarstrom DL, Rothman MF. Development of a New Nickel-Base Superalloy. J Met 1984;36:58.

[3] Haynes-International. HAYNES 230 Alloy Product Brochure, H-3000. Haynes International., 2004.

[4] Haynes-Intl. HAYNES 230 Alloy Product Brochure, . Haynes International., 2004.

[5] Chen LJ, Liaw PK, McDaniels RL, Wang GY, Liaw K, Blust JW, Thompson SA, Browning PF, Bhattacharya AK, Aurrecoechea JM, Seeley RR, Klarstrom DL. Low-cycle fatigue behavior and creep-fatigue life prediction of three superalloys. In: Lesur DR, Srivatsan TS, editors. Modelling the Performance of Engineering Structural Materials II. Proceedings of a Symposium, 4-8 Nov. 2001, Indianaplis, IN, USA: Warrendale, PA, USA : TMS - Miner. Metals & Mater. Soc, 2001. p.p.101.

[6] Lu YL, Liaw PK, Wang GY, Benson ML, Thompson SA, Blust JW, Browning PF, Bhattacharya AK, Aurrecoechea JM, Klarstrom DL. Fracture modes of HAYNES{sup (R)} 230{sup (R)} alloy during fatigue-crack-growth at room and elevated temperatures. Materials Science & Engineering A (Structural Materials: Properties, Microstructure and Processing) 2005;397:122.

[7] ASTM Standard E8, Standard Test Methods for Tension Testing of Metallic Materials. 2004.

[8] ASTM Standard E9, Standard Test Methods of Compression Testing of Metallic Materials at Room Temperature. 2000.

[9] Crook P, Caruso ML, Kingseed DA. Corrosion Resistance of a New, Wrought Ni-Cr-Mo Alloy Materials Performance 1997;36:49.

[10] Haynes-International. HASTELLOY C-2000 Alloy Product Brochure, H-2105B. 2001.

[11] Steward RV. C-2000 Alloy Research (unpublished work). University of Tennessee, 2005.

[12] Cohen JB, Noyan IC. Residual Stress: Springer –Verlag, 1987.

[13] Cullity BD. Elements of X-Ray Diffraction. Reading, Massachussetts: Addison-Wesley Publishing Company, Inc., 1978.

[14] Krawitz AD. Introduction to Diffraction in Materials Science and Engineering: Wiley-Interscience, 2001.

[15] Warren BE. X-Ray Diffraction. New York: Dover Publications, Inc., 1990.

[16] Daymond MR, Bourke MAM, VonDreele RB, Clausen B, Lorentzen T. Use of Rietveld refinement for elastic macrostrain determination and for evaluation of plastic strain history from diffraction spectra. Journal of Applied Physics 1997;82:1554.

[17] Larson AC, Von Dreele RB. General Structure Analysis System (GSAS). Los Alamos National Laboratory Report 2000;LAUR 86-748

[18] Bourke MAM, Dunand DC, Ustundag E. SMARTS - A spectrometer for strain measurement in engineering materials. Applied Physics A: Materials Science and Processing 2002;74:S1707.

[19] Dann JA, Daymond MR, Edwards L, James JA, Santisteban JR. A comparison between Engin and Engin-X, a new diffractometer optimized for stress measurement. Physica B: Condensed Matter 2004;350:e511.

[20] Daymond MR, Johnson MW. Optimisation of the design of a neutron diffractometer for strain measurement. Fifteenth Meeting of the International Collaboration on Advanced Neutron Sources. ICANS-XV, 6-9 Nov. 2000, Tsukuba, Japan: Ibaraki-ken, Japan : Japan Atomic Energy Res. Inst, 2001, 2000. p.p.499.

[21] Holden TM. The Science Case for the Vulcan Diffractometer. http://www.sns.anl.gov/pdfs/engdiff/Vulcan.pdf, 2001.

[22] Wanner A, Dunand DC. Synchrotron X-ray study of bulk lattice strains in externally loaded Cu-Mo composites. Metallurgical and Materials Transactions A: Physical Metallurgy and Materials Science 2000;31:2949.

[23] Haeffner DR, Almer JD, Lienert U. The use of high energy X-rays from the Advanced Photon Source to study stresses in materials. Materials Science and Engineering A 2005;399:120.

[24] Daymond MR, Withers PJ. A synchrotron radiation study of transient internal strain changes during the early stages of thermal cycling in an Al/SiC{sub W} MMC. Scripta Materialia 1996;35:1229.

[25] Kocks UF, Tome CN, Wenk HR. Texture and anisotropy: preferred orientations in polycrystals and their effect on materials properties New York: Cambridge University Press, 1998.

[26] Karato SI, Wenk HR. Plastic Deformation of Minerals and Rocks. Washington, DC: The Mineralogical Society of America, 2002.

[27] Wenk HR. Preferred Orientation in Deformed Metals and Rocks: An Introduction to Modern Texture Analysis. New York: Academic Press, Inc., 1985.

[28] Wenk HR, Lutterotti L, Vogel S. Texture analysis with the new HIPPO TOF diffractometer. Nuclear Instruments & Methods in Physics Research, Section A (Accelerators, Spectrometers, Detectors and Associated Equipment) 2003;515:575.

[29] Vogel SC, Hartig C, Lutterotti L, Von Dreele RB, Wenk HR, Williams DJ. Texture measurements using the new neutron diffractometer HIPPO and their analysis using the Rietveld method. Powder Diffraction 2004;19:65.

[30] Brown DW, Bourke MAM, Clausen B, Holden TM, Tome CN, Varma R. A neutron diffraction and modeling study of uniaxial deformation in polycrystalline beryllium. Metallurgical and Materials Transactions A (Physical Metallurgy and Materials Science) 2003;34A:1439.

[31] Windsor CG, Allen AJ, Hutchings MT, Sayers CM, Sinclair RN, Schofield P, Wright CJ. Neutrons for materials science. Neutron Scattering in the 'Nineties. Proceedings of a Conference, 14-18 Jan. 1985, Julich, West Germany: Vienna, Austria : IAEA, 1985. p.p.575.

[32] Allen AJ, Hutchings MT, Windsor CG, Andreani C. Neutron diffraction methods for the study of residual stress fields. Advances in Physics 1985;34:445.

[33] Clark GL. Applied X-Rays. N.Y.: McGraw-Hill Book Company, Inc., 1927.

[34] Allen A, Andreani C, Hutchings MT, Windsor CG. Measurement of internal stress within bulk materials using neutron diffraction. NDT International 1981;14:249.

[35] Bourke MAM, Goldstone JA, Shi N, Allison JE, Stout MG, Lawson AC. Measurement and prediction of strain in individual phases of a 2219Al/TiC/15p-T6 composite during loading. Scripta Metallurgica et Materialia 1993;29:771.

[36] Bourke MAM, Goldstone JA, Stout MG, Lawson AC, Allison JE. Strain-Measurement in Individual Phases of an Al-Tic Composite During Mechanical Loading. In: Barrera EV, Dutta I, editors. Symposium on Residual Stresses in Composites; February 21-25, 1993; DENVER, CO. Denver, CO: Minerals, Metals & Materials Soc, 1993. p.67.

[37] Johnson MW, Edwards L, Withers PJ. ENGIN-a new instrument for engineers. Physica B 1997;234/236:1141.

[38] Lester HH, Aborn RH. The behavior under stress of the iron crystals in steel. Army Ordnance 1925-6;6:Various.

[39] Wood WA, Rachinger WA. X-ray diffraction rings from deformed solid metal and metal powders. Nature 1948;161:93.

[40] Smith SL, Wood WA. A stress/strain curve for the atomic lattice of mild steel and the physical significance of the yield point of a metal. Proceedings of the Royal Society of London, Series A (Mathematical and Physical Sciences) 1942;179:450.

[41] Smith SL, Wood WA. A stress/strain carve for the atomic lattice of mild steel in compression. Proceedings of the Royal Society of London, Series A (Mathematical and Physical Sciences) 1942;181:72.

[42] Wood WA, Smith SL. A stress/strain curve for the atomic lattice of aluminium. Journal of the Institute of Metals 1941;67:315.

[43] Smith SL, Wood WA. X-ray structure and elastic strains in copper. Proceedings of the Royal Society of London, Series A (Mathematical and Physical Sciences) 1940;176:398.

[44] Wood WA, Thorpe PL. Behaviour of crystal structure of brass under slow and rapid cyclic stresses. Proceedings of the Royal Society of London, Series A (Mathematical and Physical Sciences) 1940;174:310.

[45] Wood WA. X-ray diffraction and the deformation of metals. Journal of Scientific Instruments 1941;18:153.

[46] Wood WA. Study of internal stress in metal by X-ray diffraction. Engineers' Digest (American Edition) 1944;1:618.

[47] Gough HJ, Wood WA. Deformation and fracture of mild steel under cyclic stresses in relation to crystalline structure. Proceedings of the Institution of Mechanical Engineers 1939;141:175.

[48] Greenough GB. Internal Stresses in Metals. Nature 1948;161:683.

[49] Greenough GB. Residual lattice strains in plastically deformed polycrystalline metal aggregates. Proceedings of the Royal Society of London, Series A (Mathematical and Physical Sciences) 1949;197:556.

[50] Greenough GB. Strain measurement by X-ray diffraction methods. Aeronautical Quarterly 1949;1:211.

[51] Greenough GB. Quantitative X-ray diffraction observations on strained metal aggregates. Progress in Metal Physics 1952;3:176.

[52] Spencer RG. X-ray study of changes in malleable iron during process of fatiguing. Physical Review 1939;55:991.

[53] Tapsell HJ, Wood WA. A combined creep machine and X-ray spectrometer. Journal of Scientific Instruments and Physics in Industry 1948;25:198.

[54] Bennett JA. A study of fatigue in metals by means of X-ray strain measurement. Journal of Research of the National Bureau of Standards 1951;46:457.

[55] Greenough GB, Bateman CM, Smith EM. X-ray diffraction studies in relation to creep. Journal of the Institute of Metals 1952;80:545.

[56] Cheskis HP, Heckel RW. Investigation of deformation behavior of individual phases in composites by X-ray diffraction. Journal of Metals 1968;20:A113.

[57] Cheskis HP, Heckel RW. Deformation behavior of continuous-fiber metal-matrix composite materials. Met Trans 1970;1:1931.

[58] Clausen B, Lorentzen T. A Self-Consistant Model for Polycrystalline Deformation. Risø National Laboratory, DK-4000 Roskilde, Denmark 1997;Riso-R-970.

[59] Clausen B, Lorentzen T, Leffers T. Self-consistent modelling of the plastic deformation of FCC polycrystals and its implications for diffraction measurements of internal stresses. Acta Materialia 1998;46:3087.

[60] Hutchinson JW. Elastic-plastic behaviour of polycrystalline metals and composites. Proceedings of the Royal Society of London, Series A (Mathematical and Physical Sciences) 1970;319:247.

[61] Clausen B, Lorentzen T. Experimental evaluation of a polycrystal deformation modeling scheme using neutron diffraction measurements.

Metallurgical and Materials Transactions A-Physical Metallurgy and Materials Science 1997;28:2537.

[62] Eshelby JD. The determination of the elastic field of an ellipsoidal inclusion, and related problems. Proceedings of the Royal Society of London Series A-Mathematical and Physical Sciences 1957;241:376.

[63] Korsunsky AM, Jarnes KE, Daymond MR. Intergranular stresses in polycrystalline fatigue: diffraction measurement and self-consistent modelling. Engineering Fracture Mechanics 2004;71:805.

[64] Daymond MR, Priesmeyer HG. Elastoplastic deformation of ferritic steel and cementite studied by neutron diffraction and self-consistent modelling. Acta Materialia 2002;50:1613.

[65] Lorentzen T, Daymond MR, Clausen B, Tome CN. Lattice strain evolution during cyclic loading of stainless steel. Acta Materialia 2002;50:1627.

[66] Oliver EC, Daymond MR, Withers PJ. Interphase and intergranular stress generation in carbon steels. Acta Materialia 2004;52:1937.

[67] Daymond MR. A combined finite element and self-consistent model; Validation by neutron diffraction strain scanning. Materials Science Forum 2005;495-497:1019.

[68] Priesmeyer HG, Daymond MR. Elastoplastic deformation of ferritic steel and cementite studied by neutron diffraction and self-consistent modelling. Acta Materialia 2002;50:1613.

[69] Clausen B, Lorentzen T, Bourke MAM, Daymond MR. Lattice strain evolution during uniaxial tensile loading of stainless steel. Materials Science & Engineering A (Structural Materials: Properties, Microstructure and Processing) 1999;A259:17.

[70] Agnew SR, Tome CN, Brown DW, Holden TM, Vogel SC. Study of slip mechanisms in a magnesium alloy by neutron diffraction and modeling. Scripta Materialia 2003;48:1003.

[71] Brown DW, Agnew SR, Bourke MAM, Holden TM, Vogel SC, Tome CN. Internal strain and texture evolution during deformation twinning in magnesium. Materials Science and Engineering A 2005;399:1.

[72] Tome CN, Agnew SR, Blumenthal WR, Bourke MAM, Brown DW, Kaschner GC, Rangaswamy P. The relation between texture, twinning and

mechanical properties in hexagonal aggregates. Materials Science Forum 2002;408/412:263.

[73] Brown DW, Abeln SP, Blumenthal WR, Bourke MAM, Mataya MC, Tome CN. Development of crystallographic texture during high rate deformation of rolled and hot-pressed beryllium. Metallurgical and Materials Transactions A (Physical Metallurgy and Materials Science) 2005;36A:929.

[74] Turner PA, Tome CN. A study of residual stresses in Zircaloy-2 with rod texture. Acta Metallurgica et Materialia 1994;42:4143.

[75] Brown DW, Bourke MAM, Dunn PS, Field RD, Stout MG, Thoma DJ. Uniaxial tensile deformation of uranium 6 wt pct niobium: A neutron diffraction study of deformation twinning. Metallurgical and Materials Transactions A: Physical Metallurgy and Materials Science 2001;32:2219.

[76] Field RD, Brown DW, Thoma DJ. Texture development and deformation mechanisms during uniaxial straining of U-Nb shape-memory alloys. Philosophical Magazine 2005;85:1441.

[77] Lebensohn RA, Tome CN, Maudlin PJ. A selfconsistent formulation for the prediction of the anisotropic behavior of viscoplastic polycrystals with voids. Journal of the Mechanics and Physics of Solids 2004;52:249.

[78] Clausen B, Lee SY, Ustundag E, Aydiner CC, Conner RD, Bourke MAM. Compressive yielding of tungsten fiber reinforced bulk metallic glass composites. Scripta Materialia 2003;49:123.

[79] Allen AJ, Bourke MAM, Dawes S, Hutchings MT, Withers PJ. The analysis of internal strains measured by neutron diffraction in Al/SiC metal matrix composites. Acta Metallurgica et Materialia 1992;40:2361.

[80] Choo H, Rangaswamy P, Bourke MAM, Larsen JM. Thermal expansion anisotropy in a Ti-6Al-4V/SiC composite. Materials Science and Engineering A-Structural Materials Properties Microstructure and Processing 2002;325:236.

[81] Povirk GL, Stout MG, Bourke M, Goldstone JA, Lawson AC, Lovato M, Macewen SR, Nutt SR, Needleman A. Mechanically induced residual stresses in Al/SiC composites. Scripta Metallurgica et Materialia 1991;25:1883.

[82] Povirk GL, Stout MG, Bourke M, Goldstone JA, Lawson AC, Lovato M, Macewen SR, Nutt SR, Needleman A. Thermally and mechanically

induced residual strains in Al-SiC composites. Acta Metallurgica et Materialia 1992;40:2391.

[83] Withers PJ, Clarke AP. A neutron diffraction study of load partitioning in continuous Ti/SiC composites. Acta Materialia 1998;46:6585.

[84] Clausen B, Lee SY, Ustundag E, Kim CP, Brown DW, Bourke MAM. Deformation of in-situ-reinforced bulk metallic glass matrix composites. Materials Science Forum 2002;404/407:553.

[85] Dragoi D, Ustundag E, Clausen B, Bourke MAM. Investigation of thermal residual stresses in tungsten-fiber/bulk metallic glass matrix composites. Scripta Materialia 2001;45:245.

[86] Ma S, Brown D, Bourke MAM, Daymond MR, Majurndar BS. Microstrain evolution during creep of a high volume fraction superalloy. Materials Science and Engineering A 2005;399:141.

[87] Ma S, Rangaswamy P, Majumdar BS. Microstress evolution during in situ loading of a superalloy containing high volume fraction of gamma ' phase. Scripta Materialia 2003;48:525.

[88] Spencer RG, Marshall JW. X-ray study of the changes that occur in Al during the process of fatiguing. Journal of Applied Physics 1941;12:191.

[89] Quesnel DJ, Meshii M, Cohen JB. Residual stresses in high strength low alloy steel during low cycle fatigue. Material Science and Engineering 1978;36:207.

[90] McClinton M, Cohen JB. Changes in residual stress during the tension fatigue of normalized and peened SAE 1040 steel. Material Science and Engineering 1982;56:259.

[91] Wang YD, Tian HB, Stoica AD, Wang XL, Liaw PK, Richardson JW. The development of grain-orientation-dependent residual stressess in a cyclically deformed alloy. Nature Materials 2003;2:101.

[92] Daymond MR, Withers PJ. In situ monitoring of thermally cycled metal matrix composites by neutron diffraction and laser extensometry. Applied Composite Materials 1997;4:375.

[93] Daymond MR, Withers PJ. A new stroboscopic neutron diffraction method for monitoring materials subjected to cyclic loads: thermal cycling of metal matrix composites. Scripta Materialia 1996;35:717.

[94] Eckold G, Gibhardt H, Caspary D, Elter P, Elisbihani K. Stroboscopic neutron diffraction from spatially modulated systems. Zeitschrift fur Kristallographie 2003;218:144.

[95] Schillinger B, Abele H, Brunner J, Frei G, Gahler R, Gildemeister A, Hillenbach A, Lehmann E, Vontobel P. Detection systems for short-time stroboscopic neutron imaging and measurements on a rotating engine. Nuclear Instruments and Methods in Physics Research, Section A: Accelerators, Spectrometers, Detectors and Associated Equipment 2005;542:142.

[96] Almer JD. Microstructure and Internal Strain Measurements in Bone Via High-Energy X-Rays. Presentation at MECA SENS III, . Santa Fe, NM, 2005.

[97] Vaidyanathan R, Bourke MAM, Dunand DC. Texture, strain, and phase-fraction measurements during mechanical cycling in superelastic NiTi. Metallurgical and Materials Transactions A-Physical Metallurgy and Materials Science 2001;32:777.

[98] Rajagopalan S, Little AL, Bourke MAM, Vaidyanathan R. Elastic modulus of shape-memory NiTi from in situ neutron diffraction during macroscopic loading, instrumented indentation, and extensometry. Applied Physics Letters 2005;86:81901.

[99] Taran YV, Daymond MR, Eifler D, Nebel T, Schreiber J. Investigation of mechanical features of low cycle fatigue specimens of austenitic steel AISI type 321 under applied load by neutron diffraction stress analysis. Materials Science and Technology 2005;21:35.

[100] Taran YV, Daymond MR, Schreiber J. Interplay of stresses induced by phase transformation and plastic deformation during cyclic load of austenitic stainless steel. Physica B-Condensed Matter 2004;350:98.

[101] Benson ML, Saleh TA, Liaw PK, Choo H, Brown DW, Daymond MR, Wang XL, Stoica AD, Buchanan RA, Klarstrom DL. Fatigue-induced phase formation and its deformation behavior in a cobalt-based superalloy. Powder Diffraction 2005;20:121.

[102] Jiang L, Liaw PK, Brooks CR, Somieski B, Klarstrom DL. Nondestructive evaluation of fatigue damage in ULTIMET (R) superalloy. Materials Science and Engineering A-Structural Materials Properties Microstructure and Processing 2001;313:153.

[103] Jiang L, Brooks CR, Liaw PK, Dunlap J, Rawn CJ, Peascoe RA, Klarstrom DL. Low-cycle fatigue behavior of ULTIMET(R) alloy.

Metallurgical and Materials Transactions A (Physical Metallurgy and Materials Science) 2004;35A:785.

[104] D'Halloy O. Introduction à la Géologie, 1833.

[105] Naumann CF. Lehrbuch der Geognosie. Engelmann, Leipzig, 1850.

[106] Wever F. The structure of rolled cubic crystallising metals. Zeitschrift fur Physik 1924;28:69.

[107] Decker BF, Asp ET, Harker D. Preferred orientation determination using a Geiger counter X-ray diffraction goniometer. Journal of Applied Physics 1948;19:388.

[108] Norton JT. Technique for quantitative determination of texture of sheet metals. Journal of Applied Physics 1948;19:1176.

[109] Brockhouse BN. Initial magnetization of nickel under tension. Canadian Journal of Physics 1953;31:339.

[110] Leisure RG, Willis FA. Resonant ultrasound spectroscopy. Journal of Physics: Condensed Matter 1997;9:6001.

[111] Migliori A, Darling TW. Resonant ultrasound spectroscopy for materials studies and non-destructive testing. Ultrasonics 1996;34:473.

[112] Migliori A, Sarrao JL, Visscher WM, Bell TM, Lei M, Fisk Z, Leisure RG. Resonant ultrasound spectroscopic techniques for measurement of the elastic moduli of solids. Physica B 1993;183:1.

[113] Migliori A, Visscher WM, Brown SE, Fisk Z, Cheong SW, Alten B, Ahrens ET, Kubatmartin KA, Maynard JD, Huang Y, Kirk DR, Gillis KA, Kim HK, Chan MHW. Elastic constants and specific-heat measurements on single crystals of La{sub 2}CuO{sub 4}. Physical Review B (Condensed Matter) 1990;41:2098.

[114] Schwarz RB, Vuorinen JF. Resonant ultrasound spectroscopy: applications, current status and limitations. Journal of Alloys and Compounds 2000;310:243.

[115] Bach HT, Schwarz RB, Tuggle DG. Hydrogen, deuterium and tritium in palladium: an elastic constants study. Fusion Science and Technology 2005;48:545.

[116] Foster K, Fairburn SL, Leisure RG, Kim S, Balzar D, Alers G, Ledbetter H. Acoustic study of texture in polycrystalline brass. Journal of the Acoustical Society of America 1999;105:2663.

[117] Ogi H, Nakamura N, Hirao M, Ledbetter H. Determination of elastic, anelastic, and piezoelectric coefficients of piezoelectric materials from a single specimen by acoustic resonance spectroscopy. Ultrasonics 2004;42:183.

[118] Tane M, Ichitsubo T, Ogi H, Hirao M. Elastic property of aged duplex stainless steel. Scripta Materialia 2003;48:229.

[119] Teklu A, Ledbetter H, Kim S, Boatner LA, McGuire M, Keppens V. Single-crystal elastic constants of Fe-15Ni-15Cr alloy. Metallurgical and Materials Transactions A (Physical Metallurgy and Materials Science) 2004;35A:3149.

[120] Jung HK, Cheong YM, Ryu HJ, Hong SH. Analysis of anisotropy in elastic constants of SiC{sub p}/2124 Al metal matrix composites. Scripta Materialia 1999;41:1261.

[121] Whitney TM, Green RE. Low temperature characterization of carbon epoxy composites: an application of resonant ultrasound spectroscopy. Ultrasonics 1996;34:383.

[122] Muller M, Sutin A, Guyer R, Talmant M, Laugier P, Johnson PA. Nonlinear resonant ultrasound spectroscopy (NRUS) applied to damage assessment in bone. Journal of the Acoustical Society of America 2005;118:3946.

[123] Ulrich TJ, Darling TW. Observation of anomalous elastic behavior in rock at low temperatures. Geophysical Research Letters 2001;28:2293.

[124] Ulrich TJ, McCall KR, Guyer RA. Determination of elastic moduli of rock samples using resonant ultrasound spectroscopy. Journal of the Acoustical Society of America 2002;111:1667.

[125] Adachi T, Kondo Y, Yamaji A, Yang SH, Yang IY. Nondestructive evaluation of micro-cracks in a ceramic ferrule by resonant ultrasound spectroscopy. NDT&E International 2005;38:548.

[126] Cho H, Komatsu K, Ishikawa S, Tanimoto K, Takii H, Yamanaka K. Evaluation on micro cracks in ceramic bearing balls by using the floating resonance of surface acoustic waves. Japanese Journal of Applied Physics, Part 1: Regular Papers and Short Notes and Review Papers 2003;42:3176.

[127] Leisure RG, Foster K, Hightower JE, Agosta DS. Internal friction studies by resonant ultrasound spectroscopy. Materials Science and Engineering A 2004;370:34.

[128] Johnson PA. New wave in acoustic testing. Materials World 1999;7:544.

[129] Johnson PA, Sutin A. Nonlinear elastic wave NDE I. Nonlinear resonant ultrasound spectroscopy and slow dynamics diagnostics. AIP Conference Proceedings 2005:377.

[130] Ostrovsky LA, Johnson PA. Dynamic nonlinear elasticity in geomaterials. Rivista del Nuovo Cimento 2001;24:1.

[131] Sutin AM, Johnson PA. Nonlinear elastic wave NDE II. Nonlinear wave modulation spectroscopy and nonlinear time reversed acoustics. Aip Conference Proceedings 2005;760:385.

[132] Todhunter I, Pearson K. A History of the Elasticity and Strength of Materials: Cambridge Press, 1893.

[133] Taylor GI, Quinney H. Latent energy remaining in a metal after cold working. Proceedings of the Royal Society of London 1934;143:307.

[134] Biot MA. Thermoelasticity and irreversible thermodynamics. Journal of Applied Physics 1956;27:240.

[135] Rocca R, Bever MB. Thermoelastic effect in iron and nickel as function of temperature. American Institute of Mining and Metallurgical Engineers -- Journal of Metals 1950;188:327.

[136] Rice JR, Levy N, Argon AS. Local heating by plastic deformation at a crack tip. Cambridge, MA, USA : M.I.T, 1969, 1969. p.p.277.

[137] Yang B, Liaw PK, Wang G, Morrison M, Liu CT, Buchanan RA, Yokoyama Y. In-situ thermographic observation of mechanical damage in bulk-metallic glasses during fatigue and tensile experiments. Intermetallics 2004;12:1265.

[138] Yang B, Liaw PK, Morrison M, Liu CT, Buchanan RA, Huang JY, Kuo RC, Huang JG, Fielden DE. Temperature evolution during fatigue damage. Intermetallics 2005;13:419.

[139] Yang B, Liaw PK, Huang JY, Kuo RC, Huang JG, Fielden DE. Stress analyses and geometry effects during cyclic loading using thermography. Transactions of the ASME. Journal of Engineering Materials and Technology 2005;127:75.

[140] Yang B, Liaw PK, Wang G, Peter WH, Buchanan RA, Yokoyama Y, Huang JY, Kuo RC, Huang JG, Fielden DE, Klarstrom DL. Thermal-imaging technologies for detecting damage during high-cycle fatigue.

Metallurgical and Materials Transactions A (Physical Metallurgy and Materials Science) 2004;35A:15.

[141] Jiang L. Fatigue Behavior of ULTIMET Alloy: Experiment and Theoretical Modeling. Department of Materials Science and Engineering, vol. Ph. D. Knoxville, TN: University of TN, Knoxville, 2000.

[142] Jiang L, Wang H, Liaw PK, Brooks CR, Chen L, Klarstrom DL. Temperature evolution and life prediction in fatigue of superalloys. Metallurgical and Materials Transactions A (Physical Metallurgy and Materials Science) 2004;35A:839.

[143] Jiang L, Wang H, Liaw PK, Brooks CR, Klarstrom DL. Characterization of the temperature evolution during high-cycle fatigue of the ULTIMET superalloy: Experiment and theoretical modeling. Metallurgical and Materials Transactions A: Physical Metallurgy and Materials Science 2001;32:2279.

[144] Jiang L, Wang H, Liaw PK, Brooks CR, Klarstrom DL. Effects of cyclic loading on temperature evolution of ULTIMET(R) superalloy: experiment and theoretical modeling. Transactions of the Nonferrous Metals Society of China 2002;12:734.

[145] Jiang L, Wang H, Liaw PK, Brooks CR, Klarstrom DL. Temperature evolution during low-cycle fatigue of ULTIMET(R) alloy: experiment and modeling. Mechanics of Materials 2004;36:73.

[146] Yang B. Thermography detection on the fatigue damage. Department of Materials Science and Engineering, vol. Ph. D. Knoxville, TN: University of Tennessee, Knoxville, 2003.

[147] Yang B, Liaw PK, Wang H, Jiang L, Huang JY, Kuo RC, Huang JG. Thermographic investigation of the fatigue behavior of reactor pressure vessel steels. Materials Science and Engineering A 2001;314:131.

[148] Saleh TA, Steward RV. *In Situ* loading of HASTELLOY C-2000, *unpublished*. 2005.

[149] Saleh TA, Jeon JW, Pang J, Hubbard CR, Brown DW, Choo H, Liaw PK, Bourke MAM. Implications of Different Strengthening Mechanisms on Intergranular Strains in Various Aluminum Alloys. American Conference on Neutron Scattering. College Park, MD, 2004.

[150] Dieter GE. Mechanical Metallurgy. Boston: McGraw-Hill, 1986.

[151] ABAQUS User Manual, version 6.3 www.abaqus.com. 2002.

[152] Mishnaevsky L, Weber U, Schmauder S. Numerical analysis of the effect of microstructures of particle-reinforced metallic materials on the crack growth and fracture resistance. International Journal of Fracture 2004;125:33.

[153] VonDreele RB. Quantitative texture analysis by Rietveld refinement. Journal of Applied Crystallography 1997;30:517.

[154] Vogel SC, Alexander DJ, Beyerlein IJ, Bourke MAM, Brown DW, Clausen B, Tome CN, Von Dreele RB, Xu C, Langdon TG. Investigation of texture in ECAP materials using neutron diffraction. Materials Science Forum 2003;426/432:2661.

[155] Wenk HR, Kocks UF. Program POD, Version 8.7a. 1996.

[156] Bronkhorst CA, Kalidindi SR, Anand L. Polycrystalline plasticity and the evolution of crystallographic texture in FCC metals. Philosophical Transactions of the Royal Society, Series A (Physical Sciences and Engineering) 1992;341:443.

[157] Klarstrom DL. Personal communication with Dr. D.L. Klarstrom, 10/21/05. 2005.

[158] Tirschler W, Tamm R, Blochwitz C, Skrotzki W. Texture stability of nickel during cyclic deformation at room temperature. Materials Science & Engineering A (Structural Materials: Properties, Microstructure and Processing) 1998;A254:311.

[159] Lebensohn RA, Tome CN. A self-consistent anisotropic approach for the simulation of plastic deformation and texture development of polycrystals: application to zirconium alloys. Acta Metallurgica et Materialia 1993;41:2611.

[160] Lebensohn RA, Tome CN. A Self-Consistent Viscoplastic Model - Prediction Of Rolling Textures Of Anisotropic Polycrystals. Materials Science and Engineering A-Structural Materials Properties Microstructure and Processing 1994;175:71.

[161] Liaw PK, Wang H, Jiang L, Yang B, Huang JY, Kuo RC, Huang JG. Thermographic detection of fatigue damage of pressure vessel steels at 1,000 Hz and 20 Hz. Scripta Materialia 2000;42:389.

[162] Wang H, Jiang L, He YH, Chen LJ, Liaw PK, Seeley RR, Klarstrom DL. Infrared imaging during low-cycle fatigue of HR-120 alloy. Metallurgical and Materials Transactions A (Physical Metallurgy and Materials Science) 2002;33A:1287.

[163] Hsin W, Liang J, Liaw PK, Brooks CR, Klarstrom DL. Infrared temperature mapping of ULTIMET alloy during high-cycle fatigue tests. Metallurgical and Materials Transactions A (Physical Metallurgy and Materials Science) 2000;31A:1307.

Vita

Tarik Saleh was born in the dark of the New Jersey winter of 1972. He was raised within 15 minutes of the Jersey shore, thus had the love of Bruce Springsteen hardwired into him. After a bucolic childhood of running, cycling and going to the beach, he graduated from the mighty Holmdel High School in 1991. He subsequently attended the Massachusetts Institute of Technology where he ran, biked and occasionally studied and graduated in 1995 with a Bachelors of Science in Materials Science and Engineering and a minor in Architecture. Subsequently he attended the University of California, Berkeley from 1996-97 and received a Masters of Engineering in Materials Science and Engineering in 2000. After working for four years in a rapid prototyping foundry and at Lawrence Berkeley National Laboratory, Tarik left California and moved to Knoxville, Tennessee. Here he attended the University of Tennessee, and flourished despite the lack of a nearby ocean. He split his time between UT and Los Alamos National Laboratory where he learned to bend the very neutron to his will. He completed his doctorate in May 2006, much to the relief of all involved. Tarik hopes to use his knowledge for good, or perhaps evil, depending on which allows him to spend more time on his bicycle.